# Colour Centres in 3D Nanostructures for Quantum Applications

HELMHOLTZ ZENTRUM DRESDEN ROSSENDORF

TECHNISCHE UNIVERSITÄT DRESDEN

Vorgelegt der Fakultät Mathematik und Naturwissenschaften
der Technischen Universität Dresden
zur Erlangung des akademischen Grades

## Doctor of Philosophy (Ph.D.)

angenommene Dissertation
Von


## M.Sc. Nagesh Shamrao Jagtap

born on 4th July, 1994 in Pune, India


Tage der Einreichung:
Tage der Verteidigung:

| Supervisor: | Gutachter: |
|---|---|
| Prof. Dr. Artur Erbe | Prof. Dr. Manfred Helm |
| PD. Dr. Georgy Astakhov | Prof. Dr. Eva Weig |

*To my Parents*

# Abstract

Quantum technology and devices, from mobile phones to autonomous vehicles, have become integral to our daily lives. Ongoing developments aim to enhance the performance of these quantum systems through fundamental and applied research. For example, creating a quantum photonic integrated circuit (QPIC) in silicon will bring us closer to a practical quantum computer.

A single-photon telecom emitter in silicon was the missing link for practically realising QPICs. To address this, we have overcome the challenge of integrating single-photon emitters into silicon nanopillars. In this work, I present a scalable and industry-friendly fabrication protocol using metal-assisted chemical etching, which allows the fabrication of smooth and anisotropic nanostructures. Additionally, spectroscopic measurements confirm that the fabrication protocol does not create any colour centres emitting in the telecommunication band.

Next, we use carbon broad-beam ion implantation to create telecom-photon emitting G-centres in silicon nanopillars. We measure a 20% enhancement in the photoluminescence signal from pillars compared to the bulk Si due to the waveguiding effect and a Debye-Waller factor of 12%. In addition, we have developed a wafer-scale broad beam ion irradiation protocol to create G-centres and W-centres in silicon.

The second part presents the concept of a hybrid spin-mechanical system based on silicon carbide to enhance magnetic field sensitivity. In this work, the envisioned hybrid quantum system requires the spin associated with a silicon vacancy ($V_{Si}$) to be coupled with the phononic modes of a nanomechanical resonator or strings in 4H-SiC. For such high-optical-quality resonators, photoelectrochemical dopant-selective etching is the only viable method and is in progress.

To contribute to the realisation of such a hybrid quantum system, we study high-mechanical-quality ($Q{\sim}10^4$) 3C-SiC strings. We fabricate the strings using a standard top-down nanofabrication approach. Afterwards, we characterise strings by employing interferometric detection to determine the resonant frequencies and quality factors. We also determine the stress and Young's modulus using the Euler-Bernoulli beam theory.

At last, we create silicon vacancies ($V_{Si}$) by broad beam helium implantation and characterise the mechanical response after each implantation step. We study the change in stress and Young's modulus with fluences of $\Phi$=$1 \times 10^{12}\,\mathrm{cm}^{-2}$, $1 \times 10^{13}\,\mathrm{cm}^{-2}$, and $1 \times 10^{14}\,\mathrm{cm}^{-2}$ at an energy $E_{\mathrm{I}}$=14 keV. Young's modulus remains unaltered by helium ion implantation. The tensile stress change is negligible for the lowest ion fluence, where single or ensembles of $V_{Si}$ are created. However, stress relaxes by 30% at the highest implantation fluence $\Phi$=$1 \times 10^{14}\,\mathrm{cm}^{-2}$.

# Zusammenfassung

Quantentechnologien und darauf basierende Geräte, von Mobiltelefonen bis hin zu autonomen Fahrzeugen, sind aus unserem täglichen Leben nicht mehr wegzudenken. Aktuelle Entwicklungen zielen darauf ab, die Leistungsfähigkeit dieser Quantensysteme durch Grundlagenforschung und angewandte Forschung zu verbessern. Beispielsweise wird uns die Entwicklung eines integrierten Quantenphotonik-Schaltkreises (QPIC) in Silizium-Technologie einem praktischen Quantencomputer näherbringen.

Ein Einzelphotonen-Emitter in Silizium war bisher für die Telekommunikation das fehlende Glied für die praktische Realisierung von QPICs. Deshalb haben wir die Herausforderung der Integration von Einzelphotonen-Emittern in Silizium-Nanosäulen gemeistert. In dieser Arbeit wird ein skalierbares und industrietaugliches Herstellungsverfahren vorgestellt, welches metallunterstütztes chemisches Ätzen verwendet und die Herstellung glatter und anisotroper Nanostrukturen ermöglicht. Außerdem bestätigen spektroskopische Messungen, dass das Herstellungsverfahren keine Defekte als Farbzentren erzeugt, die Licht im Telekommunikationsband emittieren.

Als Nächstes verwenden wir die Kohlenstoff-Breitstrahl-Ionenimplantation, um Telephotonen emittierende G-Farbzentren in Silizium Nanosäulen zu erzeugen. Wir messen eine 20%-ige Verstärkung des Photolumineszenzsignals der Säulen im Vergleich zu Si Volumenmaterial und einen Debye-Waller-Faktor von 12%. Darüber hinaus haben wir ein Breitstrahl-Ionenbestrahlungsverfahren im Wafermaßstab entwickelt, um G- und W-Farbzentren in Silizium zu erzeugen.

Im zweiten Teil wird das Konzept eines hybriden spin-mechanischen Systems auf der Grundlage von Siliziumkarbid zur Verbesserung der Magnetfeldempfindlichkeit präsentiert. Das hier vorgestellte hybride Quantensystem setzt voraus, dass der mit einer Siliziumleerstelle ($V_{Si}$) verbundene Elektronen-Spin mit den phononischen Moden eines nanomechanischen Resonators oder einer Saite in 4H-SiC gekoppelt wird. Für solche Resonatoren von hoher optischer Qualität ist das photoelektrochemische dotierungsselektive Ätzen die einzige praktikable Methode, die noch in der Entwicklung ist.

Um die Realisierung eines solchen hybriden Quantensystems voranzubringen, untersuchen wir 3C-SiC-Saiten von hoher mechanischer Qualität ($Q{\sim}10^4$). Wir stellen die Saiten mit einer Standard-Top-Down-Nanofabrikationsmethode her. Anschließend charakterisieren wir die Saiten interferometrisch, um die Resonanzfrequenzen und Gütefaktoren zu bestimmen. Mithilfe der Euler-Bernoulli-Balken-Theorie bestimmen wir außerdem die intrinsische Spannung und das Elastizitätsmodul.

Schließlich erzeugen wir Siliziumleerstelle ($V_{Si}$) durch Helium-Breitstrahl-Implantation und charakterisieren die mechanischen Eigenschaften nach jedem Implantationsschritt. Wir untersuchen die Veränderung der Spannung und des Elastizitätsmoduls mit Fluenzen von $\Phi{=}1 \times 10^{12}\,\mathrm{cm}^{-2}$, $1 \times 10^{13}\,\mathrm{cm}^{-2}$ und $1 \times 10^{14}\,\mathrm{cm}^{-2}$ bei einer Energie $E_\mathrm{I}{=}14\,\mathrm{keV}$. Der Elastizitätsmodul bleibt durch die Helium-Ionen-Implantation unverändert. Die Veränderung der Zugspannung ist bei der niedrigsten Ionenfluenz vernachlässigbar, bei der Einzelne oder Ensembles von $V_{Si}$ erzeugt werden. Bei der höchsten Implantationsfluenz $\Phi{=}1 \times 10^{14}\,\mathrm{cm}^{-2}$ lässt die Spannung jedoch um 30% nach.

# Contents

# Nomenclature

## Abbreviations

| | |
|---|---|
| CB | Conduction band |
| CMOS | Complementary metal-oxide semiconductor |
| CVD | Chemical vapour deposition |
| DFT | Density functional theory |
| DW | Debye-Waller factor |
| $E_I$ | Energy of (He) ions |
| EBL | Electron beam lithography |
| ES | Excited state |
| fcc | Face-centred cubic |
| FIB | Focused ion beam |
| FPI | Fabry-Pérot interferometer |
| GS | Ground state |
| He | Helium |
| HF | Hydrogen fluoride |
| ICP-RIE | Inductively coupled plasma-reactive ion etching |
| IP | in-plane mode |
| IPA | Isopropyl alcohol |
| MACEtch | Metal-assisted chemical etching |
| MEMS | Microelectromechanical systems |
| MIBK | Methyl isobutyl ketone |
| MS | Metastable state |
| NV | Nitrogen-vacancy centre |

| | |
|---|---|
| ODMR | Optically detected magnetic resonance |
| OOP | out-of-plane mode |
| PL | Photoluminescence |
| PSB | Phonon sideband |
| QPIC | Quantum photonic integrated circuits |
| RTA | Rapid thermal annealing |
| SEM | Scanning electron microscopy |
| Si | Silicon |
| SiC | Silicon carbide |
| $SiO_2$ | Silicon oxide |
| SOI | Silicon-on-insulator |
| SPE | Single-photon emitter |
| SRIM | Stopping and range of ions in matter |
| TIR | Total internal reflection |
| VB | Valence band |
| ZFS | Zero field splitting |
| ZPL | Zero-phonon line |

## Symbols

| | |
|---|---|
| $\Delta$PL | Change in photoluminescence |
| $\varnothing$ | Diameter |
| $\epsilon$ | Strain |
| $\Gamma$ | Damping rate |
| $\mu_B$ | Bohr-magneton |
| $\nu_{RF}$ | Frequency of radio waves |
| $\Phi$ | Ion fluence |
| $\phi$ | Schottky barrier |
| $\rho$ | Density |
| $\vec{B}$ | Magnetic field |
| $\wedge$ | Full width at half maximum |
| $C$ | Compliance |

| | |
|---|---|
| $g_e$ | Landé-factor of the electron |
| $S$ | Stiffness |
| $C_i$ | Carbon interstitial |
| $C_s$ | Carbon substitutional |
| $E_g$ | Bandgap energy |
| $m_S$ | Spin magnetic quantum number |
| $R_p$ | Projected range |
| S | Magnitude of spin angular momentum $\vec{S}$ |
| $Si_i$ | Silicon interstitial |
| $V_C$ | Carbon vacancy |
| $V_{Si}$ | Silicon vacancy |

# Chapter 1

# Thesis Overview

Quantum technology can help solve real-world social and economic challenges. For example, it can achieve higher sensitivity, lower power consumption, and enhanced security, among other benefits[1,2]. As we are reaching the limits of a few atoms for electronic and optoelectronic device applications, we can use point defects to overcome the limitations related to miniaturisation and go beyond. Laws of quantum mechanics govern the rules of such systems, and one can consider point defects as the basic building blocks for quantum technologies. This work is based on the idea of using point defects in solids to realise a system which will pave its way towards future quantum technologies[3].

Chapter 2 introduces the motivation of this doctoral work related to quantum communication and sensing. What quantum technologies are, how quantum systems appear, and their usefulness are introduced. Afterwards, the idea of two projects—one focusing on quantum photonic integrated circuits for quantum communication and the other—hybrid spin-mechanical systems for quantum sensing is described.

Chapter 3 introduces different crystal defects with a focus on point defects. Next, the telecom photon emitting G-centre in silicon (Si) as a single-photon source is discussed. The working mechanism and ion implantation techniques to create G-centres are explained. The subsequent section introduces the silicon vacancy in silicon carbide (SiC) and optically detected magnetic resonance (ODMR) for magnetic field sensing. Here, the idea is to realise hybrid spin-mechanical systems, which motivates the second project. Later, nanomechanics is introduced as an equally contributing part of our hybrid system. Additionally, how defects affect the mechanical properties is explained.

Experimental techniques for fabricating and characterising nanostructures are described in Chapter 4. First, the protocol for fabricating silicon nanopillars is described. Also, the motivation and working principle of metal-assisted chemical etching are explained. Next, fabrication steps for creating mechanical nanoresonators in silicon carbide are presented. Afterwards, the mechanism and the experimental setup of PEC etching to etch 4H-SiC dopant-selectively are described. A Fabry-Pérot interferometer characterises nanomechanical resonators, and the experimental technique is explained. At last, technical details of the helium ion implanter, which is used to create $V_{Si}$, are presented.

Chapter 5 presents the key results of this doctoral research. First, the optimisation of EBL and MACEtch for fabricating nanopillars in silicon is explained. Afterwards, the results of PL measurements followed by carbon implantation in pillars are described. Improvement in spectroscopic properties due to the waveguiding effect is reported. Additionally, an approach to create G- and W-centres on a wafer-scale is presented.

The second part of Chapter 5 presents the fabrication and characterisation of nanomechanical resonators in SiC. First, the initial results from PEC etching to fabricate 4H-SiC resonators are reported. Subsequent sections describe the characterisation of 3C-SiC resonators and the methods to determine stress and Young's modulus. Afterwards, I present SRIM simulation results to plan the implantation experiments and estimate $V_{Si}$ and $V_C$ defect density distribution in the resonators. Finally, the effect of helium ion implantation on stress and Young's modulus is described. In the last Chapter 6, I conclude the doctoral research work and briefly outline the future scope.

# Chapter 2

# Introduction

## 2.1 Quantum Technology

Quantum physics pertains to the behaviour of atomic and subatomic systems, which defies explanation by the rules of classical physics. Generally, quantum technologies exploit aspects of quantum physics to improve classical systems in terms of performance, processing, size, functionalities, and cost. Quantum technology can help solve real-world social and economic challenges. For example, it can achieve higher sensitivity, lower power consumption, and enhanced security, enabling maintenance-free operation for industrial facilities, among other benefits. Computing, simulation, communication, and sensing and metrology are the four pillars of quantum technology and this work is focuses on the last two.

First-generation quantum technologies, such as transistors and lasers, were succeeded by computers and the Internet, ushering in progressive global changes. Efforts are underway to establish an infrastructure for a global quantum internet, thereby fostering the growth of quantum technologies. Initiatives in quantum technology receive substantial financial backing globally, encompassing countries like the United States, the United Kingdom, Europe, and China, with contributions from both large multinational corporations and start-up companies[1,2,4–6].

Current quantum technologies introduce novel capabilities and performance enhancements by leveraging quantum phenomena, including entanglement[7], teleportation[8–10], the Heisenberg uncertainty principle, and the no-cloning theorem[11], along with many-body effects[6]. Practical applications can be found in areas such as sensing[12,13], metrology[14–16], navigation and timing[17], state discrimination[18,19], communication[20,21], and computation[1,4,22].

## 2.2 Quantum Communication

Quantum communication serves as a channel for transmitting information using quantum principles. It can enhance classical information transfer through quantum channels or facilitate the transfer of quantum states for various quantum applications. The primary applications of quantum communication include secure communication, long-term secure storage, cloud computing, cryptography, connecting remote devices and systems, and establishing a secure quantum network capable of distributing resources such as entanglement and randomness.[2,5].

The most efficient approach to scaling up and advancing real-life quantum technologies is chip-scale integration, akin to classical photonics. For instance, the development of quantum photonic integrated circuits (QPIC) focuses on the monolithic, hybrid, or heterogeneous integration of the available components. Key features provided by QPICs include scalable and fast reconfigurable architecture[23,24], on-demand enhanced light-matter interaction, stable optical elements[25], direct on-chip co-integration with efficient single-photon detectors[26,27], and complementary metal-oxide semiconductor (CMOS) electronic readout with feedforward control[28,29].

Photons are ideal information carriers for on-chip quantum communication technologies owing to their long coherence time, weak interaction with the environment, and high speed. Photons can work as qubits in regards to their polarisation, path, quantity, or arrival time[6]. Also, photons as information carriers offer key advantages for other tasks like information processing[30], computing[31], and communication[32]. Photonic devices aim at generating, manipulating, storing, and detecting quantum states of light. Therefore, QPICs will play a critical role in the evolution of next-generation quantum technologies[28].

The monolithic integration of single-photon sources and detectors, alongside reconfigurable elements, will be a step towards QPIC. The ultimate goal is to deploy a photonic quantum processor compatible with current silicon technology, ensuring a cost-effective and technologically efficient solution in yield and reproducibility. To that end, elements required for cryogenic QPICs, such as superconducting single-photon detectors, delay lines, modulators, phase shifters, and other elements, are already available[23,27,33–35]. The only missing link is a single-photon source in silicon.

Telecommunication wavelengths are suitable for efficient communication through optical fibres where the propagation losses are minimum[36]. Therefore, to develop a monolithically integrated QPIC and to exploit the existing silicon CMOS architecture, on-demand telecom single-photon sources in silicon become essential. Recently, a wide variety of single-photon emitting radiation damage centres have

been demonstrated in silicon, including G-centres and W-centres[37–44]. To bring such single-photon sources closer to their practical applications, their scalability, brightness, and collection efficiency need to be improved.

Therefore, part of this doctoral work is dedicated to fabricating nanopillars without introducing optically active defects emitting in the telecom O-band. To this end, we have employed a fabrication protocol including metal-assisted chemical etching (MACEtch). The development of MACEtch was a significant task in this thesis. In the following step, we implant carbon in fabricated pillars using broad-beam implantation. We confirm from spectroscopic measurements that G-centres are integrated into pillars with improved emission due to the waveguiding effect. In addition, we create G-centres and W-centres by fabricating a photoresist mask with lithographically defined arrays of nanoholes, followed by a broad beam silicon implantation. We hope this work brings us closer to the monolithic integration of QPICs based on silicon architecture.

## 2.3 Quantum Sensing

Sensors are crucial for technology as they form the basis of science, where quantitative assessment is required, as well as commerce for exchanging goods. Quantum sensors are single or ensembles of systems that use quantum phenomena like coherence, superposition, interference, and entanglement to measure physical quantities of interest with precision higher than achievable by classical alternatives. Quantum sensors exploit quantum systems' sensitivity to external disturbances such as electric and magnetic fields, stress, and temperature. The potential of quantum sensors for ultra-sensitive measurement devices makes them an inherent part of future technologies[1,5,45–49].

Current advanced nanofabrication techniques allow the coupling of mechanical resonators to electromagnetic radiation, integrating mechanical resonators in optical cavities[50,51] or superconducting microwave circuits[52–54] which makes optomechanical systems a potential candidate for tomorrow's quantum technologies. Mechanical motion can be coupled to various quantum systems such as photons and spin systems[55–57].

Similarly, electron and nuclear spin degrees of freedom can be used as qubits, a two-level quantum system, from atomic and molecular spins in solids such as colour centres and deep donors. They provide long coherence times as they are well-shielded from the environment and can hold quantum properties longer. The most promising and advanced platform so far is the nitrogen-vacancy (NV) centres in diamonds.

The current quantum systems consist of elements ranging from single photons, atoms, ions, individual electrons, or nuclear spins to mesoscopic and nanomechanical devices. Identifying a system that meets all of the criteria, such as coherence, coupling, and processability, and is suitable for most of the current quantum systems is demanding. Therefore, to utilise the available expertise for developing next-generation quantum systems, one can combine the strengths of two or more systems to make a hybrid system. Such next-generation hybrid quantum systems should be able to simultaneously perform various tasks reliably, like storing, processing, and transmitting information[6,36,56,58–62].

The prevailing critical benchmarks for sensors of this kind necessitate high sensitivity and spectral resolution, requiring long spin coherence times. NV centres in diamond allow for millisecond coherence times under ambient conditions, making them the optimal choice for spin-based sensing. Despite their proven potential in biomedical applications[5,45,49], industrial growth techniques for diamond wafers are immature. Also, device processing remains challenging due to its large bandgap and high electric resistance. So the big question 'What is the next suitable material?' hosting spin centres and wafer-scale possibilities is answered below, inspiring our research work.

The motivation behind the second part of this doctoral work is to realise a hybrid spin-mechanical system with SiC for detecting small magnetic fields with higher precision[57]. The mechanical system is associated with a doubly clamped resonator or a membrane. The spin system originates from silicon vacancies, which can be deterministically created using ion implantation techniques.

In our work, we have fabricated resonators in 3C-SiC using top-down fabrication. The unique properties of the 3C-SiC film grown on Si, which is under tension due to differences in the lattice constants and thermal expansion coefficients of Si and SiC, lead to high mechanical quality (high-Q factor) resonators. This high-quality system provides a promising platform to study changes in the mechanical properties that result from defect creation or engineering, potentially revolutionising the field of material science. On the other hand, the spin system is attributed to the silicon vacancies ($V_{Si}$) in SiC. We use broad beam helium ion implantation to create $V_{Si}$. As a consequence of defect creation, the material properties can change, affecting the device performance. However, the effect of helium ion implantation with the motivation to create silicon vacancies on nanomechanical resonators in SiC has not been reported to date. Our work fills this gap by investigating the accumulated effect of helium ion implantation on the mechanical response of 3C-SiC nanoresonators. In particular, we focus on changes in stress and Young's modulus with incremental helium ion fluence.

# Chapter 3

# Theory Basics

## 3.1 Crystal Defects

Ideally, a crystalline material has a specific order of constituents in all directions. Any deviation from such a perfect arrangement is a crystal defect. All solids have defects and can influence the electrical, mechanical, and optical properties of the materials. Defects are formed during the growth process or artificially created by irradiation techniques.

Generally, defects are classified depending on their dimensionality: three-dimensional or volume defects (pores, cracks, inclusions), two-dimensional or plane defects (stacking faults), one-dimensional or line defects (edge and screw dislocations), zero-dimensional or point defects (vacancies, interstitials, substitutionals, antisites, Frenkel pairs). As our work focuses solely on point defects, a brief introduction is provided below.

Figure 3.1 shows a schematic of various point defects: vacancy, interstitial, substitutional and antisite. The defect is called a vacancy if an atom is missing from its lattice position. Vacancies can possess different charged states and consequently have different properties. A foreign atom can occupy a vacant position, which is a substitutional defect. In compound semiconductors, if an atom of type A replaces an atom of type B at its lattice position, then it is an antisite A denoted by $A_B$. In the case of interstitials, the host atom takes a non-lattice position. Frenkel pairs are a combination of an interstitial and a vacancy. Depending on whether the defect is caused by a host atom or by a foreign atom, the defect is intrinsic or extrinsic.

Point defects can occur naturally or be created artificially. Radiation damage is one of the most effective methods to artificially create point defects, as it provides precision and control at the nanoscale. Therefore, they are also referred to as radiation-damage centres. Another criterion for classification is related to the position of the introduced additional energy level in the material's band gap. Shallow levels are near the bottom of the conduction band for donors or near the top of the valence band for acceptors, and they are suppliers of carriers. The long-range Coulomb potential of the defect produces shallow levels. Deep levels are near the centre of the forbidden energy gap, and they are formed by vacancies, substitutionals, interstitials, and antisites. Deep levels are defined as being produced by the short-range central cell potential of the defect. They act as recombination centres and traps.

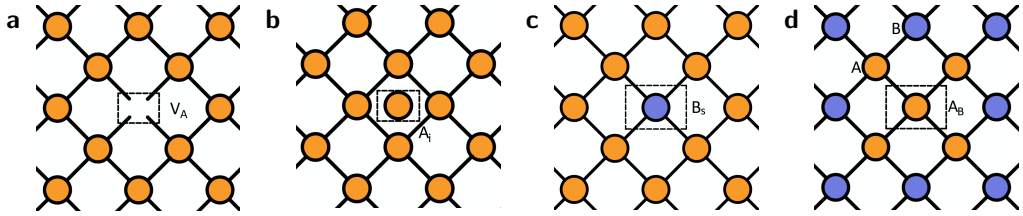


**Fig. 3.1: Schematic of various point defects (2D representation).** (a) A missing atom from the host matrix is a vacancy ($V_A$). (b) An atom can move to occupy a non-lattice position to form an interstitial. When the host atom leaves the lattice site, it is called self-interstitial ($A_i$). (c) A foreign atom at a lattice site is a substitutional imperfection ($B_S$). (d) In compound elements, if an atom of type A replaces an atom of type B at its lattice position, it is an antisite $A_B$.

Colour centres are a particular type of point defect or point defect complex. They introduce additional energy levels within the bandgap of the host material, which leads to sub-bandgap absorption. Generally, they form when point defects trap electrons with energy levels near optical frequencies. These are deep-levels, and their theoretical analysis is complex[63–66]. Next, let us discuss two defect centres: G-centres in silicon and $V_{Si}$ in silicon carbide.

## 3.2 G-centres in Silicon

The silicon crystal consists of only the chemical element Si with an atomic number 14 from group IV of the periodic table[67]. Si is the most abundant material in the earth's crust ($\sim$28%)[68,69] and holds the most significant share in the electronics market. Czochralski and float-zone techniques are used for the growth and manufacturing of monocrystalline growth and isotopic purification[67,70–72].

Si crystal has a diamond structure with two atoms in a primitive cell[73]. The Si lattice consists of two penetrating face-centred cubic lattices (fcc) with lattice constant $a_{Si}$=5.43 Å. Each Si atom is surrounded and covalently bonded by four Si atoms, making $sp^3$ hybridisation according to the orbital theory.

### 3.2.1 Telecom Photon Emitters

The early studies of luminescent centres in silicon can be traced back to the early 1960s, and since then, their origin, properties, and investigation methods have been studied[74]. In recent years, optically active point defects have gained attention due to their application in quantum communication and photonics. Si does not allow efficient photoluminescence (PL) emission due to its indirect bandgap. However, point defects allow sub-bandgap emissions.

Table 3.1 summarises known radiation damage colour centres in Si and their properties[75]. Five radiation damage centres emit in the telecom band, except the X- and W-centres. In this work, I will focus on centres emitting in the telecom band, particularly G-centres, due to their excellent spectroscopic properties: bright emission in the telecom O-band, low losses, and high oscillator strength.

**Table 3.1: Summary of radiation-damage centres in silicon.** The atomic configuration, zero phonon line (ZPL) wavelength and energy, and telecommunication sub-band category of the colour centre are mentioned. Emissions from X- and W-centres are not in the telecom band. The exact atomic configuration of I- and P-centres has yet to be identified. Adapted from the Reference [75].

| colour centre | X | W | G | I | T | C | P |
|---|---|---|---|---|---|---|---|
| Configuration | $4Si_i$ | $3Si_i$ | $2C_s$-$Si_i$ | - | $2C_s$-$H_i$ | $O_i$-$C_i$ | - |
| Wavelength (nm) | 1192 | 1218 | 1278 | 1284 | 1326 | 1570 | 1616 |
| Energy (meV) | 1040 | 1018 | 970 | 966 | 935 | 789 | 768 |
| Telecom sub-band | - | - | O | O | O | L | L |

### 3.2.2 Atomic Configuration and Working of G-centres

Like other radiation damage centres, G-centres are a complex of point defects or artificial atoms that create deep-level photoactive states in the bandgap of silicon. The formation of deep-level states makes sub-bandgap transitions possible. Among several configurations of G-centres, only one is optically active.

An optically active G-centre is a triatomic complex of two substitutional carbons ($C_s$) bonded to a silicon interstitial ($Si_i$) in Si. In the 1960s, G-centres were discovered due to radiation damage caused by bombarding silicon with electrons and ions. Then, it was known that the 1278 nm emission is due to a radiation-induced deep-level point defect complex. However, the exact configuration of G-centre was unclear[76–78]. Currently, it is accepted that the G-centre is a $C_s$-$Si_i$-$C_s$ complex distorted from the <111> bond axis having a neutral charge as shown in Figure 3.2[37,38,41,79–82] and recently also confirmed by density functional theory (DFT) calculations[83].

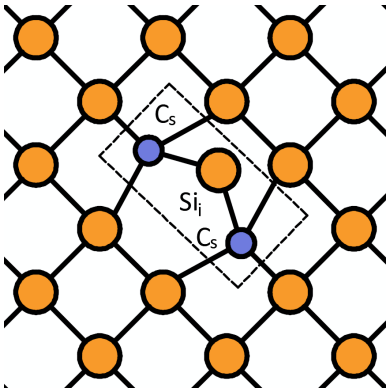


**Fig. 3.2: Atomic configuration of the G-centre (2D representation).** Schematic illustration of the atomic configuration of the G-centre embedded in the silicon matrix.

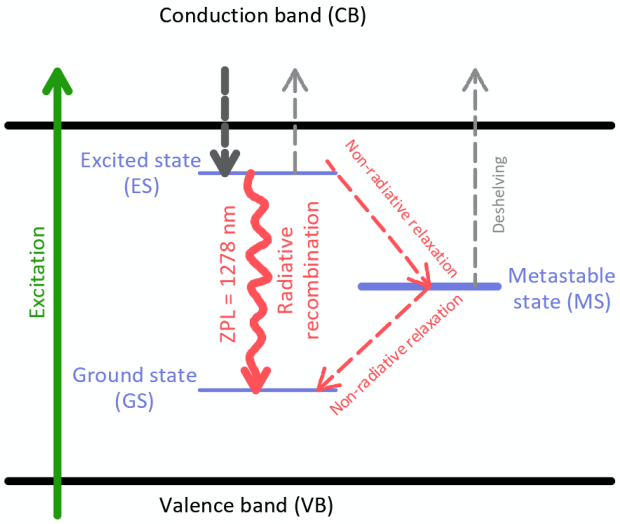


**Fig. 3.3: Energy level scheme of the G-centre.** The G-centre can be excited optically using above bandgap laser illumination. The energy difference between the ground state (GS) and excited state (ES) corresponds to a zero phonon line (ZPL) emission of 1278 nm and energy 970 meV.

The working principle of the G-centre can be described by a three-level model[84,85], as shown in Figure 3.3. A laser excites an electron from the ground state (GS) of the G-centre into the conduction band (CB). These electrons from CB can drop to the excited state (ES) of the G-centre. A radiative recombination process from

the ES to the GS results in a 1278 nm G-line emission, corresponding to energy 970 meV. A non-radiative relaxation possibly occurs via a metastable state (MS). The deshelving process of the ES or MS into the CB can take place by the laser, and it can be explained by a four-level model[86,87]. The direct excitation from the valence band (VB) to CB recharges the G-centre.

The optical transitions in the G-centres are accompanied by non-radiative channels, which result in the shifting of the spectrum towards longer wavelengths and are called phonon sidebands (PSB). The zero-phonon line (ZPL) is a sharp peak resulting from purely electronic transitions without phononic contributions. The energy difference between the ground state (GS) and excited state (ES) is 970 meV, corresponding to 1278 nm ZPL emission in the telecom O-band.

### 3.2.3 Creation of G-centres

Radiation damage centres can be created by high-energy electrons, ions, protons, or gamma rays with additional annealing protocols. For creating G-centres, a combination of electron, proton, or ion irradiation with different annealing techniques are used. The specific steps and their sequence also depend on the residual carbon impurities in the silicon wafer.

The formation of G-centres occurs in the following steps. High-energy irradiation can create $Si_i$ to kick out $C_s$ and form $C_i$ or directly form $C_i$ by irradiated species. Mobile $C_i$ can thus form defect complexes[80]. The annealing step removes the radiation damage and brings back carbon into $C_S$. Pre-annealing can also be used to reduce background noise, which can affect the spectroscopic measurements[41].

Berhanuddin and others have employed multi-step carbon implantation, rapid thermal annealing (RTA) and proton irradiation on n-type Si wafers with residual carbon to create G-centres[79]. Also, Chartrand and colleagues have created G-centres in isotopically purified $^{28}C$ samples with low levels of carbon impurities using electron irradiation and annealing[81]. Furthermore, Beaufils and others performed carbon implantation followed by annealing and proton irradiation to create ensembles of G-centres in a silicon-on-insulator (SOI) wafer[82]. Recently, we have created ensembles of G-centres in $^{nat}Si$ with only single-step carbon implantation[40]. Also, single G-centres in SOI were created using single-step carbon irradiation[38] and focused ion beam silicon implantation[41] in carbon-rich silicon without annealing.

To confirm single-photon emission, photon statistics distribution can be recorded using Hanbury, Brown and Twiss (HBT) interferometry experiments, which have become the standard. The temporal properties of light are described in the second-order autocorrelation $g^{(2)}(\tau)$-function. The $g^{(2)}$ also gives insights into

the emitter's energy level scheme and purity. More importantly, $g^{(2)}(\tau)<0.5$ unambiguously represents single-photon emission and proves the existence of only one single-photon emitter. More details on the $g^{(2)}(\tau)$ function are omitted at this point and can be found elsewhere[75].

## 3.3 Silicon Vacancy in Silicon Carbide

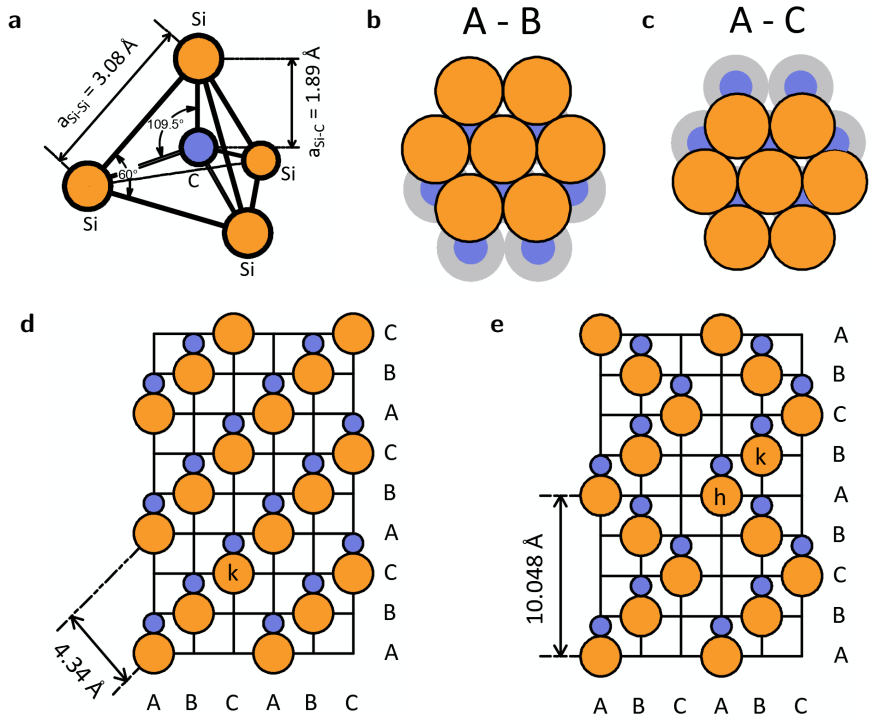


**Fig. 3.4: Silicon Carbide: Crystal Structure and Polytypism.** (a) Si (orange) and C (blue) are bonded in a tetrahedron with $a_{Si\text{-}Si}$=$a_{C\text{-}C}$=3.08 Å and $a_{Si\text{-}C}$=1.89 Å[88] with $\alpha_{Si\text{-}Si\text{-}Si}$=60° and $\beta_{Si\text{-}C\text{-}Si}$=109.5°. (b) A-B and (c) A-C are the two layer-stacking possibilities. Grey and orange circles are Si atoms at the bottom and top stacking layers. The smaller blue circles are C atoms in between the two Si layers. (d) 3C-SiC and (e) 4H-SiC stacking sequences are shown with ABC-ABC and ABCB-ABCB formations in the vertical direction. In the horizontal direction, all the polytypes have an ABC-ABC formation[89–91].

Silicon carbide (SiC) has been a material of interest due to its unique electric, thermal, and mechanical properties. SiC is a wide bandgap semiconductor ($E_{g(3C\text{-}SiC)}$=2.2 eV, $E_{g(4H\text{-}SiC)}$=3.23 eV) with high melting point (2800 °C), high thermal conductivity (3.6 W cm$^{-1}$ °C$^{-1}$), high thermal expansion coef-

ficient ($\sim 10^{-6}\,K^{-1}$), high breakdown field ($\sim 10^6\,V\,cm^{-1}$), low surface oxidation at room temperature[92] and its inertness to corrosive environments[93]. SiC is one of the strongest materials, with a hardness 9 on the Mohs scale and a Young's modulus of 450 GPa. SiC is used for applications in harsh environments at high temperatures and pressures, high frequencies, strong radiation and corrosive environments, power devices, and aerospace, automotive, and petroleum industries.

SiC is a crystalline direct bandgap semiconductor of two group IV elements: silicon ($_{14}$Si) and carbon ($_6$C), and it is the only stable compound of Si and C[94]. Si and C are bonded in a tetrahedron by $sp^3$ hybrid orbitals where Si atoms are at the corners and C at the centre, or vice versa, as shown in Figure 3.4a. SiC can exist in different crystallographic structures with the same chemical formula, and this property is called polytypism. The polytypes are identical in two dimensions but differ in the third. If a layer is arranged in the dents of the previous layer, two different possibilities exist A-B or A-C, as shown and explained in Figure 3.4b and Figure 3.4c, respectively. The stacking sequence along the symmetry axis (c-axis) determines the properties of the material[95].

SiC exists in about 250 polytypes, classified according to Ramsdell's notation. Because of the ease of manufacturing processes, three polytypes are popular: 3C-SiC, 4H-SiC, and 6H-SiC[96]. Number and letter define the periodicity in the stacking sequence and the crystal symmetry (C-cubic, H-hexagonal, and R-rhombohedral), respectively. A cubic SiC was also called $\beta$-SiC, and a hexagonal or rhombohedral SiC was $\alpha$-SiC. For 3C-SiC stacking, the order repeats after every three layers (ABC). 4H-SiC and 6H-SiC have a sequence of four (ABCB) and six (ABCACB) layers, respectively[90,91,97,98]. In this thesis, the discussion is limited to only 3C-SiC and 4H-SiC. Their stacking sequence is shown in Figures 3.4d and 3.4e.

### 3.3.1 Atomic Configuration and Working of $V_{Si}$

The silicon vacancy ($V_{Si}$) is a missing silicon atom from its lattice position. Point defects like $V_{Si}$ introduce discrete energy levels within the band gap of SiC and possess a net electron spin. These properties make $V_{Si}$ sensitive to optical and spin-dependent measurements. Figure 3.5a shows $V_{Si}$ in 4H-SiC at a hexagonal position with its surroundings and energy scheme. $V_{Si}$ in 4H-SiC can be in hexagonal (h) or cubic (k) environments and are denoted by $V_{Si}$(h) or $V_{Si}$(k), respectively. Influenced by different environments ,$V_{Si}$(h) or $V_{Si}$(k) introduce different energy gaps: 1.352 eV and 1.438 eV, respectively[99]. Therefore, their photoluminescence lies in the near-infrared band. Also, another essential property of $V_{Si}$ is its spin state, which I will elaborate on next.

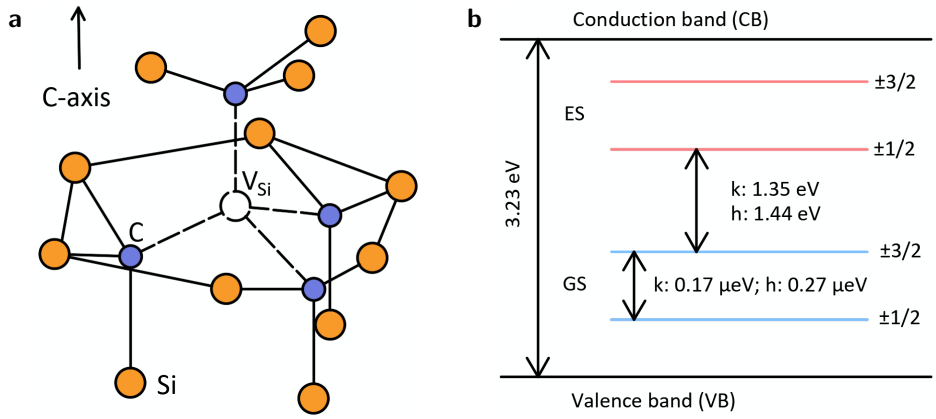


**Fig. 3.5: Atomic configuration and band diagram of $V_{Si}$ in 4H-SiC.** (a) Schematic of $V_{Si}$ in a hexagonal (h) environment with the four $sp^3$ dangling bonds at the tetrahedral aligned carbon atoms. (b) The energy band diagram of $V_{Si}$ embedded in 4H-SiC crystal shows the corresponding energy difference for h and k positions of $V_{Si}$. Adapted from Reference [91].

The electron system of optically active silicon vacancies possesses an overall spin of S=3/2[100]. A neutral silicon vacancy is surrounded by four carbon $sp^3$ dangling bonds. However, this configuration would lead to an S=1 system. That means optically active $V_{Si}$ must be negatively charged to have S=3/2 state. For simplicity, negatively charged silicon vacancy is will be denoted by $V_{Si}$ in the subsequent sections. The ground state (GS) and excited state (ES) of the $V_{Si}$ are split by their magnetic quantum number into $m_S$=±3/2 and $m_S$=±1/2 states. This is called zero-field splitting (ZFS) and corresponding energy gap is different for h (0.27 μeV) and k site (0.17 μeV) as shown in Figure 3.5b[91,98,101].

$V_{Si}$ shows a preferred population of a spin state within the GS under optical excitation or pumping and is proven theoretically[102] and experimentally[103]. The preferential population is due to the non-radiative recombination path via the metastable state (MS) between the GS and ES. One of $m_S$=±3/2 and $m_S$=±1/2 is preferred depending on the polytype and the vacancy site. $m_S$=±1/2 for $V_{Si}$(h) is preferentially populated, and such overpopulation of one spin sublevel compared to another is called spin alignment[103].

When an electron is excited from one of the GS spin levels to a corresponding ES spin level by laser light, two relaxation mechanisms can occur, and their transition rates depend on the magnetic quantum number of the ES. It is important to note that the excitation and radiative recombination are spin-conserving. $m_S$=±3/2 level favours the direct radiative or luminescent relaxation. In contrast, non-radiative or non-luminescent relaxation is more likely from $m_S$=±1/2 via MS.

Transitions between states with different spin quantum numbers, also called intersystem crossing, can take place when electrons relax from MS to GS, populating the $m_S = \pm 1/2$ GS[100]. Figure 3.6 shows the optical cycle with continuous and dotted lines representing radiative and non-radiative transitions, respectively. The transition probabilities are represented by arrow thickness[91,98].

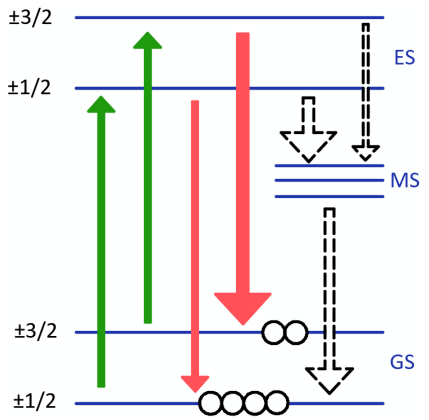


**Fig. 3.6: Energy diagram showing allowed transitions of $V_{Si}$ under optical excitation.** The upward green and downward red arrows represent excitation and luminescent (non-luminescent with black dashed arrows) transitions, respectively. The thickness of the arrows represents transition probabilities. Abbreviations used are GS for ground state, MS for metastable state and ES for excited state of the $V_{Si}$. Adapted from Reference [91].

Like other radiation damage centres, $V_{Si}$ can be created by high-energy electrons, ions, or protons with additional annealing protocols. Widmann and Nagy, with their colleagues, have reported the creation of $V_{Si}$ with excellent spectroscopic properties by 2 MeV electron irradiation[104,105]. Furthermore, mid- to high-energy neutron irradiation was employed to create $V_{Si}$ for engineering near-infrared single-photon emitters[87]. However, the distribution of the defects cannot be controlled by such broad beam implantation techniques where a complete sample surface is exposed to the defect-creating species. This makes integration of $V_{Si}$ in devices difficult.

Position control of defect centres can be achieved by lithographically patterning a mask followed by broad-beam implantation[106–108]. However, they are associated with limitations on implantation depth and lithographic processing intricacies. In addition, techniques have been developed to create colour centres by maskless laser writing[109] and focused ion beam (FIB)[110–112].

### 3.3.2 Optically Detected Magnetic Resonance

Optically detected magnetic resonance (ODMR) is an indirect detection method where the spin-sensitive photoluminescence (PL) measures the spin state of an electron. The basis of ODMR lies in detecting changes in PL from the luminescent relaxation of the electrons, which are excited from ground state (GS) to excited state (ES) with RF waves. The details of the process are as follows.

In the case of $V_{Si}$ in 4H-SiC, the spin aligns in the $m_S$=±1/2 GS under continuous optical pumping, as shown in Figure 3.6. The luminescent relaxation from ES into $m_S$=±3/2 GS is more likely than into $m_S$=±1/2 GS. Therefore, if electrons are being transferred from the preferably populated $m_S$=±1/2 GS into the $m_S$=±3/2 GS, there must be more electrons relaxing via the luminescent path in the next pumping cycle. A change in PL ($\Delta PL$) can then be monitored with respect to the previous optical cycle. The electronic transitions from $m_S$=±1/2 GS to $m_S$=±3/2 GS can be activated by applying radio waves (RF) to the sample having energy equal to ZFS. For $V_{Si}$(h), ZFS=0.27 μeV≡70 MHz. Figure 3.7a shows an example of excitation using the RF waves to explain the working principle and is explained in the following[91].

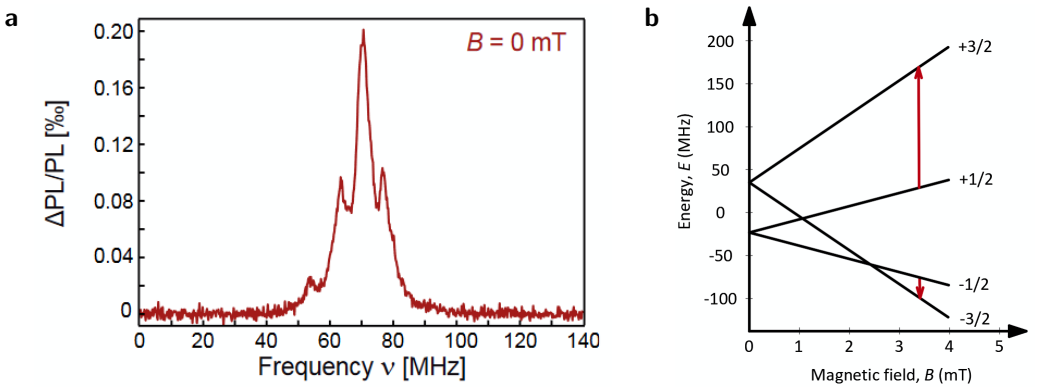


**Fig. 3.7: PL measurement and Zeeman splitting of $V_{Si}$(h) in 4H-SiC.**
(a) Electrons from optically pumped $m_S$=±1/2 GS are excited to $m_S$=±3/2 GS using resonant radio waves. ΔPL/PL is plotted against the radio frequency, showing a peak at RF=ZFS. (b) Primary degenerate $m_S$=±1/2 and $m_S$=±3/2 grounds states (GS) are split under the influence of an external magnetic field $\vec{B}$ along the c-axis. Under the application of RF waves two possible transitions with $\Delta m_S$=±1 can be induced for all $B$. Adapted from Reference [91].

In ODMR, the relative change in PL (ΔPL/PL) is measured versus the energy of the applied radio frequency. The radio frequency is swept iteratively under continuous optical pumping. At resonance ($f_{RF}$=ZFS), a change in the PL intensity is detected. Figure 3.7a shows an example of such a PL measurement, where ΔPL/PL versus applied radio frequency is plotted.

The final goal is to increase the magnetic field sensitivity of ODMR using spin-phonon coupling. Therefore, let us first briefly discuss the workings of the standard ODMR technique. Experimentally measured ODMR spectra in response to the external magnetic field $\vec{B}$ along the c-axis or symmetry axis of the crystal are described as follows.

When the $V_{Si}$ is influenced by the external magnetic field $\vec{B}$, the states $m_S$=±1/2 and $m_S$=±3/2 become non-degenerate as per the Zeeman effect. If $\vec{B}$ aligns with the c-axis, also the symmetry axis for $V_{Si}$, the energy levels split linearly with the magnetic field strength. The additional energy $E_{Zeeman}$ can be given by,

$$E_{Zeeman}^{m_S} = g_e \mu_B B \cdot m_S, \tag{3.1}$$

where $g_e$=2 is the Landé-factor of the electrons and $\mu_B$ the Bohr-magneton. Thus, the splitting for $m_S$=±3/2 is three times the splitting for $m_S$=±1/2, as shown in Figure 3.7b. Although all four spin states have different energies, the spins are still grouped into non-degenerate $m_S$=±1/2 states.

A change in PL is detected when the excitation radio frequency is resonant with a spin flip $\Delta m_S$=±1. The corresponding energy $\Delta E$ for $m_{S,1} \rightarrow m_{S,2}$ can be given by,

$$\Delta E = ZFS + (m_{S,2} - m_{S,1}) \cdot g_e \mu_B B = ZFS \pm 1 \cdot g_e \mu_B B. \tag{3.2}$$

Therefore, at resonance:

$$h\nu_{RF} \stackrel{!}{=} |\Delta E_{2,1}|, \tag{3.3}$$

where $\nu_{RF}$ is the radio frequency and $h$ the Planck constant. By inserting Equation 3.2 into 3.3, an ODMR signal at two distinct frequencies can be detected.

$$\nu_{RF}^{+1} = \left| \frac{ZFS + g_e \mu_B B}{h} \right|, \tag{3.4}$$

for the $+1/2 \rightarrow +3/2$ transition and

$$\nu_{RF}^{-1} = \left| \frac{ZFS - g_e \mu_B B}{h} \right|. \tag{3.5}$$

for the -1/2 → -3/2 transition. Even if the $-1/2 \leftrightarrow +1/2$ is theoretically possible following $\Delta m_S$=1, it cannot be detected because both the states are almost equally populated under optical pumping and the luminescent relaxation rates to the $m_S$=±1/2 GS states are the equal. Therefore, no change in PL is expected for these transitions. Figure 3.7b presents two experimental measurements, one for $g_e \mu_B B <$ ZFS and one for $g_e \mu_B B >$ ZFS. The distinct spectral positions of the transitions in ODMR give the magnetic field strength $B$[91].

### 3.3.3 Hybrid Spin-Mechanical Systems

Let us understand how a spin system can be coupled to a mechanical system to improve magnetic field sensing. Poshakinskiy and Astakhov have theoretically modelled a possibility to couple a spin system associated with the $V_{Si}$ in 4H-SiC with mechanical modes of an unstressed SiC membrane of dimensions 10 µm × 15 µm and thickness 1 µm having a mechanical quality factor $Q$=$10^4$. $V_{Si}$ are created at the centre of the membrane, close to the surface. Only the in-plane component of the wave vector is considered for out-of-plane and in-plane modes of the membrane[57].

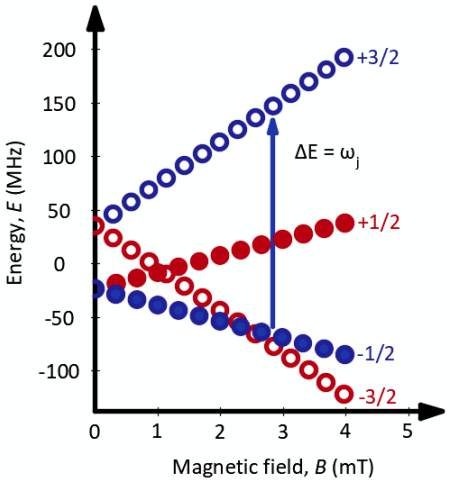


**Fig. 3.8: Spin-mechanical Magnetometry.** The fine structure of $V_{Si}$ in external magnetic field B. The solid (open) circles represent the preferentially populated (depleted) states under optical pumping. The vertical arrow shows the available spin transition frequency $\omega_j$ due to interaction with a membrane mode. Adapted from Reference [57].

When the energy difference between two spin sublevels matches a mechanical mode's frequency, the spin transition rate is enhanced. It leads to a faster spin-relaxation transition and a change in the steady-state number of vibrational quanta due to phonon absorption or emission. Next, an all-optical protocol to enhance the magnetic field sensitivity of such optically detected spin-mechanical resonance (ODSMR) is briefly discussed.

The optical cycle for realising ODSMR is shown in Figure 3.8. The spin states of $V_{Si}$ split and shift linearly when the external magnetic field $\vec{B}$ is applied along the c-axis. Under optical pumping, $m_S$=$\pm 1/2$ states are preferentially populated[113]. If the excitation is switched off, the spin relaxation $\pm 1/2 \rightarrow \pm 3/2$ takes place. This relaxation can involve the absorption or emission of single phonons at low temperatures, with a typical relaxation time of ∼10 s[114]. The spin relaxation process is accelerated by two orders of magnitude in certain magnetic fields when energy sublevel splitting equals the membrane eigenfrequency. This accelerated spin relaxation is attributed to the resonantly enhanced phonon emission or absorption probability. It is noteworthy that membrane vibrations can induce $\Delta m_S$=$\pm 1$ spin transitions, but with lower intensity as compared to $\Delta m_S$ due to the trigonal pyramidal asymmetry of $V_{Si}$.

The ODSMR detection scheme is similar to the standard ODMR mentioned in the previous sections, where $\Delta$PL/PL is measured and therefore not discussed here. Such an ODSMR scheme would lead to a sharp dip in the PL with full width at half maximum (FWHM) of 0.3 µT at 70 µT for time delay $\tau$=1 ms. For a typical ODMR with $V_{Si}$ in SiC, FWHM is around 100 µT[100]. For ODSMR, the magnetic field sensitivity depends on the mechanical quality factor $Q$ and spin relaxation time $T_1$, while in the case of ODMR, it depends on the spin coherence time $T_2$ of the $V_{Si}$. In short, for $T_1 \gg T_2$ and high $Q \gg \omega_j T_2$, ODSMR gives higher sensitivity, where $\omega_j$ is the frequency of the $j^{th}$ mode. For details about the theoretical background, mathematical formulation, and experimental protocol to realise ODSMR, interested readers can refer to the article - Optically detected spin-mechanical resonance in silicon carbide membranes[57].

## 3.4 Nanomechanics

In our hybrid spin-mechanical systems, the spin system in 4H-SiC is associated with the silicon vacancies ($V_{Si}$), which are created by helium ion implantation. The phononic system originates from nanomechanical doubly clamped resonators or strings. Therefore, the theory of nanomechanics is presented below.

The nanomechanical resonators fabricated in this work are freely suspended strings supported at both ends by clamping pads. They have two vibrating directions or flexural modes: out-of-plane (OOP) and in-plane (IP) directions, also called modes, and are shown in Figure 3.9. The Euler-Bernoulli beam theory developed in the $18^{th}$ century mathematically describes OOP and IP modes. The mathematical derivation and surrounding information can be found elsewhere[115]

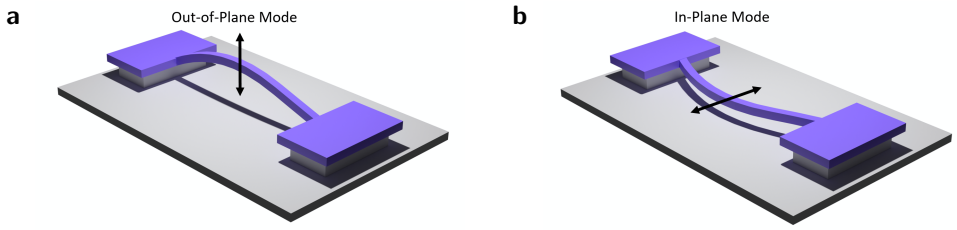


**Fig. 3.9: Out-of-plane and in-plane modes of a doubly clamped resonator.** (a) The resonator vibrates in a direction perpendicular to the sample. (b) In the IP mode, the resonator vibrates in a direction parallel to the sample.

The Euler-Bernoulli beam theory works best for prismatic beams ($l/h > 10$, where $l$ is the length and $h$ is the thickness of the resonator in the direction of vibration) with negligible rotational inertia and shear deformation. For our

doubly clamped beams with tensile stress in an elastic material (obeying Hooke's law), the equation of motion is given by[115],

$$EI\frac{\partial^4 u(x,t)}{\partial x^4} - \sigma A\frac{\partial^2 u(x,t)}{\partial x^2} + \rho A\frac{\partial^2 u(x,t)}{\partial t^2} = 0, \tag{3.6}$$

where $u(x,t)$ is the displacement, $x$ is the position along the beam, $t$ is the time, $E$ is Young's modulus, $I$ is the area moment of inertia, $A$ is the beams cross-sectional area and $\rho$ is the density of the material. By analytically solving the above equation, one can theoretically find the eigenfrequency of the out-of-plane modes (or IP modes by replacing thickness $h$ by width $w$ of the resonator)[115]:

$$f(n) = \frac{n^2\pi}{2L^2}\sqrt{\frac{Eh^2}{12\rho}}\sqrt{1+\frac{12\sigma L^2}{n^2\pi^2 Eh^2}}, \tag{3.7}$$

where $n$ is the mode number, $l$ is the length, $h$ is the thickness, $\rho$ is the density, $\sigma$ is the tensile stress, and $E$ is the Young's modulus.

$$\text{If} \qquad \frac{12\sigma L^2}{n^2\pi^2 Eh^2} \ll 1, \tag{3.8}$$

which holds true for high tensile stress and low mode numbers, Equation 3.7 simplifies to the string model.

$$f(n) \approx \frac{n}{2L}\sqrt{\frac{\sigma}{\rho}}. \tag{3.9}$$

Therefore, frequency scales linearly with mode numbers[116] and inversely with length, also verified by our experimental results.

### 3.4.1 Driven Harmonic Oscillator

A driven and damped string resonator can be described as a harmonic oscillator. To that end, the resonator is reduced to a point mass having effective mass $m_{eff}$ ($\propto$m), resonator geometry, and the mode. The equation of motion for a driven and damped resonator in a linear regime can be given by:

$$\ddot{z} + \Gamma\dot{z} + {\omega_0}^2 z = \frac{\tilde{F}}{m}, \tag{3.10}$$

where $z$ is the displacement, $\Gamma$ the damping rate, $\omega_0$=$2\pi f_0$ the eigenfrequency (without damping), and $\tilde{F}$=$F_d\cdot\cos(\omega_d t)$ the drive at the frequency $\omega_d$. The complex form of the formula can be written as:

$$\ddot{z} + \Gamma\dot{z} + {\omega_0}^2 z = \frac{F_d}{m}exp(i\omega_d t) \tag{3.11}$$

Solving the equation with Ansatz $z(t)=z_0 e^{i\omega_d t}$ gives the amplitude response $A$[115],

$$A(\omega_d) = |z_0| = \frac{F_d}{m\sqrt{({\omega_0}^2 - {\omega_d}^2)^2 + \Gamma^2 {\omega_d}^2}} \tag{3.12}$$

of the driven resonator. The amplitude response corresponds to the square root of the Lorentzian function. The sharper the resonance curve, the smaller the damping $\Gamma$ and, hence, the higher the quality factor. We will use this figure of merit to compare the quality of our resonators in later discussions. The quality factor is defined as the ratio of stored energy $W$ to the dissipated energy $\Delta W$ during one oscillation cycle[115]:

$$Q = 2\pi \frac{W}{\Delta W} = \frac{\omega_0}{\Gamma}\sqrt{1 - \frac{\Gamma^2}{2{\omega_0}^2}}. \tag{3.13}$$

For high-Q resonators $\frac{\Gamma^2}{2{\omega_0}^2}$ << 1 and then equation 3.13 reduces to,

$$Q \approx \frac{\omega_0}{\Gamma} = \frac{\omega_0}{\Delta\omega}, \tag{3.14}$$

where $\Delta\omega$ is the full width at half maximum of the Lorentzian fit. The derivation is omitted at this point and can be found in References [115, 117] or any mechanics book.

### 3.4.2 Dissipation Dilution

Nanomechanical systems under stress result in higher quality factors ($Q$) than equivalent unstressed systems. Such an enhancement in $Q$ or reduction in dissipation originates from a stress-induced damping dilution and is explained as follows[118,119].

$Q$ is the ratio of stored energy to the energy lost over one oscillation cycle. In the case of a cantilever, the energy is stored and lost by its bending. However, strings can additionally store and dissipate energy during lateral elongation. Also, as the vibrational deflection has to work against the high lateral tensile stress, more potential energy is built up in stressed strings and membranes. Therefore, the quality factor can be calculated by:

$$Q = 2\pi \frac{W_{\text{tension}} + W_{\text{elongation}} + W_{\text{bending}}}{\Delta W_{\text{elongation}} + \Delta W_{\text{bending}}}, \tag{3.15}$$

where $W_{\text{tension}}$ is the stored elastic energy required to deflect the string against the tensile force. $\Delta W_{\text{elongation}}$ and $\Delta W_{\text{bending}}$, and $W_{\text{elongation}}$ and $W_{\text{bending}}$ are the lost and stored energy due to elongation and bending, respectively.

If the tensile pre-stress in the string is dominating and assuming intrinsic damping due to elongation and bending to be equal, equation 3.15 becomes

$$Q \approx \alpha_{\text{dd}} \cdot Q_{\text{intrinsic}} \tag{3.16}$$

with the damping dilution factor

$$\alpha_{\text{dd}} = \left[ \frac{W_{\text{bending}}}{W_{\text{tension}}} + \frac{W_{\text{elongation}}}{W_{\text{tension}}} \right]^{-1}. \tag{3.17}$$

As $W_{\text{tensile}}$ is larger than the energies stored in elongation and bending, $\alpha_{\text{dd}}$ becomes larger than unity. That means the potential energy from the tensile stress dilutes the intrinsic losses and enhances $Q$[115].

The intrinsic quality factor of a stressed string resonator from the dissipation dilution model given by Yu and coauthors as[90,119,120]

$$Q_{\text{intrinsic},\,\sigma} = Q_{\text{intrinsic}} \left( \underbrace{2\lambda}_{\text{clamping}} + \underbrace{n^2\pi^2\lambda^2}_{\text{antinode}} \right)^{-1} \text{ with } \lambda = \frac{h}{L}\sqrt{\frac{E}{12\sigma}}, \tag{3.18}$$

where $n$ is the mode number, $h$ is the thickness, $l$ is the length, and $\sigma$ is the tensile stress. The higher the stress, the lower the $\lambda$ and the higher the multiplying factor to the $Q_{\text{intrinsic}}$, which enhances the quality factor. The clamping term comes from the curvature of the string close to the clamping points or pads, and the antinode term originates from the bending at the antinodes[120]. For a detailed discussion, readers can refer to the 'Fundamentals of Nanomechanical Resonators' by Silvan Schmid[115].

### 3.4.3 Young's Modulus

Young's modulus of a material is the ratio of tensile stress to tensile strain, denoted by E. Young's modulus determines the stiffness under uniaxial loading, often called elastic modulus. It is an important material parameter where the mechanical properties are of interest, such as in the fields of nano- and microelectromechanical systems[121], cavity optomechanics[58], nanophononics[122] and solid-state-based spin mechanics[57]. The performance of such systems and devices directly or indirectly depends on Young's modulus. Young's modulus affects the resonator's response regarding resonant frequencies and quality factors. At the nanoscale, types of bonds between the atoms, crystallographic orientation, types of defects and their distribution, and the material's stress impact the Young's modulus. Therefore, it is vital to understand how it is measured reliably.

In the linear regime following Hooke's law, stress is proportional to strain[117],

$$\begin{aligned} \sigma &= C \cdot \epsilon, \\ \epsilon &= S \cdot \sigma, \end{aligned} \tag{3.19}$$

where $C$ and $S$ are compliance and stiffness tensors, respectively. For anisotropic materials like silicon carbide, $C$ and $S$ are fourth-order tensors ($3^4$=81 entries per tensor). Fortunately, with the cubic symmetry of 3C-SiC, the tensor reduces to a 6×6 matrix with 3 independent variables, yielding[117],

$$\begin{pmatrix} \sigma_1 \\ \sigma_2 \\ \sigma_3 \\ \sigma_4 \\ \sigma_5 \\ \sigma_6 \end{pmatrix} = \begin{pmatrix} c_{11} & c_{12} & c_{12} & 0 & 0 & 0 \\ c_{12} & c_{11} & c_{12} & 0 & 0 & 0 \\ c_{11} & c_{12} & c_{11} & 0 & 0 & 0 \\ 0 & 0 & 0 & c_{44} & 0 & 0 \\ 0 & 0 & 0 & 0 & c_{44} & 0 \\ 0 & 0 & 0 & 0 & 0 & c_{44} \end{pmatrix} \begin{pmatrix} \epsilon_1 \\ \epsilon_2 \\ \epsilon_3 \\ \epsilon_4 \\ \epsilon_5 \\ \epsilon_6 \end{pmatrix} \tag{3.20}$$

for Equation 3.19, where $c_{ij}$ are the elastic stiffness coefficients. Following the Voigt notation, $\sigma_1$, $\sigma_2$, and $\sigma_3$ correspond to the normal stress in the crystal direction [100] (x-axis), [010] (y-axis), and [001] (z-axis), respectively. Moreover, $\sigma_4$, $\sigma_5$, and $\sigma_6$ represent shear stress components along y-z, x-z, and x-y directions, respectively. Young's modulus along the [110] (x-axis) can be calculated by inverting the stiffness matrix component $s_{11}$,

$$E_{[100]} = (s_{11})^{-1}. \tag{3.21}$$

As our SiC device layer has crystallographic orientation [111], the compliance matrix must be rotated to align the x-axis with the desired direction. The detailed discussion about the compliance matrix transformation can be found elsewhere[90] and omitted from this discussion. The elastic constants

$$c_{11} = 352\,\text{GPa}, c_{12} = 140\,\text{GPa}, c_{44} = 233\,\text{GPa}, \tag{3.22}$$

from a reference[123] fit previously calculated Young's modulus[124] of 400 GPa for samples used in this work.

The nanoindentation technique can estimate Young's modulus of a material. Literature also provides data about Young's modulus and other material properties[125–128]. However, Young's modulus of materials is known to vary from bulk depending on the wafer growth parameters and nanofabrication steps. Therefore, relying on the literature data or specifications from the manufacturer can lead to deviations. In this work, we use Euler-Bernoulli fitting to the measured data to deduce stress and Young's modulus.

### 3.4.4 Effect of Point Defects

Silicon carbide is one of the best candidates as a structural material for nuclear reactors owing to its high mechanical strength and rigidity, high thermal conductivity and thermal shock resistance, very low neutron-induced radioactivity, small neutron capture cross-section, and dimensional stability under neutron irradiation. Experiments have been performed by helium implantation to study ion-induced microstructural and compositional changes, the accumulation and recovery of irradiation damage, vacancy formation, and their effect on the evolution of defects[129–138]. However, most of the work has been done in high-damage regimes, where the interest of the nuclear research community lies.

In this work, our goal is to create ensembles of $V_{Si}$ in SiC nanoresonators using He implantation, where other types of point defects are also created, such as antisites and interstitials. Therefore, we will first understand the change in mechanical properties arising from various point defects, which are discussed below.

Research has been done to study the effect of ion implantation in the lower-energy and low-fluence, i.e., low-damage regime. Oliviero and coauthors characterised helium implantation-induced defects in 4H-SiC and 6H-SiC by thermal helium desorption spectrometry. Samples were implanted with helium at energies ranging from 100 eV to 3 keV with fluence ranging from $10^{13}$ $cm^{-2}$ to $10^{15}$ $cm^{-2}$ followed by annealing at 1800 K. Their work mainly focused on helium trapping and the effect of annealing. They have concluded that most of the helium remains trapped at room temperature[133].

Nogami and Hasegawa performed neutron irradiation and helium implantation experiments on CVD-grown SiC to study changes in hardness, elastic modulus, and fracture toughness at moderate damage (0.5 dpa) and high temperatures (800 °C) using indentation techniques. Helium implantation does not change the hardness drastically but reduces elastic modulus and fracture toughness[139]. Barbot and coauthors have investigated the evolution of hardness and elastic modulus after low-damage helium implantation on 4H-SiC using nanoindentation tests. They have found that both hardness and elastic modulus increase for low levels of damage (0.01-0.02 dpa)[140]. The studies mentioned above are presented on bulk samples and do not clearly state the effect of different types of point defects.

Xi and colleagues have investigated the effect of different point defects, including vacancies, antisites, and interstitials, on volumetric swelling and the elastic modulus of SiC using molecular dynamics simulations with Tersoff potential. To quantify the number of defects, defect concentration along with their upper and lower bounds are considered, which is the ratio of the number of defects to the

total number of atoms in the simulation box.

Xi and coauthors found that point defects do not create volumetric swelling but significantly impact Young's modulus. The influence of point defects on the change in Young's modulus is fitted by an exponential function given by:

$$\begin{aligned}\Delta E = &-656.582 C_{\mathrm{Y}}(V_{\mathrm{C}})^{0.782} - 2102.507 C_{\mathrm{Y}}(V_{\mathrm{Si}})^{0.956} \\ &-667.508 C_{\mathrm{Y}}(Si_{\mathrm{C}})^{0.542} + 2327.996 C_{\mathrm{Y}}(C_{\mathrm{Si}})^{1.504}\end{aligned} \tag{3.23}$$

where $C_{\mathrm{Y}}(V_{\mathrm{C}})$, $C_{\mathrm{Y}}(V_{\mathrm{Si}})$, $C_{\mathrm{Y}}(Si_{\mathrm{C}})$ and $C_{\mathrm{Y}}(C_{\mathrm{Si}})$ are the concentrations of $V_{\mathrm{C}}$, $V_{\mathrm{Si}}$, $Si_{\mathrm{C}}$ and $C_{\mathrm{Si}}$, respectively. The authors concluded that change in $E$ is a combination of effects from volumetric swelling, types and distribution of point defects, and vacancy clusters[141].

From the stopping and range of ions in matter (SRIM), it is possible to estimate the numbers $V_{\mathrm{Si}}$ and $V_{\mathrm{C}}$. However, it is difficult to argue about the antisites due to the possible creation of interstitials. Nevertheless, Xi's work helps us understand the effect of different point defects on volumetric swelling and Young's modulus[141]. Their results are used qualitatively to set the basis for interpreting our results after helium ion implantation on 3C-SiC nanomechanical resonators.

In conclusion, I have briefly introduced quantum technologies, focusing on communication and sensing. Then, I introduced different types of point defects, with a special focus on point defects and their properties. Afterwards, I set up the theoretical foundation required for the two projects discussed in this thesis, which is divided into three parts: G-centres in silicon, silicon vacancies in silicon carbide, and nanomechanics. Now, I shall move to one of the crucial parts of this work where I contributed the most: the fabrication of nanostructures.

# Chapter 4

# Experimental Techniques

This Chapter describes experimental techniques used for the fabrication and characterisation of nanostructures. The major part of my doctoral research is invested in developing etching techniques for silicon and silicon carbide.

The top-down fabrication steps of pillars in silicon are reported. Afterwards, metal-assisted chemical etching (MACEtch) to etch silicon anisotropically is presented in detail. Applications of MACEtch, its working mechanism, and a brief comparison with other etching techniques are presented. Finally, experimental proof of RIE-induced damage, which sets up the motivation of MACEtch, is demonstrated.

Next, protocols to fabricate doubly clamped resonators in 3C-SiC and 4H-SiC are described. In addition, photoelectrochemical etching (PEC) for fabricating free-standing resonators in 4H-SiC is discussed. The need to develop and use PEC etching with the experimental setup is stated. Lastly, We will discuss the Fabry-Pérot interferometry for characterising strings and helium ion implantation to create $V_{Si}$ in SiC.

## 4.1 Nanopillars in Silicon

### 4.1.1 Fabrication Protocol

Silicon nanopillars are fabricated via a top-down approach using electron beam lithography (EBL) and metal-assisted chemical etching (MACEtch). In order to investigate the influence of nanopillar size, arrays of nanopillars with varying diameters are fabricated. The height of the pillars is controlled by the etch

time during MACEtch. Fabrication steps are performed in the nanofabrication facilities and cleanroom of the Ion Beam Center of Helmholtz-Zentrum Dresden - Rossendorf (HZDR).

We use <100> oriented silicon wafer with 525 µm nominal thickness grown by a float zone technique with carbon and oxygen impurities about $5 \times 10^{14}\,\mathrm{cm}^{-3}$ and $1 \times 10^{14}\,\mathrm{cm}^{-3}$, respectively. The wafer is cleaved into 5 mm × 5 mm pieces due to the technical requirements of the measurement setup.

Figure 4.1 illustrates steps to fabricate silicon nanopillars. To remove the organic and carbon residues, the samples are cleaned with the piranha solution (3 parts sulphuric acid and 1 part hydrogen peroxide) for 15 min. Without piranha cleaning, the metal film lifts off during MACEtch due to poor adhesion. The native silicon oxide is removed by dipping the samples in a 0.5 % hydrogen fluoride (HF) solution for 2 min. Next, a negative-tone electron-beam resist (ma-N 2410, 3500 rpm, 45 s) is spin-coated, followed by a hot plate bake at 90 °C for 150 s.

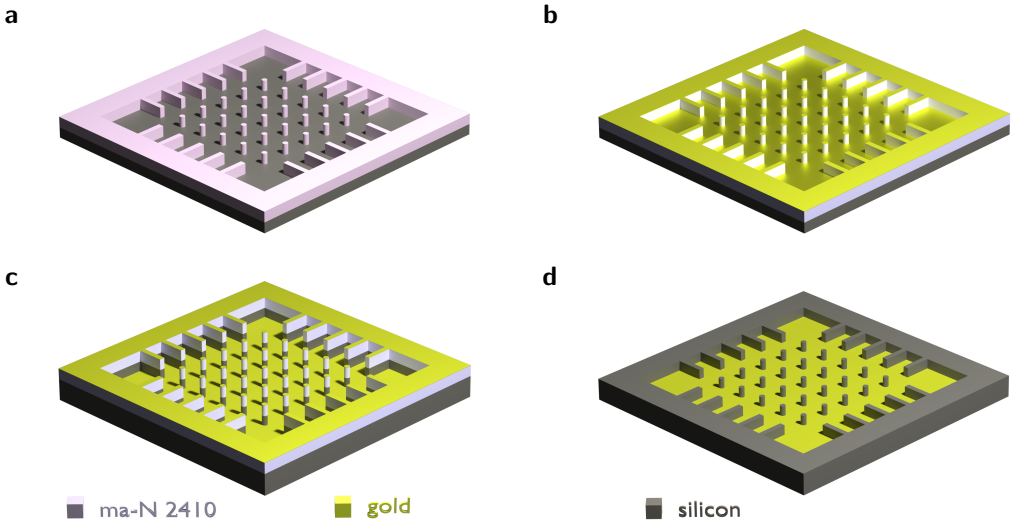


**Fig. 4.1: Schematic of fabrication steps for silicon nanopillars.** (a) Patterns with arrays of pillars of varying diameters are defined by EBL and arrays of photoresist nanopillars are created after development. (b) 10 nm Au is evaporated, which will serve as a catalyst during MACEtch. (c) MACEtch etches silicon anisotropically, and nanopillars are fabricated. (d) The resist and Au film on top are lifted off. However, the Au film in contact with the silicon remains intact.

The EBL pattern consists of 2D nanopillar arrays of ⌀300 nm to ⌀1100 nm. The EBL design will be discussed in more detail later (Section 5.1). For pattern transfer, we use the Raith 150TWO tool with 20 kV acceleration voltage and 20 µm aperture. The samples are developed in ma-D 525 developer for 210 s followed

by isopropyl alcohol (IPA) dip to stop the development process and nitrogen blow dry. Gold (Au) is used as a catalyst for all the MACEtch experiments. After the native oxide removal step with a 0.5 % HF solution, 10 nm Au is evaporated at a rate of 3 Å $s^{-1}$. Removing native oxide is necessary; otherwise, HF in the MACEtch solution etches the silicon oxide, and MACEtch stops due to metal film peel-off.

All MACEtch experiments were performed in the cleanroom at room temperature without stirring. The MACEtch solution is prepared by adding 4.5 mL 31% hydrogen peroxide ($H_2O_2$) in 100 mL de-ionised (DI) water and then adding 25 mL 40% hydrogen fluoride (HF). 5 min waiting is kept in between both steps. The samples are dipped in the solution for 5 min to achieve an etch depth of 1200 nm. The etch rate is determined by previously performed calibration experiments (Section 5.1.2). To remove the solution from the sample surface and stop etching, samples are dipped in two consecutive DI water baths and dried using a nitrogen blow. The photoresist is removed by ultrasonication in acetone for 30 s. The sample is cleaned with an IPA dip and dried with a nitrogen blow. As HF etches silicon slowly and can deteriorate the surface finish, MACEtch is performed without removing the photoresist from the pillar top. The details of the fabrication protocols in a table form can also be found in Appendix A.

### 4.1.2 Metal-Assisted Chemical Etching

The preliminary work similar to MACEtch is attributed to Dimova-Malinovska's work to prepare thin porous silicon layers[142]. Li and Bohn put forth the first demonstration of MACEtch in 2000[143]. They fabricated light-emitting porous silicon by depositing thin metal layers and immersing it in the solution of hydrogen fluoride (HF) and hydrogen peroxide ($H_2O_2$). Since then, MACEtch has been used to fabricate nanostructures in silicon (also germanium, gallium arsenide, and silicon carbide) due to several advantages over standard wet and dry etching techniques: the possibility of fabricating high aspect ratio structures[144–146], its versatility[147,148] and high precision[146], possibility of etching along specific directions[147,149], ability to create lattice-damage free structures[40,144,149], low-cost. MACEtch has applications for optoelectronics[150,151] and MEMS devices[152], photovoltaics[144,153], X-ray optics[146,154–156], fabrication of nanowires[157–160], 3D nanostructures[161–163] and photonic nanostructures[40].

#### 4.1.2.1 Mechanism

MACEtch is a fabrication technique where silicon with metal (acts as a catalyst) deposited on it when immersed in a solution containing an etchant (HF), and

an oxidiser ($H_2O_2$) etches preferentially at the metal/Si interface. The solution with silicon can be treated as an electrochemical cell. $H_2O_2$ is reduced at the metal surface due to its catalytic activity and gives holes. The holes diffuse through the metal and are injected into the valence band of silicon. The holes oxidise the silicon to silicon oxide, and HF dissolves the formed silicon oxide. The concentration of holes is highest at the metal/Si interface. Hence, silicon beneath the metal is etched much faster than silicon without metal coverage. The well-accepted essential chemical reactions are as follows[146]:

$$\begin{aligned} H_2O_2 + 2H^+ &\rightarrow 2H_2O + 2h^+, \\ Si + 4h^+ + 6HF &\rightarrow {SiF_6}^{2-} + 6H^+ \end{aligned} \tag{4.1}$$

The complex dynamic technique combines multiple processes and depends on various experimental parameters discussed below. The etch quality, etch rate, uniformity, and porosity of the structures depend on various factors: pathways available for the transfer of reactants and byproducts, thickness and morphology of the metal film, crystal orientation and resistivity of the substrate, concentration ratio of etchants, temperature, dimensions, and lateral spacing between the structures. The following section will discuss some of the most critical parameters relevant to our experiments. More details can be found elsewhere[147,149,154].

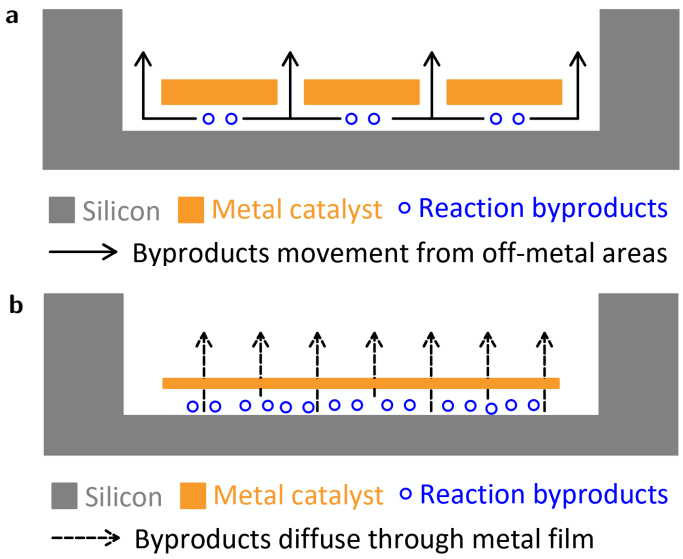


**Fig. 4.2: A scheme of two mass transfer pathways during MACEtch.**
(a) Model I: The reactants and reaction byproducts flow around the periphery of the structure. Model I dominates in the case of densely packed nanostructures or sparse microstructures. (b) Model II: The reactants and reaction byproducts diffuse through the thin metal film. Model II dominates in the case of sparse nanostructures and thin metal film.

The mass transfer of the reactants and reaction by-products has two pathways. It can be understood by the models shown in Figure 4.2: either around the metal (Figure 4.2a) or through thin metal film by diffusion (Figure 4.2b). Which of the two dominates depends on the thickness and morphology of the metal film, the lateral size and spacing between the structures, and the balance between the formation and removal rate of reaction by-products. In reality, the mass transfer combines both models and will be explained in Chapter 5.

Generally, the concentration ratio of the etchants and the substrate orientation determine the anisotropic nature of the etching. How easily oxidised silicon atoms are removed depends on the strength of their back bonds, and it is in the order (100)<(110)<(111). Therefore, the atoms on the 100 plane are readily etched, and the etching preferentially proceeds along <100> directions. The oxidation of silicon is kinetically favoured along non-<100> directions where the density of back bonds is higher[146,157]. Similarly, with a high HF concentration, the oxidised silicon is readily removed from non-<100> directions with more back bonds. Notably, the MACEtch mechanism is very complex, and etching depends on the concentration of etchants and the metal catalyst. More details about the mechanism of MACEtch can be found elsewhere[146,147,157].

#### 4.1.2.2 Dry Etch, Wet Etch and MACEtch

In semiconductor fabrication, etching is an essential step in creating 3D structures. Dry etching techniques such as reactive ion etching (RIE) are commonly used where reactive ions remove the material isotropically or anisotropically, depending on the combination of gases and experimental conditions. Direct write methods such as focused ion beam-induced deposition (FIBID) and electron beam-induced deposition (EBID) can make 3D nanostructures with low throughput. Both methods have one common disadvantage: lattice damage due to ions. Lattice damage can create unwanted optically active defects and is undesirable for photonics.

Wet etching techniques remove material layer by layer and solve the problem of unwanted crystal damage. However, etching proceeds preferentially along specific crystal directions. MACEtch, on the other hand, provides control over etching directions. Table 4.1 presents the comparison between standard dry etching, wet etching, and MACEtch.

RIE is the industry standard and is extensively used for high-volume production compared to MACEtch. However, it has been investigated and further researched, as well as for other materials. MACEtch has the potential to be considered a standard wafer-scale fabrication technique both in research and in industries due

to its ability to fabricate lattice damage-free high aspect-ratio structures at low cost, especially in fields such as photonics, photovoltaics, and MEMS sensors.

**Table 4.1: Characteristics of wet etch, dry etch and MACEtch**[144]

| | Dry Etch | Wet Etch | MACEtch |
|---|---|---|---|
| Directionality | Anisotropic | Isotropic | **Anisotropic** |
| Aspect ratio | Medium | Low | High |
| Ion induced damage | Mild to severe | None | **None** |
| Orientation dependence | Weak | Strong | Controllable |
| Etch rate | Slow/medium | Fast | Fast |
| Sidewall smoothness | Smooth/rough | Smooth | Smooth/rough |
| Cost | High | Low | Low |

#### 4.1.2.3 RIE-Induced Lattice Damage

Reactive ion etching (RIE) is the standard technique in the industry and research to fabricate high-aspect ratio structures with high fidelity and throughput. RIE uses high-energy ions and radicals that remove materials by physical sputtering and chemical reactions. However, the ion bombardment during the process causes lattice damage and can lead to radiation-induced luminescence centres, which are well-studied from the late 80'[74]. The type of defects formed depends on the conditions of plasma, RIE gases, and residual impurities in the sample.

The typical gases used in RIE are carbon tetrafluoride ($CF_4$), octafluorocyclobutane ($C_4F_8$), sulphur hexafluoride ($SF_6$), and oxygen ($O_2$). Plasma in combination with these gases and impurities in silicon wafer can result in W (1018 meV), X (1040 meV), T (935 meV), I (965 meV), G (967 meV), C (790 meV) and P (767 meV) lines[164–166]. As the ions are bombarded everywhere, unwanted optically active centres cane be created all over the sample without any control.

Although annealing protocols can remove irradiation-induced damage and unwanted colour centres, they can introduce other photoluminescence (PL) lines. For instance, it was reported that G and C lines introduced by RIE anneal out at 400 °C. However weak PL lines at 1008 meV and 997 meV were observed after annealing at 400 °C[165]. Buyanova and others have reported the formation of C and G lines with an RIE recipe including $SF_6$ and $O_2$, avoiding carbon-related gases ($CF_4$, $C_4F_8$). If only $SF_6$ is used, sharp C lines and weak G lines are observed[166]. For photonic devices, annealing above 900 °C causes intermixing between Si and $SiO_2$ in the case of SOI with high-quality BOX (buried oxide). Annealing can

lead to solid-state dewetting, which affects the shape stability of small devices on an SOI substrate and, therefore, is not suitable for nanostructures[68].

To investigate the effect of RIE on a silicon-on-insulator (SOI) sample, we fabricate a square frame using RIE. The wafer is a commercial SOI from IceMOS Technology with a residual carbon concentration of $10^{16}$ $cm^{-3}$. The RIE recipe employs $C_4F_8$, $SF_6$, and $O_2$ gases. Figure 4.3 shows the results of a 2D photoluminescence (PL) scan. G-centres are formed across the sample without any control, which is undesirable for photonics.

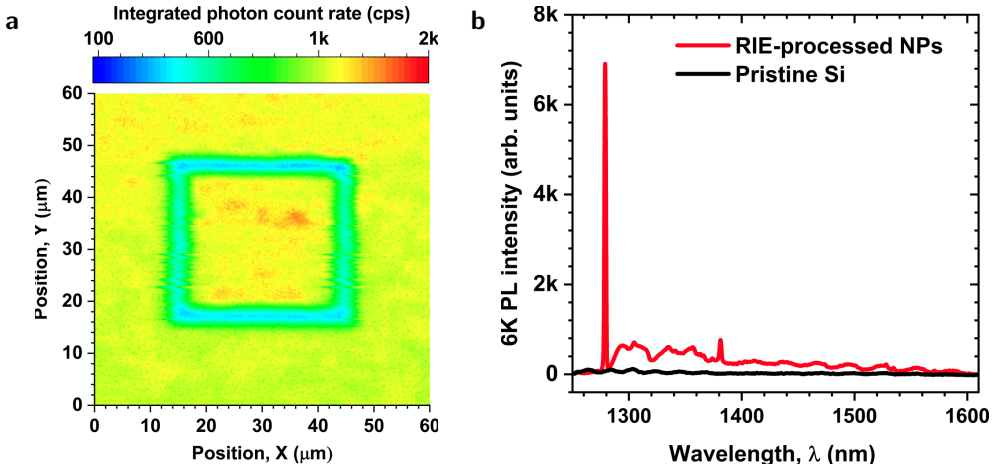


**Fig. 4.3: Low-temperature photoluminescence spectroscopy.** (a) A 2D PL scan of a frame structure fabricated using RIE shows the formation of unwanted optically active defect centres. (b) The PL spectrum shows that ZPL is at 1278 nm, which is the optical fingerprint of the G-centre.

To make the fabrication protocol crystal defect-free and use-for-all regardless of impurities present in the sample, we decided to implement an emerging wet etching method: MACEtch.

## 4.2 Mechanical Nanoresonators in Silicon Carbide

This project is carried out in collaboration with Prof. Eva Weig's group from the Technical University of Munich. We have fabricated doubly clamped resonators or strings in 3C-SiC. In the top-down approach, we used standard nanofabrication techniques: EBL and inductively coupled plasma-reactive ion etching (ICP-RIE). A unique dopant-selective photoelectrochemical etching was employed for fabricating resonators in 4H-SiC, along with standard EBL and ICP-RIE.

### 4.2.1 Fabrication Protocol

#### 4.2.1.1 3C-SiC Nanoresonators

3C-SiC mechanical nanoresonators are fabricated in collaboration with Prof. Eva Weig's group from the Technical University of Munich. EBL and metal deposition are performed in nanofabrication facilities at HZDR. All other process steps are carried out at the Technical University of Munich by Felix David.

Mechanical resonators in cubic silicon carbide (3C-SiC) have been fabricated using a top-down approach. 110 nm <111> oriented 3C-SiC is epitaxially grown on 1 mm <111> silicon by NovaSiC. The wafer is cleaved into 5 mm × 5 mm pieces before processing. The material is crystalline, and the properties of the resonators depend on the relative orientation of the sample. Therefore, our wafers are marked with a flat to the [1 2 $\bar{2}$] direction. The 5 mm × 5 mm pieces are marked by scratching the bottom and left sides with a diamond tip. A unique identification number is written on the backside of the samples before processing. Figures 4.4 and 4.5 show EBL design and fabrication steps, respectively.

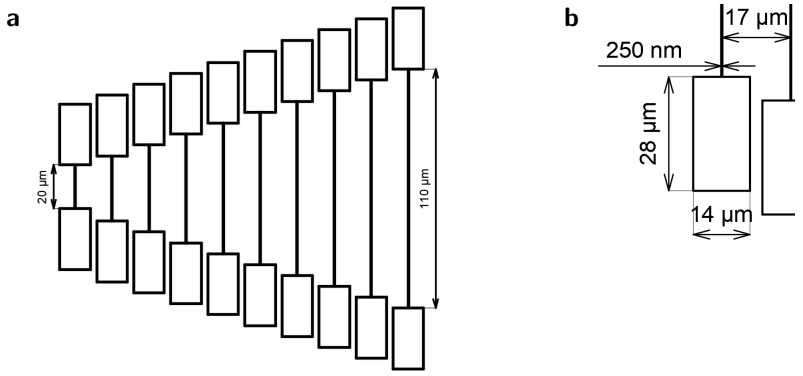


**Fig. 4.4: EBL design of a harp of SiC resonators.** (a) Array of resonators varying in length from 20 µm to 110 µm. (b) Close view showing the dimensions of the pads, resonator width, and spacing between the resonators.

First, samples are cleaned with acetone and IPA. 450 nm 950K PMMA A6 is spin coated, followed by a hot plate bake of 180 °C for 90 s. From the tests, we find the optimum dose for the pads and strings 130 µC cm$^{-2}$ and 220 µC cm$^{-2}$, respectively. We use the Raith 150TWO tool for pattern transfer with 10 kV acceleration voltage and 30 µm aperture. The sample is developed in MIBK:IPA (1:3) for 50 s followed by IPA dip to stop the development process and dried using nitrogen. Next, we deposit 30 nm chromium as an RIE mask by thermal evaporation at ∼1.5 Å s$^{-1}$.

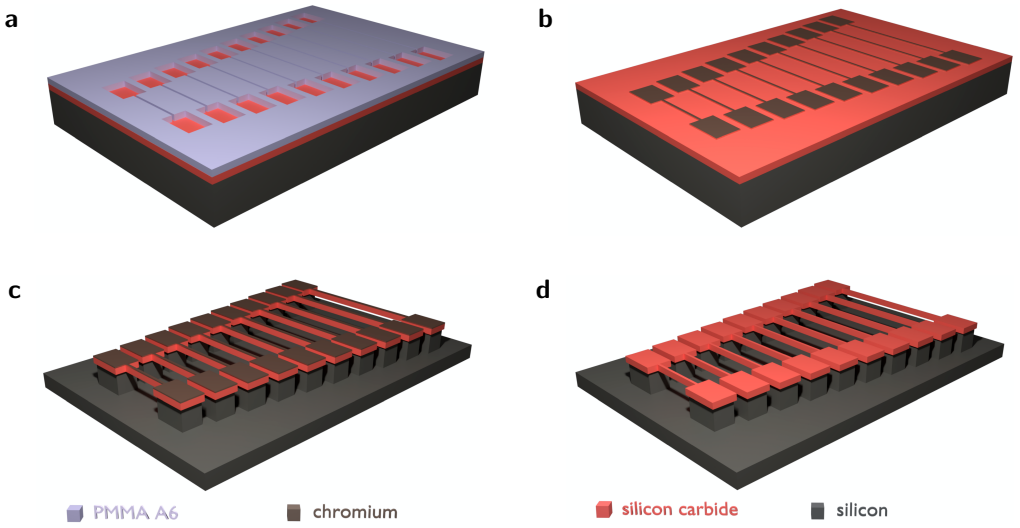


**Fig. 4.5: Schematic of fabrication steps for 3C-SiC resonators.** (a) The pattern for mechanical resonators is defined by EBL. (b) 30 nm Cr is evaporated as an etch mask for ICP-RIE. (c) In the three-step ICP-RIE process, first silicon carbide and silicon are etched anisotropically. Then, silicon is etched isotropically to underetch silicon carbide. In the last step, an Ar mill is used to restore the etch rate of Cr during subsequent chemical etching. (d) The Cr mask is removed by chromium etchant, and free-standing resonators are fabricated.

Afterwards, the resist is lifted off using ultrasonication at low power, followed by an IPA dip and a nitrogen blow-dry. Resonators are released by using three-step RIE, where first SiC and Si are etched anisotropically, followed by isotropic etching of Si. In the following step, the Cr mask is modified using an argon mill to restore its etch rate in the Cr etchant. For a detailed explanation of the RIE process, readers can refer to Dr. Yannick Klaß's PhD thesis[90]. Finally, we characterise the resonators using Fabry-Pérot Interferometry.

#### 4.2.1.2 4H-SiC Nanoresonators

The top-down fabrication of 4H-SiC mechanical nanoresonators is described in this section. All the experimental steps are performed in the nanofabrication facilities and cleanroom of the Ion Beam Center of HZDR by me.

Figure 4.6 presents fabrication steps. We have purchased the bilayer 4H-SiC wafer from Norstel AB. The 500 nm n-type layer is grown on the 300 µm substrate layer, and both contain $1 \times 10^{18}\,\mathrm{cm}^{-3}$ nitrogen. Next, 250 nm p-type device layer with $1 \times 10^{17}\,\mathrm{cm}^{-3}$ aluminium doping is grown on top. Before processing, the wafer is diced into 5 mm $\times$ 5 mm pieces.

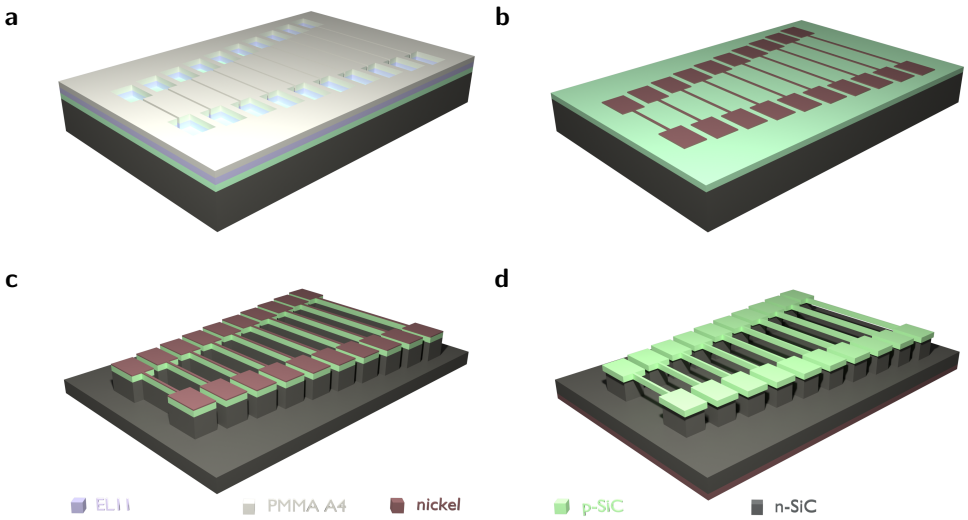


**Fig. 4.6: Schematic of fabrication steps for 4H-SiC resonators.** (a) The pattern for mechanical resonators is defined by EBL. (b) 50 nm Ni is evaporated as an etch mask for ICP-RIE. (c) In the ICP-RIE process, first silicon carbide and silicon are etched anisotropically. (d) Then, the Ni etch mask is dissolved using aqua regia. Again, 100 nm Ni is deposited on the back side, which serves as an electrical contact for photoelectrochemical (PEC) etching. PEC etching provides dopant selectivity and etches only n-SiC, releasing resonators of p-SiC.

First, samples are cleaned with acetone and IPA. 270 nm EL11 and 125 nm 950K PMMA A4 were spin coated. Samples are baked using a hot plate at 150 °C for 5 min before and after both the resist spinning steps. We use the Raith 150TWO tool for pattern transfer with 10 kV acceleration voltage and 30 µm aperture. The sample is developed in MIBK:IPA (1:3) for 30 s followed by a 90 s IPA dip to stop the development process and dried using nitrogen.

Next, we deposit 50 nm nickel RIE mask by thermal evaporation at $\sim$3 Å s$^{-1}$. The resist is lifted off using ultrasonication at low power, followed by an IPA dip and a nitrogen blow-dry. RIE is used to etch the material anisotropically with a fluorine-based recipe that includes $SF_6$=40 SCCM, $O_2$=10 SCCM, pressure=2.0 Pa, ICP Power=400 W, and RF Power=75 W, giving an etch rate of $\sim$350 nm min$^{-1}$.

Afterwards, we dissolve the Ni mask by aqua regia, which is a mixture of nitric and hydrochloric acid [1 part of $HNO_3$: 3 parts of HCl]. The solution is heated to 80 °C. Later, samples are cleaned by DI water dip and nitrogen blow drying. In the last step, photoelectrochemical dopant-selective etching (PEC) is employed to remove n-SiC, releasing free-standing resonators of p-SiC. It requires a nickel back contact, as the samples themselves serve as a working electrode. Therefore, 100 nm Ni is evaporated by thermal evaporation on the back side of the samples.

Finally, PEC etching is employed to etch the n-SiC layer, and resonators of p-SiC are released. Details about the PEC setup and the PEC cell configuration are mentioned later (Section 4.2.2). The cell is then flushed with DI water, and the sample is blow-dried using a nitrogen gun. The details of the fabrication protocols in a table form can also be found in Appendix A.

### 4.2.2 Photoelectrochemical Etching

Silicon carbide (SiC) is a wide-bandgap semiconductor with a high breakdown field, mechanical strength, corrosion resistance, and chemical resistance. Therefore, it becomes difficult to micromachine or etch SiC for semiconductor applications. The chemical stability of SiC is due to its strong covalent bonds resulting from the wide bandgap and a valence band edge at low energy. Nevertheless, for microelectronics applications, dry etching techniques are standard[167–172].

On the other hand, photoelectrochemical etching (PEC) gained importance for III-V semiconductor electronic and photonic device processing in the 1990s. Kohl and Ostermayer from AT&T Bell Laboratories introduced PEC, including its applications for GaAs, in 1989[173]. Meanwhile, Shor and coworkers published articles focusing on the dopant-selective etch feature of PEC for 6H-SiC and 3C-SiC[168,174,175]. Later in 2000, they patented the method to etch SiC selectively based on different conductivity[176] selectively. Since then, PEC etching of SiC has been used in the research community for making porous structures[177,178], characterising crystal polarity, polytype, defect density, and distribution[179,180], micro-electro-mechanical systems (MEMS) devices[92,171,181], and optomechanical devices like microdisk resonators[182].

#### 4.2.2.1 Bi-layer 4H-SiC

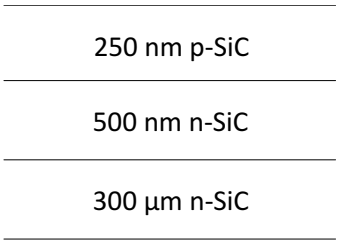


**Fig. 4.7: Bilayer 4H-SiC**

Hybrid spin-mechanical systems in 4H-SiC consist of silicon vacancies ($V_{Si}$) created in mechanical systems such as resonators or membranes. As point defects like $V_{Si}$ are susceptible to the environment, the crystalline quality is crucial. High-crystalline quality 4H-SiC can only be grown on 4H-SiC. Therefore, we use epitaxially grown 4H-SiC bilayer samples (Figure 4.7) to experimentally realise spin-mechanical magnetometry.

Etch selectivity is essential to underetch the structures and fabricate free-standing mechanical resonators. Usually, the selectivity originates from both layers being of different materials, such as SiC on Si, $Si_3N_4$ on $Si/SiO_2$. In our case, the selectivity based on conductivity is achieved by doping the material with nitrogen and aluminium during the epitaxial growth process. Alternatively, dopant-selectivity can be created by ion implantation techniques. As mentioned in the previous subsection, it is difficult to etch SiC using standard wet or chemical etching techniques for Si and GaAs. Also, none of them offer dopant-selective etching. The only etching technique that allows us to achieve either n-SiC or p-SiC is photoelectrochemical etching (PEC), explained in the next section.

#### 4.2.2.2 Mechanism

Photoelectrochemical etching involves using the above bandgap light to enhance the oxidation of the semiconductor in contact with an electrolyte and the removal of the oxide by the electrolyte. Acidic (HF) and basic (KOH) solutions have been used as electrolytes. The chemical reaction occurring at the semiconductor-electrolyte (SiC/KOH) interface is as follows:

$$SiC + 6h^+ + 8OH^- \rightarrow [Si(OH)_2O_2]^{2-} + CO + 3H_2O \tag{4.2}$$

Other insoluble products such as $SiO_2$ and gases ($CO_2$, CO) in the form of bubbles are also formed. UV light with energy higher than the bandgap ($E_{g(4H\text{-}SiC)}$=3.23 eV$\hat{=}$ 384 nm) is used to illuminate the sample, which produces electron-hole pairs that migrate to the semiconductor/electrolyte interface under an applied bias. Holes at the interface are equivalent to broken bonds, and hole transfer to the electrolyte oxidises the semiconductor surface. Oxides formed are removed by dissolution or gas evolution[183].

Figure 4.8 shows the band diagram of the semiconductor/electrolyte interface for both n-SiC and p-SiC. A Schottky barrier is formed at the SiC/KOH interface and a depletion region in SiC. Suppose the Fermi level of the semiconductor at the semiconductor/electrolyte interface is within the bandgap. In that case, the semiconductor's charge carriers' density is less than the ions in the electrolyte. As a result, the majority of potential drops in the semiconductor. The applied voltage bends bands for p-SiC and n-SiC to promote hole transfer. The flat-band voltage of p-SiC is higher than n-SiC. Therefore, a negative bias applied at the cathode can be selected above the flat-band voltage of n-SiC but below the flat-band voltage of p-SiC. This negative bias ensures more upward band bending in n-SiC without getting closer to flat-band voltage for p-SiC, meaning p-SiC will not be etched in this configuration.

Figure 4.8a shows energy band diagrams in thermal equilibrium with Schottky barriers $\phi_{i(n)}$ and $\phi_{i(p)}$. The change in barrier across the semiconductor:

$$\Delta\phi = \phi_{\mathrm{i(p)}} - \phi_{\mathrm{p}} = \phi_{\mathrm{i(n)}} - \phi_{\mathrm{n}}, \tag{4.3}$$

where $\phi_{\mathrm{p}}$ and $\phi_{\mathrm{n}}$ are the Schottky barriers after applying a negative bias. For n-SiC, more upward band bending supports hole movement, which results in etching n-SiC. The barrier at the p-SiC/KOH interface is large enough to collect only a few holes at the surface, and the material is not etched. This mechanism can also be used for the samples with n-SiC at the top of p-SiC, and p-SiC can act as an etch stop layer[64].

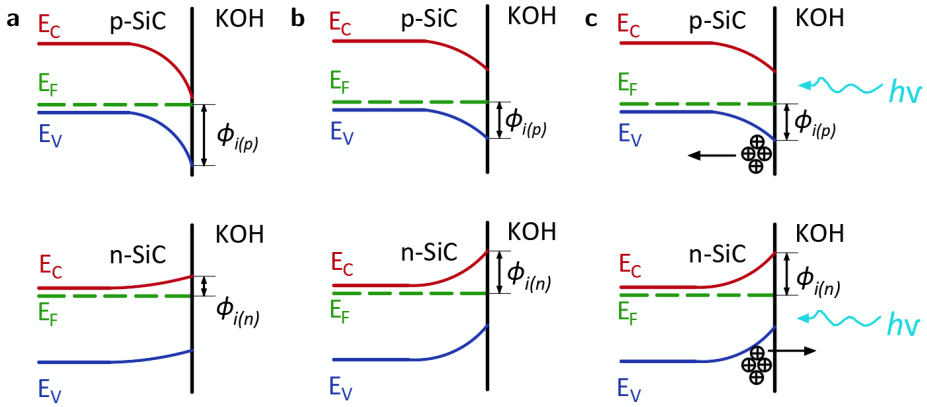


**Fig. 4.8: Energy band diagrams of the n-SiC and p-SiC/KOH interface.**
(a) Thermal equilibrium: SiC in contact with KOH forms a Schottky barrier at the interface ($\phi_{\mathrm{i(n)}}$ and $\phi_{\mathrm{i(p)}}$) and depletion region in SiC. (b) Bias: Under a negative bias on the KOH side (Pt electrode dipped in KOH), bend bands for both n-SiC and p-SiC. (c) UV illumination: Above bandgap UV light produces electron-hole pairs, and holes migrate to the interface, resulting in oxidation and dissolution of the n-SiC. Holes collected at the p-SiC/KOH interface are negligible due to the larger energy barrier $\phi_{\mathrm{(p)}}$, so the etching of p-SiC is effectively suppressed.

The rate and quality of etched structures depend on several factors, including the type and concentration of the electrolyte, applied bias, light intensity, doping type and density, crystal quality, orientation, and temperature. PEC etching with wafer scalability and capability to produce defect-free structures having low total thickness variation (TTV) and low surface roughness ($\sim$1 nm RMS), dopant selectivity ($\geq$ 20:1), and faster etch rates ($>$ 4 µm h$^{-1}$) holds great promise for next-generation MEMS and quantum applications[183].

#### 4.2.2.3 Experimental Setup

Figure 4.9 shows the schematic of the PEC setup and photograph. The PEC setup, including the photoelectrochemical cell (PECC) and potentiostat, is bought from Zahner-Elektrik GmbH & Co. KG. The UV light source used is a LED LS365-2 with a typical intensity of 2000 $\mathrm{W\,m^{-2}}$ and a wavelength of 365 nm ($\hat{=}$ 3.4 eV), which is above the bandgap energy of 4H-SiC. A plano-convex lens is mounted directly after the LED to get a parallel beam (⌀4 cm).

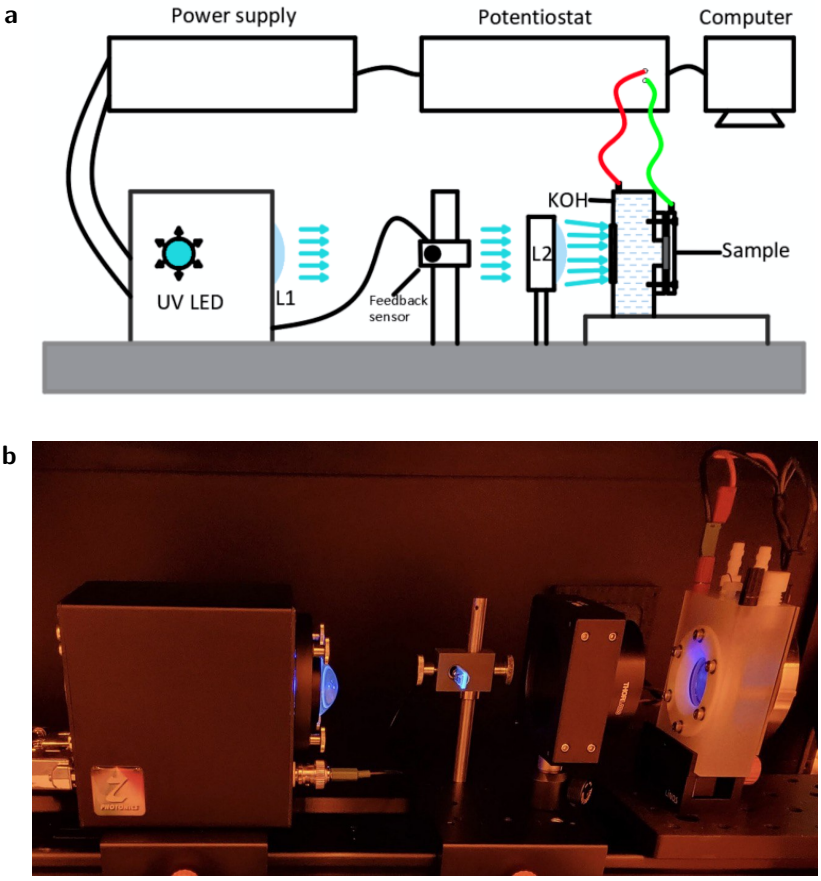


**Fig. 4.9: PEC etching setup.** (a) Schematic showing key components and general arrangement of the setup. (b) Photograph of the setup while in operation showing the UV LED, feedback sensor, lens to focus light, and PEC cell.

We use PECC in a two-electrode configuration: SiC sample with Ni back contact and platinum coil immersed in the electrolyte serve as a working and counter electrode, respectively. PECC has an optical window with a ⌀30 mm to illuminate the sample, and the sample is mounted on the other side. The electrical contact with the sample is made using the conductive foam and the copper tape. PECC

has provisions for an inlet and outlet for electrolyte circulation (not employed in our experiments) and cell cleaning.

To increase the light intensity by focusing on a small spot ($\sim \varnothing 10$ mm), a plano-convex lens (Thorlabs LA1401-A-ML) is mounted in between the UV LED and the PECC. The active area of the 5 mm $\times$ 5 mm sample which is exposed to the electrolyte and light is $\sim \varnothing 3$ mm ($\approx 0.07065$ cm$^2$). A photodiode is fixed before the second lens, which gives feedback to the LED and ensures the set light intensity. Zahner provides the software for controlling the potentiostat and LED and data acquisition and analysis.

## 4.3 Fabry-Pérot Interferometry

A Fabry-Pérot laser interferometer setup facilitates stable and fast measurements of the mechanical response of resonators. It allows access to the vibrating resonator's frequency, quality factor, and amplitude. In addition, we deduce stress and Young's modulus by measuring higher modes. Figure 4.10 shows a schematic and photograph of the setup. The setup was developed at Helmholtz-Zentrum Dresden - Rossendorf with the support of Jens Zscharschuch, Holger Lange and collaborators from the Technical University of Munich.

The working principle of the interferometer setup is as follows. The freely suspended resonator is exposed to normally impinging laser light. The laser light, with a spot bigger than the width of the resonator, reflects from the substrate and the string, creating interference. This results in an oscillation of the intensity of the reflected laser beam from the sample. So, the remaining signal gives the resonator's vibration peak around the resonance frequency. Lorentzian fitting to the measured spectra gives the resonant frequency and quality factor.

Figure 4.10a illustrates the laser light's path and the main optical components of the setup. A laser (1) with a $\lambda$=785 nm and maximum power 125 mW is used as a coherent light source. After passing through the iris, the beam is split into two beams through BS I. Afterwards, the beam passes another beam splitter, BS II, and then a 20$\times$ objective with NA 0.25. Focused light then goes on the sample through the glass of the vacuum chamber. The reflected light follows the same path and is split from the beam splitter BS II to another beam splitter BS III. Part of the beam goes to the LED, and the other part goes to the camera, which is connected to the computer for visualisation. The camera collects the small part of the laser light, and the LED light is reflected from the sample. Then, the laser spot and the structure can be seen on a computer.

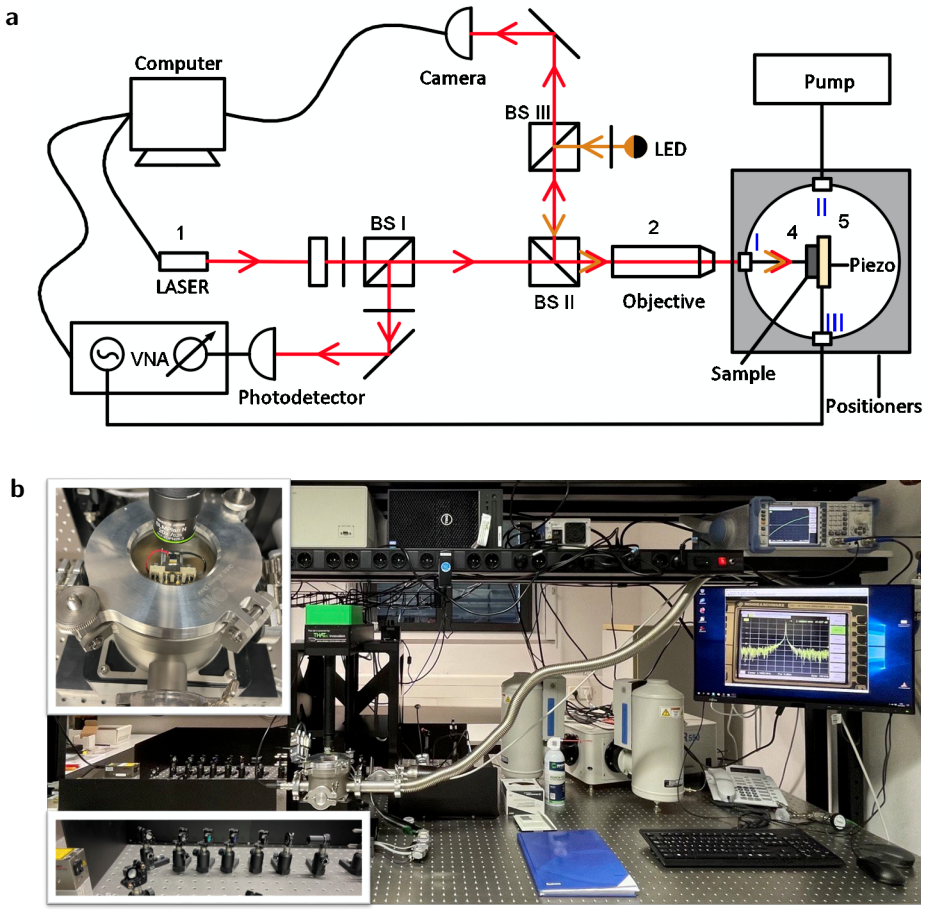


**Fig. 4.10: Fabry-Pérot interferometer setup.** (a) Schematic showing essential components and the general arrangement of the setup. (b) The photograph shows the arrangement on the optical table with insets showing lenses and a vacuum chamber with a mounted sample. On the computer screen, a resonance spectrum is captured.

The vacuum chamber is mounted on the positioners capable of XYZ movements with a precision of 100 nm. A vacuum pump Leybold Turbolab Core 90i is used to maintain a vacuum of about $5\times10^{-5}$ mbar to minimise gas damping and is connected to the chamber via a feedthrough II. The driving scheme for resonators is based on piezoelectric actuation. In the chamber, the sample is glued to the piezo plate with the help of a photoresist. The piezo plate is glued to the sample holder, and the sample holder is screwed on the base inside the chamber with glue. The piezo is connected using plug connectors to apply RF voltage from the vector network analyser (VNA) Rohde & Schwarz ZVL, capable of operating from 5 kHz to 13 GHz. The applied RF voltage vibrates the piezoelectric crystal, resulting in the resonators' mechanical vibrations. The RF voltage is provided by the integrated microwave source of the VNA.

Laser light reflects from the resonator and substrate, causing interference. On the return path, the beam is reflected from the BSI to the photodiode of the photodetector. A photodetector receives the optical signal from the vibrating resonators and converts it into voltage. The photodetector is connected to the VNA via an SMA cable and measures the resonator's response.

## 4.4 Helium Ion Implantation

Since the beginning of ion implantation experiments, helium has been used for semiconductor applications, along with silicon, hydrogen, nitrogen, and argon. Helium can be used for ion implantation, defect engineering, and local modification of material properties with the helium ion microscope (HIM). With higher fluence, the material is removed by sputtering or added by gas-assisted deposition for nanofabrication applications. Being the second lightest material, the interaction volume of the helium ions is narrow, especially in the few hundred nanometers of the material. Small interaction volume means defect formation and material modification can be localised with minimal spread. With HIM energy, the spread of ions can be smaller than 1 eV, leading to lower chromatic aberration and a de Broglie wavelength of 0.08 pm. Therefore, the diffraction effects do not limit the beam size, which is smaller than 1 nm. For imaging, HIM offers advantages such as high resolution (0.25 nm) than scanning electron microscopy (SEM), extended depth of focus, and novel contrast mechanisms[184,185].

We have used a DANFYS 1090-50 air-insulated accelerator produced by Danfysik to implant helium. It is an electrostatic accelerator with a nominal voltage of 40 kV. The SO140 ion source is integrated directly into the air-insulated high-voltage terminal and can be supplied with up to 40 kV. The positively charged ions generated by electron impact ionisation in the ion source are accelerated towards the ion beam line. The maximum acceleration voltage achieved is 40 kV. To achieve homogeneous implantation, the ion beam is scanned over the sample in horizontal and vertical directions by deflecting plates supplied with a voltage ($f \sim 1$ kHz). The vacuum inside the sample chamber is around $1\times10^{-7}$ mbar.

This chapter has focused on understanding the motivation and working mechanisms of two unique and emerging etching techniques: MACEtch and PEC etching. Afterwards, Fabry-Pérot Interferometry for characterising mechanical resonators is described. Finally, the critical features of helium implantation, followed by the technical details of the implanter, are described. In the next chapter, the key results will be presented.

# Chapter 5

# Results

The Results chapter describes the principle outcomes of my doctoral research. First, the MACEtch optimisation process is explained, which includes details about changes in electron beam lithography design, the morphology of the metal film, and the ratio of chemicals used for metal-assisted chemical etching (MACEtch). The results from spectroscopic measurements of ion-implanted pillars will be presented in the subsequent section. In addition, a wafer-scale fabrication protocol to create single G-centres and W-centres is described.

The second part will focus on the hybrid spin-mechanical systems involving 3C-SiC and 4H-SiC. First, I will present preliminary results of photoelectrochemical (PEC) etching for the fabrication of resonators in 4H-SiC, which is in the development phase. Next, the technique used in this work to characterise nanomechanical strings using Fabry-Pérot interferometry is described.

In the end, SRIM simulation results are explained, followed by the effect of helium ion implantation of mechanical resonators. The last subsection presents changes in mechanical properties, mainly Young's modulus and stress of resonators with incremental implantation fluences, estimated from the interferometric measurement data.

## 5.1 Telecom Photon Emitters in Silicon

The following section is based on our publication: Michael Hollenbach, Nagesh S. Jagtap, Ciarán Fowley, Juan Baratech, Verónica Guardia-Arce, Ulrich Kentsch, Anna Eichler-Volf, Nikolay V. Abrosimov, Artur Erbe, ChaeHo Shin, Hakseong Kim, Manfred Helm, Woo Lee, Georgy V. Astakhov, Yon-

der Berencén; Metal-assisted chemically etched silicon nanopillars hosting telecom photon emitters. J. Appl. Phys. 21 July 2022; 132 (3): 033101. https://doi.org/10.1063/5.0094715; licensed under a Creative Commons Attribution (CC BY) license[40]. In this work, I fabricated the samples, Dr. Michael Hollenbach performed the spectroscopic measurements. Details about the authors' contributions can be found in Appendix B[1].

### 5.1.1 Electron Beam Lithography

**Table 5.1: EBL dose for pillars**

| Pillar diameter (nm) | Dose Factor | Dose ($\mu C\,cm^{-2}$) |
|---|---|---|
| 1100 | 0.9 | 117 |
| 900 | 1.15 | 149.5 |
| 700 | 1.3 | 169 |
| 500 | 1.4 | 182 |
| 300 | 1.6 | 208 |

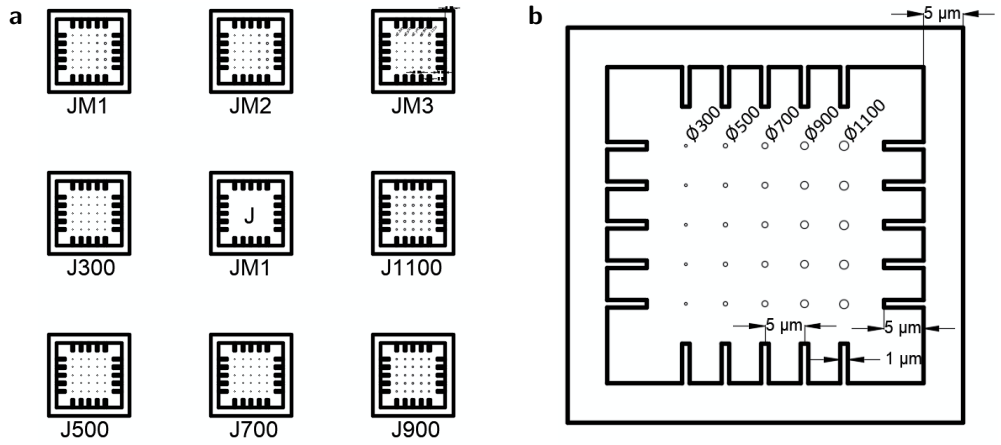


**Fig. 5.1: EBL design of silicon nanopillars.** (a) Arrays J300 to J1100 consist of ⌀ 300 nm to ⌀ 1100 nm nanopillars, and JM serves as a control. Arrays JM1, JM2, and JM3 include pillars with all five diameters. (b) Array JM3 shows the dimensions of the frame, pillars, pitch, and pins.

[1]Dr. Michael Hollenbach and I contributed equally to this work (data curation, formal analysis, investigation, visualisation, and methodology)

Table 5.1 describes the optimum electron dose for pillars with different diameters estimated by dose tests. The base dose is 130 μC cm$^{-2}$. To systematically study the effect of different pillar diameters on the spectroscopic properties of the single photon emitters, we have created arrays of pillars with varying diameters, as shown in Figure 5.1a.

The arrays consist of 5×5 nanopillars with diameters ranging from ⌀300 nm to ⌀1100 nm. Arrays in the top row have a column-wise combination of all five pillar sizes, as shown in Figure 5.1b. 5 μm centre-to-centre pitch between the pillars is to avoid cross-talk losses between neighbouring photonic elements when working with the optical telecom bands[186]. The central array serves as a control and marker for the spectroscopic measurements. The 1 μm × 5 μm rectangular pins are added to overcome the technical problem of the confocal microscope.

### 5.1.2 Metal-Assisted Chemical Etching

In the preliminary experiments, we deposited 30 nm Au film as a metal catalyst for MACEtch. However, the thick metal film separated, and Si was not etched. This was confirmed by scanning electron microscopy (SEM), and film removal is attributed to a lack of material removal pathways. Si, being etched underneath the gold, is removed around the periphery of the structures and open areas (without gold, if resist is removed prior to MACEtch). When material removal pathways are insufficient and not in balance with the material dissolution rate, byproducts tend to escape by diffusing through the film. 30 nm Au film is too thick for byproducts to diffuse through, and the film gets detached from the Si.

Later, we have reduced the Au layer to 10 nm. It resulted in non-uniform etching with metal film breaking off in some regions. With the extended Au film covering the complete sample area, the only available path for mass transfer is around the nanostructures, similar to the first case. However, the thin film allows mass transfer by breaking off in some regions.

In extended areas without nanostructures, if the diffusion rate of byproducts outwards through the film is not in balance with their generation, the metal film is pushed away from the sample, resulting in the film being removed or torn. This imbalance leads to film peel-off, resulting in non-uniform, conical, and rough nanopillars. To overcome the problem, we added frames to separate the pillars from the extended film. If the film in the long, extended regions outside the frames breaks, it does not affect the etching inside the frames; the metal film stays intact. Nevertheless, artefacts are formed outside the frames due to the breaking of the extended film (Figure 5.3a).

To improve the etch quality, we have conducted calibration experiments. P-type <100> oriented 525 µm thick Si wafer is diced into 2 cm × 2 cm pieces and processed as per the fabrication protocol mentioned in Section 4.1. Before the last MACEtch step , the sample is diced into smaller 5 mm × 5 mm pieces to experiment with different etch recipes. This reduced the processing time by several hours per sample. Table 5.2 describes MACEtch optimisation parameters: etch chemistry, etching time, rate, and quality of the fabricated nanostructures.

**Table 5.2: MACEtch optimisation.** Summary of the effect of different etch recipes on the etch rate and quality of nanopillars. The sample MC2 gives the best quality of nanostructures results with the etch rate 205 nm $min^{-1}$.

| Sample | HF (mL) | $H_2O_2$ (mL) | DI Water (mL) | Time (min) | Etch Rate (nm $min^{-1}$) | Etch Quality |
|---|---|---|---|---|---|---|
| MC1 | 50 | 9 | 240 | 10 | 410 | average |
| **MC2** | **50** | **9** | **300** | **10** | **205** | **best** |
| MC3 | 50 | 4 | 240 | 5 | 25 | good |
| MC4 | 100 | 4 | 240 | 5 | 85 | average |
| MC5 | 50 | 9 | 360 | 10 | 145 | bad |

Key results from the MACEtch optimisation experiments are explained in this section. Samples are etched by changing the ratio of the etchants as shown in Table 5.2 and characterised using SEM. By carefully analysing the images, our understanding of the process has significantly enhanced[40].

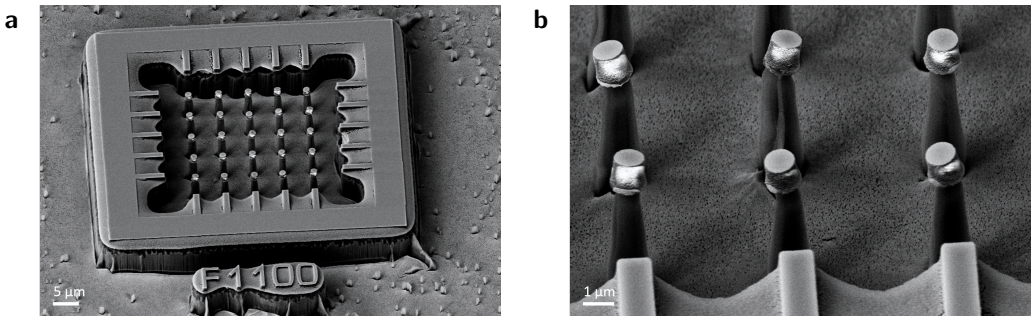


**Fig. 5.2: SEM images of MC1.** (a) Array of ⌀1100 nm nanopillars with 5 µm height surrounded by frame. Artefacts are formed outside the frames due to the Au film breaking off. (b) High aspect-ratio ⌀900 nm nanopillars with resist on the top and tapered shape showing signs of anisotropic etching.

High aspect-ratio nanopillars were fabricated in MC1. Etching was uniform across the sample with an etch rate of 410 nm $min^{-1}$. However, the etching quality was not good and worsened with time. Degradation in etch quality was confirmed by comparing the sample etched for 5 min (not shown). The walls of the pillars were smooth, but the etching had a partial isotropic nature, as shown in Figure 5.2b. Because the reaction byproducts are generated faster than their removal, the metal film seems to have strained or torn in some areas, making Si more accessible to the solution. As etching proceeds, the higher concentration of $H_2O_2$ leads to excess holes, and etching proceeds in non-<100> directions, resulting in tapered pillars.

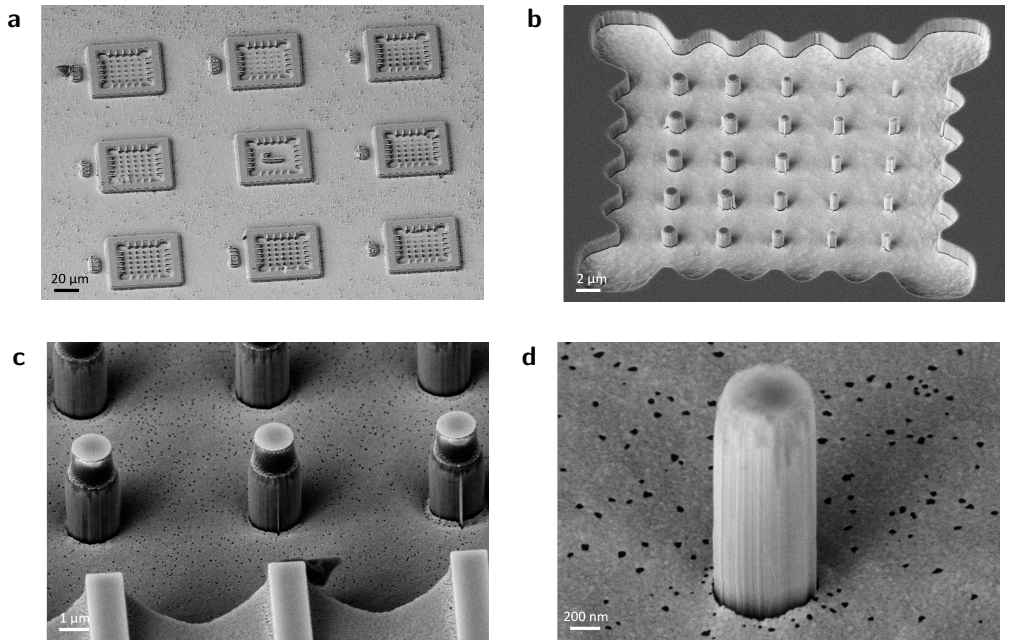


**Fig. 5.3: SEM images of MC2.** (a) Set of all nanopillar arrays showing uniform etching. (b) An array of nanopillars with diameters from 1100 nm to 300 nm (left to right columns) after lift-off is shown. Sidewall Smoothness improves with diameter due to the longer peripheral length available for byproducts to escape. (c) Close view of ⌀1100 nm smooth and anisotropic nanopillars with resist on top. (d) A ⌀700 nm pillar with 1200 nm height after lift-off: Roughness on the pillar top is due to the imbalance between etch byproduct formation and removal at the beginning of etching. Adapted from Reference [40].

For MC2, with a solution consisting of 50 mL HF, 9 mL $H_2O_2$ and 300 mL DI water, the best quality pillars were fabricated: smooth and vertical sidewalls, moderate etch rate ($\sim$200 nm $min^{-1}$) and good etch uniformity across the sample. As explained in the section 4.1.2, the metal catalyst plays a vital role in

MACEtch. 10 nm Au film allows mass transfer by diffusion. In the initial etching stage, the diffusion of byproducts through the metal film is slower. Because the byproducts are escaping only from the periphery of the nanostructures, the part of Au film around the structures is removed. An up-turn of the film can also be seen in Figure 5.3d, leading to an increase in pillar diameter. In parallel, diffusion of the byproducts through the metal film makes it porous. A point is reached where the generation and removal of reaction byproducts are balanced: etching becomes anisotropic, and film porosity does not increase further. This explanation is supported by the fact that the pillar uniformity within the arrays increases with pillar diameter as the path available for material to escape increases, as shown in Figure 5.3b.

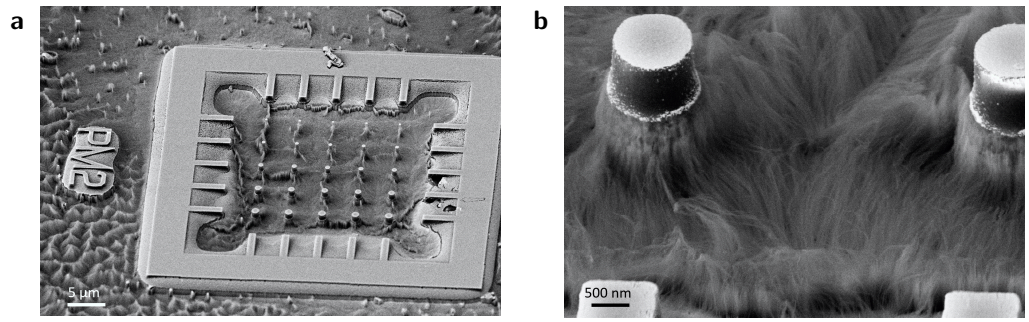


**Fig. 5.4: SEM images of MC5.** (a) Etching created very non-uniform structures, and even outside the frames, Au film broke, leading to surface irregularities. (b) A close view showing rough pillar sidewalls and a porous floor: The etching was initially anisotropic, where pillars formed. Later, due to an imbalance of byproducts, Au film breaks, and etching becomes uniform. Densely packed nanowires are formed due to powder-like Au particles etching in Si.

The sample MC3 was etched with the solution consisting of half the $H_2O_2$ volume compared to the sample MC1, resulting in 16 times slower etching. The reduced etch rate is due to hydrogen peroxide's lower hole supply rate. When HF volume was doubled in the case of the sample MC4, the etch rate increased three times. This is attributed to the fact that a higher concentration of HF removes oxide faster, resulting in faster etching.

In the case of MC5, further dilution of $H_2O_2$ leads to nonuniform etching: rough sidewalls of pillars and porous floor area (region inside the frames in between the pillars). When comparing the results of a sample etched for 5 min, it becomes clear that etching worsens with time for the sample MC5. The Au film detaches from the sample surface. Also, Au particles separate and continue etching, leading to tiny, hairy structures. The detailed mechanism is complex and needs further investigation.

### 5.1.3 Ensembles of G-Centres in Silicon Nanopillars

After the fabrication of Si nanopillars, we create G-centres by a carbon broad beam ion implantation. Without removing the thin gold film, we implant carbon at a fluence of $2\times10^{14}$ cm$^{-2}$ and with an energy of 250 keV. The G-centres are created at a depth of about 600 nm in the pillars with 1200 nm height. The broad beam ion implantation protocol creates G-centres everywhere in the sample. 10 nm gold film is not thick enough to stop the ions in the etched areas. During the confocal measurements, the gold film reduced the intensity of the G-line emission from the chip floor (areas without the extended features).

The optical experiments were performed in a low-temperature confocal photoluminescence microscope. Details about the experimental setup and its configuration for measurement of G-centres can be found elsewhere[37,40,75]. A 2D PL scan of ⌀1100 nm nanopillar array shown in Figure 5.5a confirms the presence of optically active G-centres. A PL spectrum at 6 K of one of the pillars (marked with a red circle in Figure 5.5a) exhibits a sharp zero phonon line (ZPL) peak at 1278 nm along with a broad phonon sideband (PSB) at lower wavelengths (Figure 5.5b). The ZPL at 1278 nm accompanied by PSB is the spectroscopic fingerprint of the G-centre[74].

The probability of coherently emitting light into the ZPL is called the Debye-Waller (DW) factor, and it is one of the essential characteristics of single-photon emitters (SPE). Our results show a DW factor of 12%, which agrees with the previously reported values[37,39]. Also, a sample processed by the same fabrication protocol does not show any PL emission in the O-band (black curve in Figure 5.5b). Hence, the proposed fabrication protocol, including MACEtch, to create the nanostructures does not introduce G-centres or other optically active defects emitting in the telecom O-band.

Figure 5.5c illustrates the PL line scan along a row of ⌀1100 nm pillars denoted by the dotted line in Figure 5.5a. The normalised PL intensity increases at the pillars having ensembles of G-centres, and confirms a 5 µm pitch between the pillars compared to the fabrication design. Figure 5.5d shows ZPL intensity for pillars with different diameters, indicating the presence of ensembles of G-centres. All pillars show strong ZPL emission in the O-band, and emission from ⌀1100 nm pillars was the highest. ⌀300 nm pillars did not show any PL emission, and this can be attributed to scattering losses due to rough sidewalls. The ZPL intensity depends on various factors, such as the number of G-centres incorporated in the pillar, scattering losses, size, shape, and roughness. A thorough understanding of the influence of these parameters is complex and out of the scope of this work.

We have measured a laser power-dependent saturation curve of the integrated

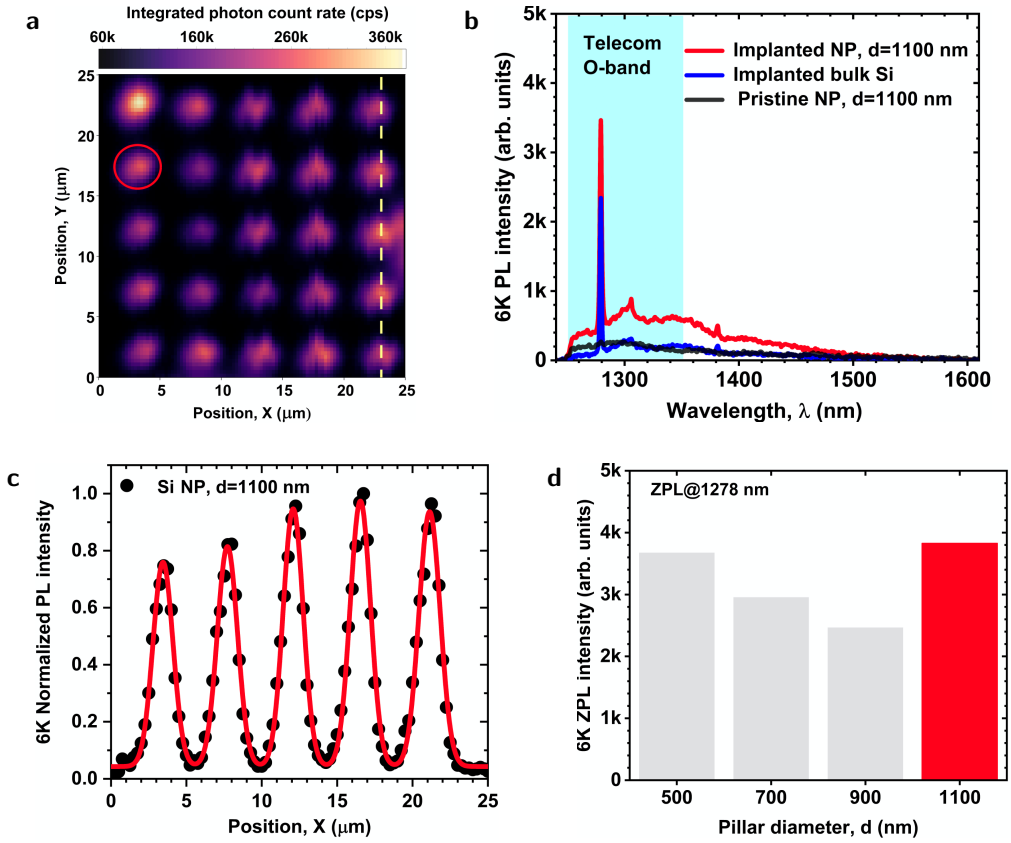


**Fig. 5.5: Low-temperature confocal photoluminescence spectroscopy I.** (a) 2D confocal PL scan performed at 6 K of a ⌀1100 nm array, confirming the presence of optically active G-centres. (b) Typical low-temperature PL spectrum of a G-centre telecom photon emitter (red curve) recorded on the nanopillar highlighted with a red circle in (a). Emission from the pillar is enhanced due to the waveguiding effect when compared with emission from bulk Si (blue curve). (c) Normalised PL line scan along ⌀1100 nm pillars (dashed line in (a)). (d) 1278 nm ZPL intensity as a function of diameter for MACEtch fabricated pillars. Adapted from Reference [40].

photon count rate, shown in Figure 5.6a. We calculate the background by taking the difference in emission from the etched areas covered with gold and the pillar. A background-corrected saturation curve was fitted with the saturation equation of an ensemble of a two-level system to estimate the maximum intensity, and the equation is given by[82],

$$I(P) = I_{\text{max}} \cdot \ln\left(1 + \frac{P}{P_0} \cdot \ln(2)\right) \tag{5.1}$$

where $I(P)$ is the PL intensity dependent on the excitation power $P$, $P_0$ is the saturation power, and $I_{\text{max}}$ is the photon count rate when saturated. The

saturation count rate was 210 kcps and 2 mW power, which leads to a power density of 260 kW cm$^{-2}$. The PL intensity of the G-centres integrated into the Si pillar is enhanced by a factor of 1.2 as compared to the signal from the G-centres in the bulk Si (Figure 5.6a). The emitted light from bulk Si is scattered at the Si/air interface. In the case of pillars, however, directional emission due to the waveguiding effect leads to a higher PL intensity.

For a given excitation power, PL intensity increases for all the pillar diameters. The PL scan along the depth of the sample is shown in Figure 5.6b. The integrated photon count rate at the pillar (red) is compared with the signal from bulk Si (blue). The shift in the peak position and higher integrated photon count rate indicate that the photon collection efficiency in Si pillars is higher than in bulk Si. Because of the waveguiding effect, which is based on total internal reflection (TIR), the full width at half maximum (FWHM) of the PL signal from pillars is 3.5 times narrower than the bulk. Improved PL signal shows that the nanopillars allow the emission to be coupled and guided by a high refractive index material (Si) surrounded by a low refractive index material (air) due to TIR.

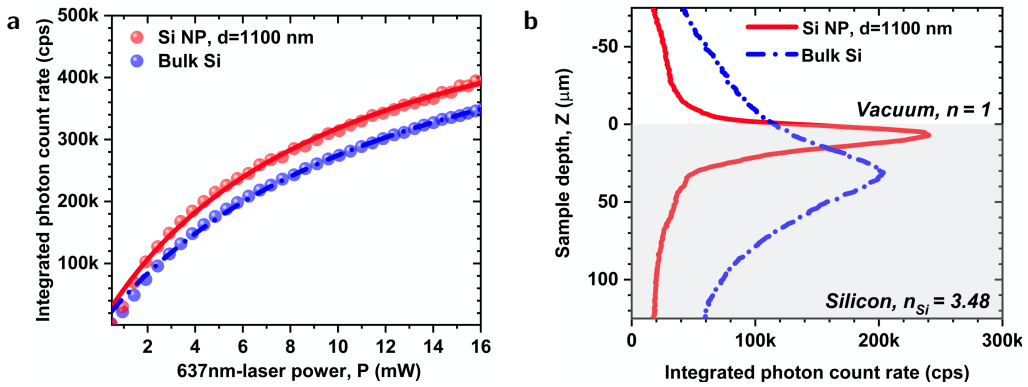


**Fig. 5.6: Low-temperature confocal photoluminescence spectroscopy II.**
(a) Power dependence of telecom photon emitters integrated into a Si nanopillar with reference to bulk Si is shown. (b) In-depth (z-axis) integrated photon count rate recorded from a ⌀1100 nm pillar and bulk Si. Adapted from Reference [40].

Notably, unlike most of the other MACEtch works with densely packed nanostructures[144] or separated microstructures[154], we have fabricated isolated[40] photonic nanostructures with superior quality and uniformity. In conclusion, we have successfully integrated ensembles of G-centres in Si nanopillars, which is confirmed by the low-temperature PL measurements. Our proposed fabrication protocol with MACEtch does not introduce G-centres or other optically active defects in the telecom O-band. We demonstrated that the PL signal from the G-centres integrated into the nanopillars is enhanced due to the waveguiding effect. Integrating G-centres in photonic structures is the first step towards incorporating

single telecom-photon emitters in Si photonic structures, which is a fundamental building block of QPIC. To integrate a single G-centre in Si nanopillars, lower implantation fluence, perhaps in combination with fabricating smaller diameter pillars, will provide a solution.

### 5.1.4 Wafer-Scale Nanofabrication of G- and W-centres

In the follow-up work, we have created both G-centres and W-centres by fabricating a photoresist mask with lithographically defined arrays of nanoholes, followed by a broad beam silicon implantation. Our work is reported in the Nature Communication publication: Michael Hollenbach, Nico Klingner, Nagesh S. Jagtap, Lothar Bischoff, Ciarán Fowley, Ulrich Kentsch, Gregor Hlawacek, Artur Erbe, Nikolay V. Abrosimov, Manfred Helm, Yonder Berencén Georgy V. Astakhov; Wafer-scale nanofabrication of telecom single-photon emitters in silicon. Nature Communications 12 December 2022; 13 (1): 7683. https://doi.org/10.1038/s41467-022-35051-5; Creative Commons Attribution 4.0 International (CC BY) License[41].

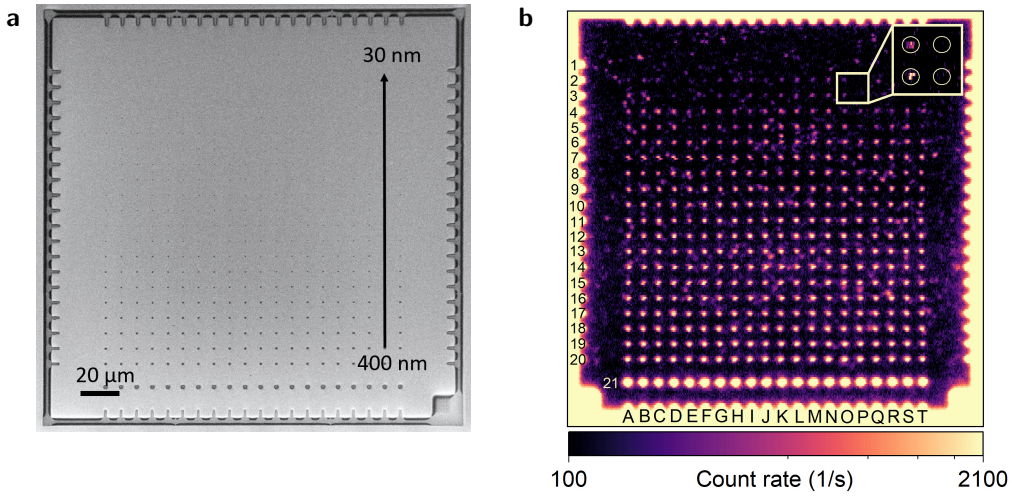


**Fig. 5.7: Wafer-scale nanofabrication of single G-centres.** (a) SEM image of patterned nanoholes with diameters varying from 400 nm to 30 nm (top to bottom) on an SOI substrate and (b) confocal PL intensity map of locally created G-centres after $Si^{+2}$ broad-beam implantation are shown. The inset shows four spots with singles (left row) and no G-centres (right row). Adpated from Reference [41].

The fabrication details are as follows. First, 5 mm × 5 mm SOI sample is annealed to reduce the background using rapid thermal annealing (RTA) at 1000 °C for 3 min in nitrogen atmosphere. Next, sample is cleaned with piranha solution

(mixture sulphuric acid and hydrogen peroxide) to remove residual C- and O-terminates. Before spin coating, the sample is ultrasonically cleaned in acetone, rinsed in IPA, and dried with a nitrogen stream. Afterwards, sample is spin-coated with a positive-tone resist PMMA 950K A6 with a nominal thickness of 320 nm, followed by a hot plate bake at 150 °C for 5 min.

Next, we define nanohole patterns with diameters ranging from 30 to 400 nm using the Raith 150TWO EBL tool, as shown in Figure 5.7a. We use 20 kV acceleration voltage, 30 µm aperture, and 820 µC cm$^{-2}$. By varying the nominal diameter of nanoholes, the number of implanted ions is controlled by keeping the ion fluence constant (broad-beam implantation). Afterwards, the sample is developed in DI water: IPA (3:7) for 30 s followed by an IPA dip to stop the development process and dried using a nitrogen stream.

Afterwards, we create G-centres using $Si^{+2}$ broad-beam implantation with an energy $E$=40 keV, at a fluence $\Phi$=1×10$^{12}$ cm$^{-2}$ and an angle $\theta$=7° to avoid channelling. Next, the resist is removed using ultrasonication at low power, followed by an IPA dip and a nitrogen blow-dry. Figure 5.7b shows the confocal PL intensity map of the created G-centres after implantation. The second-order autocorrelation function $g^{(2)}(\tau)$ obtained on spot M3 yields $g^{(2)}(0) = 0.22 \pm 0.08$ and unambiguously points to a single G-centre. Based on $g^{(2)}(\tau)$ measurements, we have found that more than 50% of the nanoholes with nominal diameters of 35 and 40 nm contain single G-centres.

Similarly, W-centres are created in ultrapure Si samples (carbon $5 \times 10^{14}$ cm$^{-3}$ and oxygen $1 \times 10^{14}$ cm$^{-3}$) with the same fabrication and $Si^{+2}$ implantation protocol ($E$=40 keV, $\Phi$=1×10$^{12}$ cm$^{-2}$, $\theta$=7°). No annealing was performed as the post-implantation annealing at 225 °C leads to a high background. We confirm from PL measurements that the 300 nm hole corresponds to single-photon emission from a W-centre. Therefore, we have successfully created single G- and W-centres on a wafer scale. For more details, readers can refer to our article published in Nature Communications[41]. The details about the authors' contributions can be found in Appendix B.

## 5.2 Mechanical Resonators in Silicon Carbide

### 5.2.1 Photoelectrochemical Etching

Photoelectrochemical etching (PEC) is a dopant-selective technique used to release resonators p-SiC by removing n-SiC underneath for fabricating free-standing structures. We used 300 µm thick, heavily nitrogen-doped 4H-SiC samples to

calibrate the PEC setup. 100 nm Ni is deposited on the back side of samples to form an ohmic contact prior to etching. The voltage was maintained at 200 mV, and current was recorded during all the experiments. Figure 5.8 shows the current versus time (I-t) plot and SEM images of porous SiC formed.

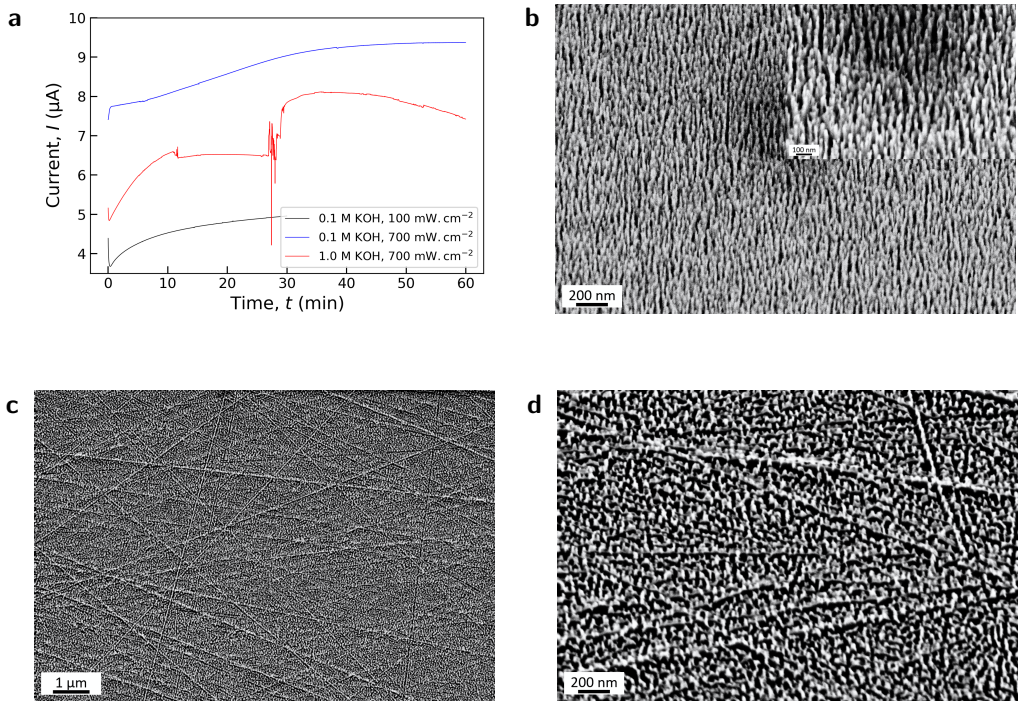


**Fig. 5.8: Calibrating PEC etching with n-4HSiC.** (a) I-$t_{200\ mV}$ plot for three different experiments with variation in light intensity and KOH concentration. (b) SEM image of vertical nanowires fabricated with 0.1 M KOH and 700 mW cm$^{-2}$ for 60 min with inset showing the magnified view. (c) An SEM image of a sample etched with 1.0 M KOH and (d) its magnified view shows that etching creates nanowire-like structures and is not entirely isotropic.

Figure 5.8a shows three different plots of current versus time at a constant bias of 200 mV (I-$t_{200\ mV}$). The maximum current density is directly proportional to the etch rate[170]. For all the experiments, the current first drops and then starts rising. In the first case (black curve), the light was not focused, and the sample was etched for 30 min. There is a linear increase in current over time. In the second experiment (blue curve), light is focused on a ⌀15 cm spot, and the expected light intensity is about 700 mW cm$^{-2}$. The higher the number of photons, the more holes are available for oxidation, and therefore, the current increases linearly with increasing light intensity until saturation has reached.

If the applied bias is constant, the measured current should not change much

in the case of non-porous etching. However, porous etching results in a larger surface area (50–60 times[177]) and hence a higher number of collected holes and current density. After a certain thickness of interpore spacing is achieved, which depends on the thickness of the space charge or depletion layer, the semiconductor starts behaving like a semi-insulating material, and therefore, the current drops with time. Also, when the pores are deeper in the sample, the amount of photons reaching the SiC-KOH interface reduces, leading to a drop in current[177].

The third experiment used concentrated KOH to achieve higher currents and etch rates. Higher $OH^-$ concentrations will etch the formed oxide faster until it becomes oxidation rate-dependent due to limited hole supply. Dorp and colleagues have shown that from 0.1 M to 1.0 M KOH concentration, the etch rate increases with a forward shift in bias voltage corresponding to the maximum current for p-SiC[170]. In the third experiment with 1.0 M KOH and focused light (red curve), the current increases and then saturates. During the experiment, the plano-convex lens was moved to achieve the maximum current, and that is the cause of the noise after 30 min. Although higher currents are reached after adjusting the position of the lens, the current starts dropping.

During the process, the oxide may form faster than its removal rate, creating a passivation layer and a drop in current. The passivation layer can be effectively removed during etching by stirring the electrolyte. It is worth noting that the shape and size of pores vary with the KOH concentration. Concentrated KOH results in more triangular-shaped pores, which have been previously reported by Shishkin and coauthors[177]. However, the origin of the formation of nanowire-like structures observed (Figure 5.8b) is still unclear. Next, the results of the test experiments with 4H-SiC are described.

In the preliminary experiments, 4H-SiC samples were fabricated using the protocol mentioned in Section 4.2.1.2. Samples were etched at 200 mV with light intensity 100 $mW\,cm^{-2}$ and 0.1 M KOH for 5 min. I-$t_{200\ mV}$ plot and SEM images are shown in Figure 5.9. Figure 5.9a shows that the current first drops suddenly before it increases and then drops again, like in the case of n-SiC. However, the time scale is shorter than that of n-SiC. Unfortunately, SEM images show that n-SiC is etched in a porous manner and p-SiC is affected by etching, which is undesirable in our case. Ideally, PEC etching should only etch the n-SiC layer. Here, why n-SiC gets affected is unclear and needs further investigation.

For all experiments with n-SiC and bilayer SiC samples, a maximum current of about 9 µA was recorded. With an active area of 0.07 $cm^2$, the corresponding current density is 0.128 $mA\,cm^2$. Compared with the literature, this value is one or two orders of magnitude lower, even with porous etching of n-SiC[177]. The origin of the low current can be attributed to the improper back contact, the

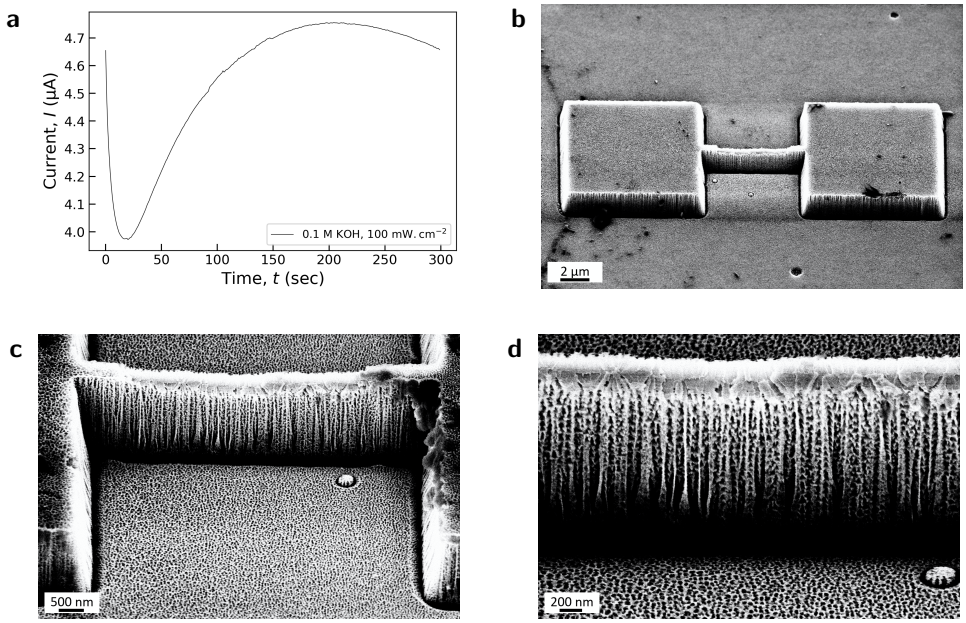


**Fig. 5.9: PEC etching of bilayer SiC.** (a) I-$t_{200\ mV}$ plot for bilayer SiC with light intensity 100 mW cm$^{-2}$ and 0.1 M KOH. (b) SEM image of a structure, and (c) magnified view showing the bent and damaged bridge where both p- and n-SiC are etched. (d) An SEM image of the porous underetching of the resonator is shown. The etch selectivity is achieved, but the p-SiC bridge is damaged. Also, distinct triangular structures and pores are formed in the underlying n-SiC layer.

PECC arrangement, and the contact resistance. Whiteley and others have performed an annealing step to make an ohmic contact with metal[170,182,183]. In the following experiments, measuring resistance with different contacts and annealing is helpful to ensure the ohmic behaviour. Also, in the PECC arrangement, modifications are needed to make an electrical connection to the sample with a thin plate or wire to minimise contact resistance.

Shishkin and coauthors reported the formation of triangular-shaped pores by PEC etching of n-type 4H-SiC dilute hydrofluoric acid as an electrolyte at low voltage and low current conditions. A distinct triangular shape is associated with the different surface energies and resistance to electrolytic attack on different planes. As mentioned previously, the pore size and shape mainly depend on the thickness of the space charge layer, which is a function of the potential drop in the space charge region and doping concentration. Also, one of the reasons for lower currents in our experiments could be low doping, and this argument is also supported by Magyar[177,182]. Also, it is possible to thermally oxidise and etch porous SiC using HF[168,187].

In conclusion, we have achieved etch selectivity in p- and n-SiC, but the etching of the n-SiC is porous. Porous layers can be removed by oxidation, followed by dipping in HF. Also, improvement of PECC design and electrical contacts is needed and is a work in progress.

### 5.2.2 Characterisation of Strings

This section presents results from our collaboration with Prof. Eva Weig's group from the Technical University of Munich. The manuscript based on our work is published in the ArXiv - P. Bredol et al., *Effect of Helium Ion Implantation on 3C-SiC Nanomechanical String Resonators*, arXiv:2405.02035 [cond-mat], May 2024. In this work, I have performed electron beam lithography to define the nanostructures, SRIM simulations to prepare implantation experiments and estimate defect concentration, and supported manuscript writing.

In the following sections, Figure 5.11 and Figure 5.12 show the data I measured in Prof. Weig's lab at TU Munich with support from Dr. Yannick Klaß. While Figures 5.13 and 5.15 present the data measured by an automatic Python program developed in Prof. Weig's group by Dr. Philipp Bredol.

Nanomechanical strings in 3C-SiC are fabricated by using the protocol mentioned in Chapter 4 (Section 4.2). Figure 5.10 shows SEM images of the strings of varying lengths (20 to 110 µm) with the same nominal width of 300 nm. The thickness of the resonators is 110 nm and is defined by the thickness of the CVD grown SiC layer on Si(111) substrate.

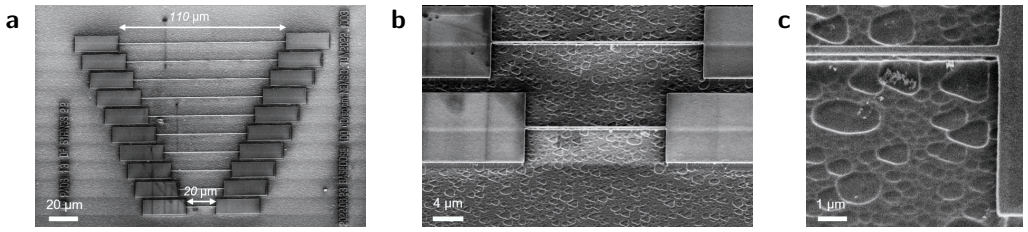


**Fig. 5.10: SEM images of nanomechanical resonators.** (a) Harp of strings of varying length ranging from 20 µm to 110 µm (bottom to top). (b) Magnified view of a 20 µm string. (c) A close view shows the undercut of the string and triangular voids on Si originating from the CVD growth process.

Next, we characterise strings before and after each implantation step to record mechanical response using a Fabry-Pérot interferometer. The measured mechanical response is fitted by the square root of a Lorentzian using MATLAB or Python code. The frequency at the maximum amplitude is the resonant frequency $f$ of

the resonator. FWHM is a measure for the energy dissipating per cycle ($\Gamma$), and from that, we calculate the quality factor of the resonator ($Q{=}f/\Gamma$).

Figure 5.11b shows the frequency response of a 110 µm string with Lorentzian fitting for the first out-of-plane (OOP) mode. Resonance frequency $f{=}2.13$ MHz and dissipation $\Gamma{=}31$ Hz gives the quality factor $Q{=}6.7\times10^4$. Through higher-frequency sweeps, higher modes are detected. Figure 5.11a shows sharp lines for the eight OOP modes of a 110 µm string. In-plane (IP) modes appear at slightly higher frequencies as compared to the respective OOP mode, as 110 nm thickness $h$ is replaced by the 300 nm width $w$ of the resonator in the Euler-Bernoulli equation. In the following discussion, only OOP modes are considered.

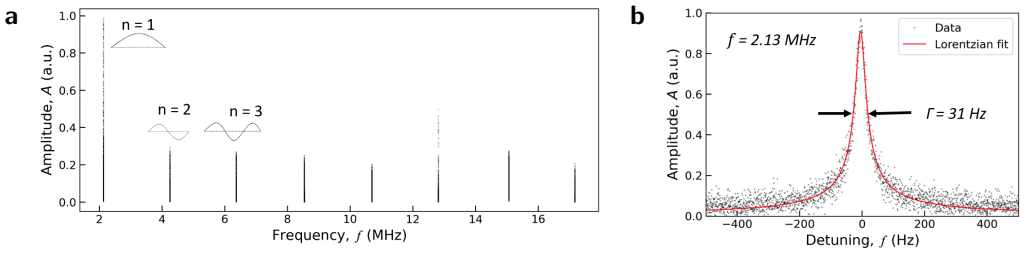


**Fig. 5.11: Characterisation of a string for $f$ and $Q$.** (a) The plot shows higher OOP modes with very sharp peaks for a 110 µm string. IP modes appear at frequencies slightly above the OOP modes (as width $w$ is higher than thickness $h$) and are excluded from spectra for simplicity. (b) Lorentzian fitting of the first OOP mode to estimate resonant frequency and dissipation.

Figure 5.12 shows the variation in resonant frequencies for OOP modes and quality factors for all string lengths. The Euler-Bernoulli equation is given by,

$$f(n) = \frac{n^2\pi}{2L^2}\sqrt{\frac{Eh^2}{12\rho}}\sqrt{1+\frac{12\sigma L^2}{n^2\pi^2Eh^2}}, \tag{5.2}$$

where $n$ is the mode number, $l$ is the length of the string, $E{=}400$ GPa is Young's modulus (reported for the same wafer[124]), $h{=}110$ nm is the thickness (in the direction of vibration), $\rho{=}3.2$ g cm$^{-3}$ is the density, and $\sigma{=}800$ MPa[188] is the stress. The experimental data agrees with the data calculated using the Euler-Bernoulli equation with the parameters mentioned earlier (Figure 5.12a). Figure 5.12b shows the corresponding quality factors, which increase with length.

It is noteworthy that the wafer stress is considered while calculating frequencies of all strings. However, the stress in each string is different due to the deformation of clamping pads caused by isotropic Si etching under the strings and pads. For

more details, readers can refer to the publication 'Universal Length Dependence of Tensile Stress in Nanomechanical String Resonators' by Maximilian Bückle and Dr. Yannick Klaß[116].

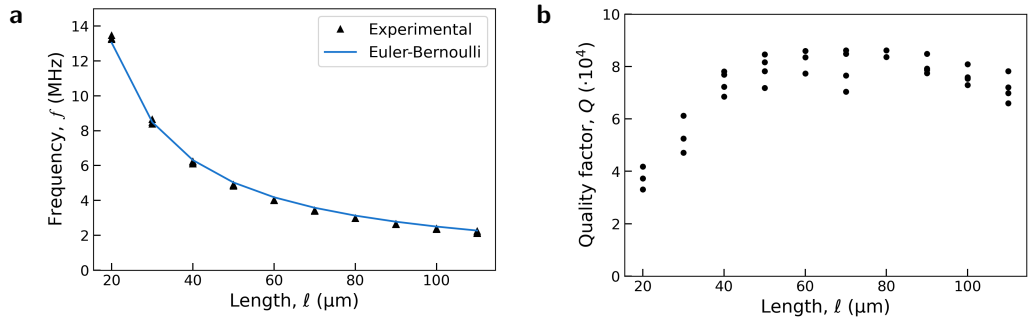


**Fig. 5.12: Characterisation: $f$ versus $l$ and $Q$ versus $l$.** (a) The plot shows fundamental OOP mode frequencies for all string lengths. The blue curve is calculated using the Euler-Bernoulli equation and agrees with the experimental data. (b) The plot shows corresponding quality factors for strings. Quality factors reduce for longer strings, but the reason is still unclear.

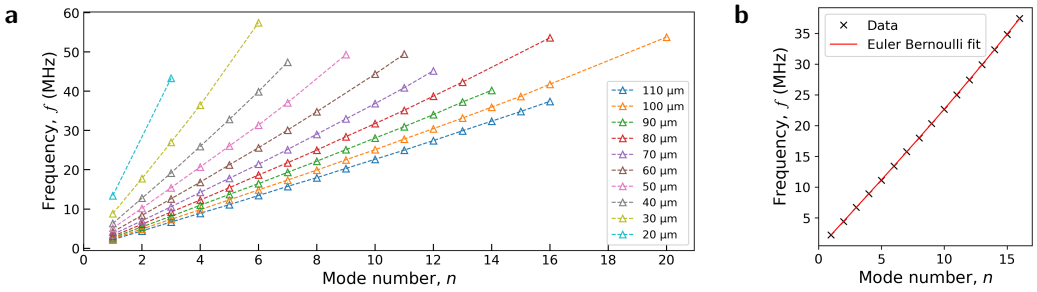


**Fig. 5.13: Characterisation: $f$ versus $n$.** (a) The plot shows frequencies for higher OOP modes measured for all strings. Detecting higher modes for shorter strings becomes challenging; only a few modes are shown. (b) The plot shows OOP modes for 110 μm string and Euler-Bernoulli fit to the data. Stress $\sigma$ and Young's modulus $E$ are calculated from the fit parameters (explained in the text).

Figure 5.13a shows frequency versus mode numbers for OOP modes of all strings. Reordering the Equation 5.2,

$$f(n) = \sqrt{a \cdot n^4 + b \cdot n^2}, \tag{5.3}$$

where a and b are fitting parameters and are given by,

$$a = \frac{\pi^2 h^2 E}{48 l^4 \rho}, \quad b = \frac{\sigma}{4 l^2 \rho}. \tag{5.4}$$

By fitting measured frequencies and mode numbers to Equation 5.2, we get the fit parameters $a$ and $b$. Inserting the values $l$=110×10$^{-6}$ m, $\rho$=3200 kg m$^{-3}$, $h$=110×10$^{-9}$ m, we get $E$=400 GPa, $\sigma$=767 MPa. The same fitting routine is used in this work to calculate Young's modulus and stress before and after each implantation step, considering simply supported boundary conditions. Measured frequencies and the fit function agree (Figure 5.13b), justifying our choice of boundary conditions.

### 5.2.3 Stopping and Range of Ions in Matter

We use the helium ion broad beam implantation technique to create silicon vacancies ($V_{Si}$) in SiC. Before finalising the experimental parameters, simulations using the stopping and range of ions in matter (SRIM) are performed. First, to fix the implantation energy, the projected range ($R_p$) versus the energy $E_I$ of ions is plotted as shown in Figure 5.14a.

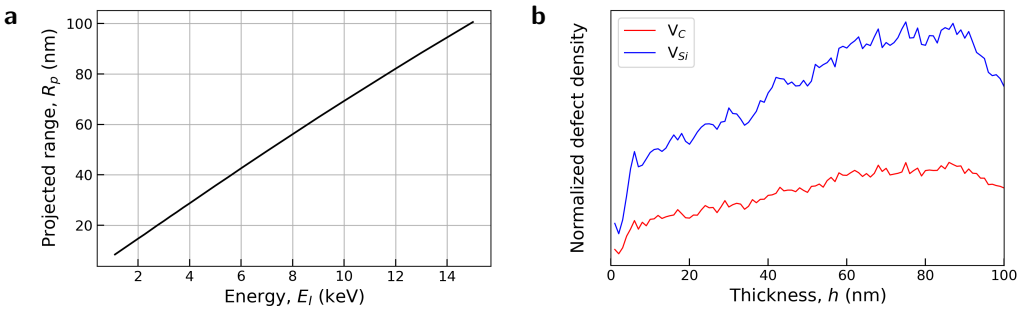


**Fig. 5.14: Helium ion range and normalised vacancy distribution.**
(a) Projected range $R_p$ versus energy $E_I$. (b) Normalised silicon and carbon vacancies produced along the thickness of the resonator: Energy $E_I$ of ions is selected so that most of the $V_{Si}$ are created in the lower half of the resonator.

Notably, changes in mechanical response after creating $V_{Si}$ and other types of defects are more likely to be detected when defects are away from the neutral axis (N.A.) of the resonator. Also, defects are well-defined away from the top surface when artificially created using ion implantation techniques. The thickness of the resonators is 110 nm, originating from the CVD-grown SiC device layer. Therefore, to create $V_{Si}$ in the lower part of the resonators, 14 keV implantation energy is selected, for which the corresponding $R_p$≈95 nm. SRIM helps us quantify the number of $V_{Si}$ and $V_C$ and their distribution along the resonator thickness is as shown in Figure 5.14b, confirming that more vacancies are created in the lower part of the resonator.

As we shall see in the later part of the thesis, a qualitative understanding of defects created due to ion implantation is crucial for nanomechanics. Therefore, we deduce the average number of vacancies from SRIM and multiply them by the fluence, which gives the total number of vacancies per unit volume. With the fluence $\Phi$=$10^{14}$ cm$^{-2}$, we have found defect density to be $V_{Si}$=$4.1 \times 10^{20}$ cm$^{-3}$ and $V_C$=$1.7 \times 10^{20}$ cm$^{-3}$. From this, we estimate that there are $1.48 \times 10^9$ $V_{Si}$ in the longest 110 µm string. The actual defect densities are lower as most of the created defects anneal at room temperature[131,189].

### 5.2.4 Effect of Helium Ion Implantation

To create $V_{Si}$ in mechanical nanoresonators, we have employed helium ion broad-beam implantation protocol at room temperature with energy $E_I$=14 keV and ion fluence $\Phi$=$10^{12}$, $10^{13}$ and $10^{14}$ cm$^{-2}$ consecutively. Figure 5.15 shows the effect of helium ion implantation on the response and mechanical properties of strings. The frequencies of all modes and for all string lengths drop with fluence, but the effect is visible only for the highest fluence $\Phi$=$1 \times 10^{14}$ cm$^{-2}$.

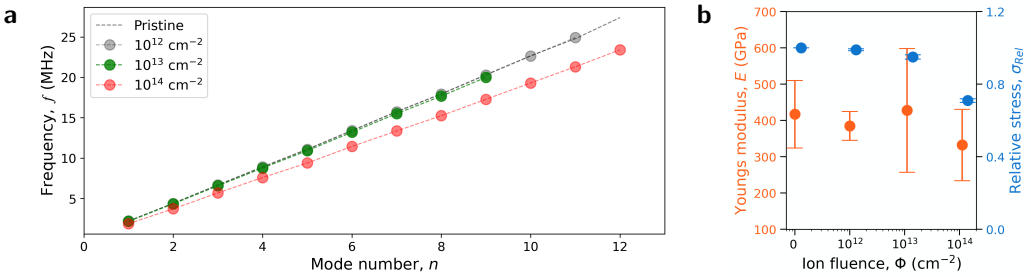


**Fig. 5.15: Effect of helium ion implantation.** (a) The plot shows a change in OOP mode frequencies for a 110 µm string after incremental implantation steps from $\Phi$=$1 \times 10^{12}$ cm$^{-2}$ to $1 \times 10^{14}$ cm$^{-2}$. (b) Young's modulus $E$ and relative stress $\sigma_{Rel}$ (with respect stress in strings without implantation) versus incremental ion fluences are plotted for for all string lengths and error bars indicate the standard deviation. Stress data are shifted for clarity.

After the implantation with $\Phi$=$1 \times 10^{12}$ cm$^{-2}$, the stress $\sigma$ remains the same as the pristine sample, indicating a negligible change in mechanical eigenfrequencies up to this fluence. With increasing fluence, however, $\sigma$ starts relaxing and finally reaches 532 MPa at $\Phi$=$1 \times 10^{14}$ cm$^{-2}$ for 110 µm string. On the other hand, Young's modulus $E$ stays constant within the error margins for all employed fluences. Our results are in agreement with the previous experimental[139,140,190] and theoretical work[141].

We find that $\sigma$ is proportional to the slope of $f(n)$ and can fit reliably with a few data points. However, $E$, corresponding to a small non-linear component of $f(n)$, can only be measured with lower uncertainties for higher modes. Therefore, $E$ is more sensitive to the uncertainties in frequencies, geometric, and material parameters than $\sigma$ (not shown here). Also, measured $E$ is based on the bending rigidity model, which assumes a thin isotropic string with a rectangular cross-section. Implantation creates more damage in the lower half of the strings (Figure 5.14b), and the elastic properties should not remain isotropic. However, as $E$ remains unaltered, it allows using the bending rigidity model to treat our analysis[188].

Implantation in the low dpa regime creates points defects such as vacancies, antisites, and interstitials. It has been shown that interstitials play an essential role in causing tensile strain[191]. In addition, helium atoms get trapped in $V_{Si}$ or $V_C$, crucial from the second implantation step, causing large internal stress. However, as our strings are already under tensile stress originating from growth and fabrication processes, deriving a direct correlation between stress relaxation and point defects is complex and out of the scope of this work. It has been concluded using Raman spectroscopy that deposition of helium on interstitial sites leads to internal stress without breaking of SiC bonds. These results from Raman spectroscopy also support the fact that stress changes, but as the bonds are not broken, the elastic properties remain unchanged[132].

$V_{Si}$ ensembles are created with helium in the fluence range $\Phi = 5 \times 10^{13}\,\mathrm{cm}^{-2}$ to $1 \times 10^{14}\,\mathrm{cm}^{-2}$[192]. Isolated optically active $V_{Si}$ are created at much lower fluence $\Phi{=}1 \times 10^{11}\,\mathrm{cm}^{-2}$, where changes in mechanical properties are negligible[108]. Therefore, helium ion implantation in the low-damage regime where isolated optically active $V_{Si}$ are created in 3C-SiC nanomechanical resonators does not alter the mechanical response significantly. Additionally, with the stress relaxation after ion implantation, tuning the resonators individually with local FIB writing tools such as HIM is possible. With HIM, resonance frequencies can be matched better than their linewidths or their resonant coupling can even be engineered.

In conclusion, we have shed light on how the mechanical response of the nanomechanical resonators in 3C-SiC alters after low-damage helium implantation. Our results show that the stress relaxes by 30% for the fluence $\Phi{=}1 \times 10^{14}\,\mathrm{cm}^{-2}$. As stress modifies in this regime, special attention must be given while designing devices such as MEMS and NEMS sensors. Young's modulus does not change significantly for all the implantation fluences, and the elastic properties of the strings are maintained. Stress and Young's modulus change are primarily related to defect types and their distribution, helium trapping at vacancies, point defects and their clusters, and volumetric swelling.

This chapter summarises the key results of my doctoral work. The first part consists of the integration of ensembles of G-centres in Si nanopillars and wafer-scale nanofabrication of G- and W-centres. To integrate G-centres in Si nanopillars, we have developed a fabrication protocol, including MACEtch, which does not create any optically active colour centres in the telecom O-band, and this is the most important achievement of this thesis.

In the second part, I have presented nanomechanical resonators in SiC to investigate the effect of helium implantation on their mechanical response. First, I showed preliminary results of PEC etching for bilayer 4H-SiC with the goal of producing nanoresonators in p-type 4H-SiC. Afterwards, the characterisation of 3C-SiC strings, followed by changes in stress and Young's modulus after helium implantation, is discussed. I will briefly summarise my doctoral thesis in the next and final chapter.

# Chapter 6

# Conclusion and Outlook

In conclusion, I investigated fabrication and characterisation of nanostructures for applications in quantum communication and sensing. On one side, I have demonstrated a pathway towards monolithic integration of quantum photonic integrated circuits by creating ensembles of telecom-photon emitters in silicon nanopillars. On the other hand, I have presented how the process of creating silicon vacancies, helium ion implantation in our case, affects the mechanical properties of high-quality doubly clamped 3C-SiC nanoresonators is presented.

In the first project, we fabricate silicon nanopillar arrays of varying diameters with a fabrication protocol employing standard electron beam lithography (EBL), but rather a relatively new wet anisotropic etching technique called metal-assisted chemical etching (MACEtch). The etch quality in terms of surface roughness and uniformity can be achieved by isolating each array using frames. From literature and experience, it has been concluded that fabricating smaller structures far apart demands more experimental optimisation. Nevertheless, we have successfully fabricated silicon nanopillars with 5 µm pitch which is crucial for QPIC.

The incentive to avoid lattice damage as a general consequence of standard reactive ion etching (RIE) led to the development of MACEtch for silicon etching. More importantly, the low-temperature photoluminescence (PL) measurements indicate the absence of any optically active centres in the telecom O-band post-fabrication for unimplanted pillars. Therefore, MACEtch allows defect-free, smooth, and uniform anisotropic etching at low cost, and it is possible to extend the technique to other materials on a wafer scale. The current research overview of MACEtch shows that it can be potentially used as a standard for low- to mid-level industrial and research applications.

Next, we create ensembles of G-centres in the nanopillars by carbon broad-beam implantation with a fluence of $2\times10^{14}$ cm$^{-2}$ at an energy of 250 keV corresponding to a projected range of 600 nm. A low-temperature PL shows a sharp zero phonon line (ZPL) at 1278 nm with a phonon sideband (PSB) at longer wavelengths, which is the optical fingerprint of G-centres. We estimate a Debye-Waller factor of 12% and measure 20% enhancement in the PL signal with 3.5 times narrower FWHM from the pillars compared to the bulk silicon due to the waveguiding effect. The goal of improving the spectroscopic properties by integrating G-centres in pillars is achieved.

In addition, we demonstrate a wafer-scale protocol to create individual G-centres and W-centres in silicon using broad-beam implantation through a lithographically patterned PMMA mask. In the following steps, we would like to fabricate photonic structures in silicon and create single telecom-photon emitters integrated into the nanostructures using a FIB protocol. It will contribute to reaching the goal of monolithic integration of silicon-based QPIC and will be a breakthrough in quantum photonics.

In the second project, focusing on quantum sensing, our work is inspired by the concept of hybrid spin-mechanical systems to measure magnetic fields with enhanced precision. The idea is to extend spin-based magnetometry based on silicon vacancies ($V_{Si}$) by coupling spin associated with $V_{Si}$ to mechanical resonators in 4H-SiC. To this end, we are developing a standard fabrication protocol for doubly clamped resonators in bi-layer 4H-SiC. We employ the photoelectrochemical etching (PEC) technique to underetch p-SiC. However, etching leads to porous structures with n-SiC and needs calibration experiments. The low current density during PEC is likely due to higher contact resistance from the backside of the sample. Improving the nickel back contact and cell configuration will solve the issues and is a work in progress.

In the interim, we focus on understanding the change in mechanical properties of nanomechanical resonators in 3C-SiC due to the creation of $V_{Si}$. Epitaxially grown 3C-SiC on Si leads to a stressed device layer, which results in high-Q ($\sim10^4$) mechanical resonators and is attributed to the damping dilution. Such a high-quality and, therefore, sensitive system is an ideal platform to study subtle changes in material properties after implantation.

First, 3C-SiC resonators are fabricated using standard semiconductor processing techniques, including EBL and RIE. Resonators are characterised to determine vibrational frequencies and quality factors using a Fabry-Pérot interferometer before and after implantation. Furthermore, we also measure higher modes for all string lengths. By fitting the data with the Euler-Bernoulli equation, we estimate the change in stress and Young's modulus after implantation.

Afterwards, we use helium ion implantation to create $V_{Si}$ in SiC because of features such as low damage, high resolution, and the possibility of extending it to a single-defect level using HIM. We have implanted helium in successive steps with fluence $\Phi$=1 $\times$ $10^{12}$ $cm^{-2}$, 1 $\times$ $10^{13}$ $cm^{-2}$, and 1 $\times$ $10^{14}$ $cm^{-2}$ at an energy $E_I$=14 keV corresponding to the projected range $R_P$ of 95 nm.

By fitting the Euler-Bernoulli beam equation to the data, we study changes in stress and Young's modulus with ion fluence. Generally, ion implantation leads to crystal damage in moderate to high dpa regimes. We observe no change in resonance frequencies and stress for the lowest fluence $\Phi$=1 $\times$ $10^{12}$ $cm^{-2}$ but record stress relaxation for higher fluences, which is attributed to volumetric swelling, helium trapping, and interstitial defects. Lowering quality factors is associated with increased dissipation losses. However, Young's modulus does not change significantly and stays within error margins. It must be noted that, in the low-damage implantation regime, where single or ensembles of $V_{Si}$ are created, this does not hamper the performance of SiC nanoresonators. Preserving mechanical properties after ion implantation, where single or small ensembles of point defects are created, is crucial for device applications in quantum technologies.

Finally, my doctoral research has contributed to taking a step towards the practical realisation of envisioned applications in quantum communication and sensing. For quantum communication, my work has contributed to making QPIC fully monolithic by integrating telecom photon emitters in photonic structures and their wafer-scale nanofabrication. Also, my research lays out a fabrication protocol that is especially suitable for photonics. In the case of quantum sensing, our work mainly gives a perspective on the change in mechanical properties of 3C-SiC resonators with helium ion implantation.

# Bibliography


[1] M. Polini et al., *Materials and devices for fundamental quantum science and quantum technologies*, arXiv:2201.09260 [cond-mat, physics:quant-ph], Jan. 2022.

[2] O. Van Deventer et al., 'Towards European standards for quantum technologies', EPJ Quantum Technology **9**, 33 (2022).

[3] L. C. Bassett et al., 'Quantum defects by design', Nanophotonics **8**, 1867–1888 (2019).

[4] J. S. Sidhu et al., 'Advances in space quantum communications', IET Quantum Communication **2**, 182–217 (2021).

[5] A. Acín et al., 'The quantum technologies roadmap: a European community view', New Journal of Physics **20**, 080201 (2018).

[6] W. P. Schleich et al., 'Quantum technology: from research to application', Applied Physics B **122**, 130 (2016).

[7] R. Horodecki et al., 'Quantum entanglement', Reviews of Modern Physics **81**, 865–942 (2009).

[8] S. Pirandola et al., 'Advances in quantum teleportation', Nature Photonics **9**, 641–652 (2015).

[9] S. L. Braunstein and H. J. Kimble, 'Teleportation of Continuous Quantum Variables', Physical Review Letters **80** (1998).

[10] C. H. Bennett et al., 'Teleporting an unknown quantum state via dual classical and Einstein-Podolsky-Rosen channels', Physical Review Letters **70**, 1895–1899 (1993).

[11] W. K. Wootters and W. H. Zurek, 'A single quantum cannot be cloned', Nature **299**, 802–803 (1982).

[12] J. S. Sidhu and P. Kok, *Quantum Fisher information for general spatial deformations of quantum emitters*, arXiv:1802.01601 [quant-ph], Feb. 2018.

[13]J. S. Sidhu and P. Kok, 'Quantum metrology of spatial deformation using arrays of classical and quantum light emitters', Physical Review A **95**, 063829 (2017).

[14]J. S. Sidhu and P. Kok, 'Geometric perspective on quantum parameter estimation', AVS Quantum Science **2**, 014701 (2020).

[15]J. S. Sidhu et al., 'Tight Bounds on the Simultaneous Estimation of Incompatible Parameters', Physical Review X **11**, 011028 (2021).

[16]J. Rubio et al., 'Quantum sensing networks for the estimation of linear functions', Journal of Physics A: Mathematical and Theoretical **53**, 344001 (2020).

[17]R. Jozsa et al., 'Quantum Clock Synchronization Based on Shared Prior Entanglement', Physical Review Letters **85**, 2010–2013 (2000).

[18]A. Peres and D. R. Terno, 'Optimal distinction between non-orthogonal quantum states', Journal of Physics A: Mathematical and General **31**, 7105–7111 (1998).

[19]J. S. Sidhu et al., 'Quantum Receiver for Phase-Shift Keying at the Single-Photon Level', PRX Quantum **2**, 010332 (2021).

[20]V. Scarani et al., 'The security of practical quantum key distribution', Reviews of Modern Physics **81**, 1301–1350 (2009).

[21]S. Pirandola et al., 'Advances in quantum cryptography', Advances in Optics and Photonics **12**, 1012 (2020).

[22]E. Knill and R. La, 'A scheme for ef®cient quantum computation with linear optics', **409** (2001).

[23]J. Wang et al., 'Multidimensional quantum entanglement with large-scale integrated optics', Science **360**, 285–291 (2018).

[24]W. Bogaerts et al., 'Programmable photonic circuits', Nature **586**, 207–216 (2020).

[25]A. Politi et al., 'Silica-on-Silicon Waveguide Quantum Circuits', Science **320**, 646–649 (2008).

[26]F. Najafi et al., 'On-chip detection of non-classical light by scalable integration of single-photon detectors', Nature Communications **6**, 5873 (2015).

[27]W. Pernice et al., 'High-speed and high-efficiency travelling wave single-photon detectors embedded in nanophotonic circuits', Nature Communications **3**, 1325 (2012).

[28]E. Pelucchi et al., 'The potential and global outlook of integrated photonics for quantum technologies', Nature Reviews Physics **4**, 194–208 (2021).

[29]J. Van Dijk et al., 'The electronic interface for quantum processors', Microprocessors and Microsystems **66**, 90–101 (2019).

[30]F. Flamini et al., 'Photonic quantum information processing: a review', Reports on Progress in Physics **82**, 016001 (2019).

[31]J. L. O'Brien, 'Optical Quantum Computing', Science **318**, 1567–1570 (2007).

[32]J. L. O'Brien et al., 'Photonic quantum technologies', Nature Photonics **3**, 687–695 (2009).

[33]S. Gyger et al., 'Reconfigurable photonics with on-chip single-photon detectors', Nature Communications **12**, 1408 (2021).

[34]Y. Tian et al., 'Experimental demonstration of a reconfigurable electro-optic directed logic circuit using cascaded carrier-injection micro-ring resonators', Scientific Reports **7**, 6410 (2017).

[35]H. Lee et al., 'Ultra-low-loss optical delay line on a silicon chip', Nature Communications **3**, 867 (2012).

[36]A. Orieux and E. Diamanti, 'Recent advances on integrated quantum communications', Journal of Optics **18**, 083002 (2016).

[37]M. Hollenbach et al., 'Engineering telecom single-photon emitters in silicon for scalable quantum photonics', Optics Express **28**, 26111 (2020).

[38]W. Redjem et al., 'Single artificial atoms in silicon emitting at telecom wavelengths', Nature Electronics **3**, 738–743 (2020).

[39]A. Durand et al., 'Broad Diversity of Near-Infrared Single-Photon Emitters in Silicon', Physical Review Letters **126**, 083602 (2021).

[40]M. Hollenbach et al., 'Metal-assisted chemically etched silicon nanopillars hosting telecom photon emitters', Journal of Applied Physics **132**, 033101 (2022).

[41]M. Hollenbach et al., 'Wafer-scale nanofabrication of telecom single-photon emitters in silicon', Nature Communications **13**, 7683 (2022).

[42]D. B. Higginbottom et al., 'Optical observation of single spins in silicon', Nature **607**, 266–270 (2022).

[43]L. Weiss et al., 'Erbium dopants in nanophotonic silicon waveguides', Optica **8**, 40 (2021).

[44]Y. Baron et al., 'Detection of Single W-Centers in Silicon', ACS Photonics **9**, 2337–2345 (2022).

[45]N. Aslam et al., 'Quantum sensors for biomedical applications', Nature Reviews Physics **5**, 157–169 (2023).

[46]C. A. Hart et al., 'N - V –Diamond Magnetic Microscopy Using a Double Quantum 4-Ramsey Protocol', Physical Review Applied **15**, 044020 (2021).

[47]B. Yang et al., 'Vector Electrometry in a Wide-Gap-Semiconductor Device Using a Spin-Ensemble Quantum Sensor', Physical Review Applied **14**, 044049 (2020).

[48]D. B. Bucher et al., 'Quantum diamond spectrometer for nanoscale NMR and ESR spectroscopy', Nature Protocols **14**, 2707–2747 (2019).

[49]C. L. Degen et al., 'Quantum sensing', Reviews of Modern Physics **89**, 035002 (2017).

[50]E. Verhagen et al., 'Quantum-coherent coupling of a mechanical oscillator to an optical cavity mode', Nature **482**, 63–67 (2012).

[51]J. Chan et al., 'Laser cooling of a nanomechanical oscillator into its quantum ground state', Nature **478**, 89–92 (2011).

[52]S. Barzanjeh et al., 'Stationary entangled radiation from micromechanical motion', Nature **570**, 480–483 (2019).

[53]J.-M. Pirkkalainen et al., 'Squeezing of Quantum Noise of Motion in a Micromechanical Resonator', Physical Review Letters **115**, 243601 (2015).

[54]E. E. Wollman et al., 'Quantum squeezing of motion in a mechanical resonator', Science **349**, 952–955 (2015).

[55]B. Rogers et al., 'Hybrid optomechanics for Quantum Technologies', Quantum Measurements and Quantum Metrology **2**, `10.2478/qmetro-2014-0002` (2014).

[56]G. Kurizki et al., 'Quantum technologies with hybrid systems', Proceedings of the National Academy of Sciences **112**, 3866–3873 (2015).

[57]A. V. Poshakinskiy and G. V. Astakhov, 'Optically detected spin-mechanical resonance in silicon carbide membranes', Physical Review B **100**, 094104 (2019).

[58]M. Aspelmeyer et al., eds., *Cavity Optomechanics: Nano- and Micromechanical Resonators Interacting with Light* (Springer Berlin Heidelberg, Berlin, Heidelberg, 2014).

[59]N. Daniilidis et al., 'Quantum information processing with trapped electrons and superconducting electronics', New Journal of Physics **15**, 073017 (2013).

[60]Z.-L. Xiang et al., 'Hybrid quantum circuits: Superconducting circuits interacting with other quantum systems', Reviews of Modern Physics **85**, 623–653 (2013).

[61] J. J. Morton and B. W. Lovett, 'Hybrid Solid-State Qubits: The Powerful Role of Electron Spins', Annual Review of Condensed Matter Physics **2**, 189–212 (2011).

[62] M. Wallquist et al., 'Hybrid quantum devices and quantum engineering', Physica Scripta **T137**, 014001 (2009).

[63] S. M. Sze et al., *Semiconductor devices, physics and technology*, 3rd edition (Wiley, 2012).

[64] N. S. Jagtap, 'Fabrication and Characterization of String Resonator Structures in Silicon Carbide for Hybrid Spin-Mechanical Systems', Master thesis at TUD Dresden University of Technology (2019).

[65] A. Rockett, *The materials science of semiconductors* (Springer, 2008).

[66] J. Patterson and B. Bailey, *Solid-state physics, introduction to the theory*, Second edition (Springer, 2010).

[67] D. Kumar and M. Johari, 'Characteristics of silicon crystal, its covalent bonding and their structure, electrical properties, uses', in (2020), p. 040037.

[68] M. Khoury and M. Abbarchi, 'A bright future for silicon in quantum technologies', Journal of Applied Physics **131**, 200901 (2022).

[69] R. C. Newman, 'Defects in silicon', Reports on Progress in Physics **45**, 1163–1210 (1982).

[70] K. Fujii et al., 'Realization of the kilogram by the XRCD method', Metrologia **53**, A19–A45 (2016).

[71] K. M. Itoh and H. Watanabe, 'Isotope engineering of silicon and diamond for quantum computing and sensing applications', MRS Communications **4**, 143–157 (2014).

[72] G. Fisher et al., 'Silicon Crystal Growth and Wafer Technologies', Proceedings of the IEEE **100**, 1454–1474 (2012).

[73] F. Shimura, *Semiconductor silicon crystal technology* (Academic Press, San Diego, 1989).

[74] G. Davies, 'The optical properties of luminescence centres in silicon', Physics Reports **176**, 83–188 (1989).

[75] M. Hollenbach, 'Ion-induced telecom single-photon emitters in silicon for scalable quantum photonics',

[76] K. Thonke et al., 'New model of the irradiation-induced 0.97-eV ( G ) line in silicon: A C S − Si * complex', Physical Review B **24**, 5874–5886 (1981).

[77] K. O'Donnell et al., 'Origin of the 0.97 eV luminescence in irradiated silicon', Physica B+C **116**, 258–263 (1983).

[78]L. W. Song et al., 'Bistable interstitial-carbon–substitutional-carbon pair in silicon', Physical Review B **42**, 5765–5783 (1990).

[79]D. D. Berhanuddin et al., 'Co-Implantation of Carbon and Protons: An Integrated Silicon Device Technology Compatible Method to Generate the Lasing G-Center', Advanced Functional Materials **22**, 2709–2712 (2012).

[80]D. Timerkaeva et al., 'Structural, electronic, and optical properties of the C-C complex in bulk silicon from first principles', Journal of Applied Physics **123**, 161421 (2018).

[81]C. Chartrand et al., 'Highly enriched Si 28 reveals remarkable optical linewidths and fine structure for well-known damage centers', Physical Review B **98**, 195201 (2018).

[82]C. Beaufils et al., 'Optical properties of an ensemble of G-centers in silicon', Physical Review B **97**, 035303 (2018).

[83]P. Udvarhelyi et al., 'Identification of a Telecom Wavelength Single Photon Emitter in Silicon', Physical Review Letters **127**, 196402 (2021).

[84]C. Kurtsiefer et al., 'Stable Solid-State Source of Single Photons', Physical Review Letters **85** (2000).

[85]I. Aharonovich et al., 'Photophysics of chromium-related diamond single-photon emitters', Physical Review A **81**, 043813 (2010).

[86]E. Neu et al., 'Single photon emission from silicon-vacancy colour centres in chemical vapour deposition nano-diamonds on iridium', New Journal of Physics **13**, 025012 (2011).

[87]F. Fuchs et al., 'Engineering near-infrared single-photon emitters with optically active spins in ultrapure silicon carbide', Nature Communications **6**, 7578 (2015).

[88]S. Tian, 'Monte Carlo Simulation of Ion Implantation in Crystalline SiC With Arbitrary Polytypes', IEEE Transactions on Electron Devices **55**, 1991–1996 (2008).

[89]H. Morkoç et al., 'Large-band-gap SiC, III-V nitride, and II-VI ZnSe-based semiconductor device technologies', Journal of Applied Physics **76**, 1363–1398 (1994).

[90]Y. S. Klaß, 'High Q Nanomechanical Resonators Fabricated from Crystalline Silicon Carbide', PhD Thesis at Technical University of Munich (2022).

[91]D. Simin, 'Quantum Sensing with Highly Coherent Spin Centers in Silicon Carbide', PhD thesis at Julius-Maximilians-Universität Würzburg, 118 (2017).

[92]F. Zhao et al., 'Photoelectrochemical etching to fabricate single-crystal SiC MEMS for harsh environments', Materials Letters **65**, 409–412 (2011).

[93]M. M. Islam et al., 'Single-Crystal SiC Resonators by Photoelectrochemical Etching', Materials Science Forum **717-720**, 529–532 (2012).

[94]R. M. Hazen et al., 'Carbon Mineralogy and Crystal Chemistry', Reviews in Mineralogy and Geochemistry **75**, 7–46 (2013).

[95]W. Ching et al., 'The electronic structure and spectroscopic properties of 3C, 2H, 4H, 6H, 15R and 21R polymorphs of SiC', Materials Science and Engineering: A **422**, 147–156 (2006).

[96]H. Matsunami, 'Technological Breakthroughs in Growth Control of Silicon Carbide for High Power Electronic Devices', Japanese Journal of Applied Physics **43**, 6835–6847 (2004).

[97]A. L. Falk et al., 'Polytype control of spin qubits in silicon carbide', Nature Communications **4**, 1819 (2013).

[98]F. Fuchs, 'Optical spectroscopy on silicon vacancy defects in silicon carbide', PhD thesis at Julius-Maximilians-Universität Würzburg, 115 (2015).

[99]A. Gali, 'Excitation Properties of Silicon Vacancy in Silicon Carbide', Materials Science Forum **717-720**, 255–258 (2012).

[100]H. Kraus et al., 'Room-temperature quantum microwave emitters based on spin defects in silicon carbide', Nature Physics **10**, 157–162 (2014).

[101]N. Mizuochi et al., 'Continuous-wave and pulsed EPR study of the negatively charged silicon vacancy with S = 3 2 and C 3 v symmetry in n -type 4 H − SiC', Physical Review B **66**, 235202 (2002).

[102]Ö. O. Soykal et al., 'Silicon vacancy center in 4 H -SiC: Electronic structure and spin-photon interfaces', Physical Review B **93**, 081207 (2016).

[103]P. G. Baranov et al., 'Silicon vacancy in SiC as a promising quantum system for single-defect and single-photon spectroscopy', Physical Review B **83**, 125203 (2011).

[104]M. Widmann et al., 'Coherent control of single spins in silicon carbide at room temperature', Nature Materials **14**, 164–168 (2015).

[105]R. Nagy et al., 'Quantum Properties of Dichroic Silicon Vacancies in Silicon Carbide', Physical Review Applied **9**, 034022 (2018).

[106]J. Wang et al., 'Efficient Generation of an Array of Single Silicon-Vacancy Defects in Silicon Carbide', Physical Review Applied **7**, 064021 (2017).

[107]J.-F. Wang et al., 'On-Demand Generation of Single Silicon Vacancy Defects in Silicon Carbide', ACS Photonics **6**, 1736–1743 (2019).

[108]C. Babin et al., 'Fabrication and nanophotonic waveguide integration of silicon carbide colour centres with preserved spin-optical coherence', Nature Materials **21**, 67–73 (2022).

[109]Y.-C. Chen et al., 'Laser Writing of Scalable Single Color Centers in Silicon Carbide', Nano Letters **19**, 2377–2383 (2019).

[110]J. Wang et al., 'Scalable Fabrication of Single Silicon Vacancy Defect Arrays in Silicon Carbide Using Focused Ion Beam', ACS Photonics **4**, 1054–1059 (2017).

[111]S. P. Pavunny et al., 'Arrays of Si vacancies in 4H-SiC produced by focused Li ion beam implantation', Scientific Reports **11**, 3561 (2021).

[112]Z.-X. He et al., 'Maskless Generation of Single Silicon Vacancy Arrays in Silicon Carbide by a Focused $He^+$ Ion Beam', ACS Photonics **10 (7)**, 2234–2240 (2022).

[113]D. Riedel et al., 'Resonant Addressing and Manipulation of Silicon Vacancy Qubits in Silicon Carbide', Physical Review Letters **109**, 226402 (2012).

[114]M. Fischer et al., 'Highly Efficient Optical Pumping of Spin Defects in Silicon Carbide for Stimulated Microwave Emission', Physical Review Applied **9**, 054006 (2018).

[115]S. Schmid et al., *Fundamentals of Nanomechanical Resonators* (Springer International Publishing, Cham, 2016).

[116]M. Bückle et al., 'Universal Length Dependence of Tensile Stress in Nanomechanical String Resonators', Physical Review Applied **15**, 034063 (2021).

[117]A. N. Cleland, *Foundations of Nanomechanics*, Advanced Texts in Physics (Springer Berlin Heidelberg, Berlin, Heidelberg, 2003).

[118]Q. P. Unterreithmeier et al., 'Damping of Nanomechanical Resonators', Physical Review Letters **105**, 027205 (2010).

[119]P.-L. Yu et al., 'Control of Material Damping in High- Q Membrane Microresonators', Physical Review Letters **108**, 083603 (2012).

[120]L. G. Villanueva and S. Schmid, 'Evidence of Surface Loss as Ubiquitous Limiting Damping Mechanism in SiN Micro- and Nanomechanical Resonators', Physical Review Letters **113**, 227201 (2014).

[121]A. Bachtold et al., 'Mesoscopic physics of nanomechanical systems', Reviews of Modern Physics **94**, 045005 (2022).

[122]S. Volz et al., 'Nanophononics: state of the art and perspectives', The European Physical Journal B **89**, 15 (2016).

[123]Z. Li and R. C. Bradt, 'The single-crystal elastic constants of cubic (3C) SiC to 1000 C', Journal of Materials Science **22**, 2557–2559 (1987).

[124]Y. S. Klaß et al., 'Determining Young's modulus via the eigenmode spectrum of a nanomechanical string resonator', Applied Physics Letters **121**, 083501 (2022).

[125]V. Kulikovsky et al., 'Hardness and elastic modulus of amorphous and nanocrystalline SiC and Si films', Surface and Coatings Technology **202**, 1738–1745 (2008).

[126]K. Babaei Gavan et al., 'Size-dependent effective Young's modulus of silicon nitride cantilevers', Applied Physics Letters **94**, 233108 (2009).

[127]B. Hähnlein et al., 'Mechanical Properties and Residual Stress of Thin 3C-SiC(111) Films Determined Using MEMS Structures', Materials Science Forum **778-780**, 444–448 (2014).

[128]B. Hähnlein et al., 'Mechanical Properties and Residual Stress of Thin 3C-SiC(100) Films Determined Using MEMS Structures', Materials Science Forum **821-823**, 281–284 (2015).

[129]K. Nakata et al., 'Damage structure obtained by cross-sectional observation in silicon carbide irradiated with helium ions', Journal of Nuclear Materials **179-181**, 403–406 (1991).

[130]K. Hojou et al., 'In situ EELS and TEM observation of silicon carbide irradiated with helium ions at low temperature and successively annealed', Nuclear Instruments and Methods in Physics Research Section B: Beam Interactions with Materials and Atoms **116**, 382–388 (1996).

[131]W. Jiang et al., 'Accumulation and recovery of irradiation damage in He implanted a-SiC', Journal of Nuclear Materials (1998).

[132]H. Hobert et al., 'He+ beam induced damage of silicon carbide studied by vibrational spectroscopy', Nuclear Instruments and Methods in Physics Research Section B: Beam Interactions with Materials and Atoms **129**, 244–249 (1997).

[133]E. Oliviero et al., 'Helium implantation defects in SiC studied by thermal helium desorption spectrometry', Nuclear Instruments and Methods in Physics Research Section B: Beam Interactions with Materials and Atoms **186**, 223–228 (2002).

[134]C. Zhang et al., 'Evolution of defects in silicon carbide implanted with helium ions', Nuclear Instruments and Methods in Physics Research Section B: Beam Interactions with Materials and Atoms **326**, 345–350 (2014).

[135]H. Zang et al., 'Vacancy effects on the formation of He and Kr cavities in 3C-SiC irradiated and annealed at elevated temperatures', Nuclear Instruments and Methods in Physics Research Section B: Beam Interactions with Materials and Atoms **389-390**, 40–47 (2016).

[136]J. Sun et al., 'The stability of vacancy clusters and their effect on helium behaviors in 3C-SiC', Journal of Nuclear Materials **503**, 271–278 (2018).

[137]S. Yang et al., 'Electron energy-loss spectroscopic evaluation of depth-dependent swelling of $He^+$ ion-irradiated 4H-SiC correlated with defect type', Journal of Applied Physics **127**, 175106 (2020).

[138]B. Li et al., 'Irradiation-induced microstructure damage in He-irradiated 3C-SiC at 1000℃', Journal of the European Ceramic Society **40**, 1014–1022 (2020).

[139]S. Nogami and A. Hasegawa, 'Indentation Properties of Silicon Carbide after Neutron Irradiation and Helium Implantation', IOP Conference Series: Materials Science and Engineering **18**, 162007 (2011).

[140]J. F. Barbot et al., 'Effects of Helium Implantation on the Mechanical Properties of 4H-SiC', Materials Science Forum **645-648**, 721–724 (2010).

[141]J. Xi et al., 'The role of point defects in the swelling and elastic modulus of irradiated cubic silicon carbide', Nuclear Instruments and Methods in Physics Research Section B: Beam Interactions with Materials and Atoms **356-357**, 62–68 (2015).

[142]D. Dimova-Malinovska et al., 'Preparation of thin porous silicon layers by stain etching', Thin Solid Films **297**, 9–12 (1997).

[143]X. Li and P. W. Bohn, 'Metal-assisted chemical etching in $HF/H_2O_2$ produces porous silicon', Applied Physics Letters **77**, 2572–2574 (2000).

[144]X. Li, 'Metal assisted chemical etching for high aspect ratio nanostructures: A review of characteristics and applications in photovoltaics', Current Opinion in Solid State and Materials Science **16**, 71–81 (2012).

[145]H. Li and C. Xie, 'Fabrication of Ultra-High Aspect Ratio (>420:1) $Al_2O_3$ Nanotube Arrays by Sidewall TransferMetal Assistant Chemical Etching', Micromachines **11**, 378 (2020).

[146]L. Romano et al., 'Metal assisted chemical etching of silicon in the gas phase: a nanofabrication platform for X-ray optics', Nanoscale Horizons **5**, 869–879 (2020).

[147]H. Han et al., 'Metal-assisted chemical etching of silicon and nanotechnology applications', Nano Today **9**, 271–304 (2014).

[148]L. Romano, 'Editorial for the Special Issue on Micro- and Nano-Fabrication by Metal Assisted Chemical Etching', Micromachines **11**, 988 (2020).

[149]Z. Huang et al., 'Metal-Assisted Chemical Etching of Silicon: A Review: In memory of Prof. Ulrich Gösele', Advanced Materials **23**, 285–308 (2011).

[150]Y. Qian et al., 'Heterogeneous optoelectronic characteristics of si micropillar arrays fabricated by metal-assisted chemical etching', Scientific Reports **10** (2020).

[151]O. Hildreth and C. P. Wong, 'Nano-metal-Assisted Chemical Etching for Fabricating Semiconductor and Optoelectronic Devices', in *Materials for Advanced Packaging*, edited by D. Lu and C. Wong (Springer International Publishing, Cham, 2017), pp. 879–922.

[152]M. Zahedinejad et al., 'Deep and vertical silicon bulk micromachining using metal assisted chemical etching', Journal of Micromechanics and Microengineering **23**, 055015 (2013).

[153]P. Lova and C. Soci, 'Black GaAs: Gold-Assisted Chemical Etching for Light Trapping and Photon Recycling', Micromachines **11**, 573 (2020).

[154]L. Romano and M. Stampanoni, 'Microfabrication of X-ray Optics by Metal Assisted Chemical Etching: A Review', Micromachines **11**, 589 (2020).

[155]R. Akan et al., 'Metal-Assisted Chemical Etching and Electroless Deposition for Fabrication of Hard X-ray Pd/Si Zone Plates', Micromachines **11**, 301 (2020).

[156]C. Chang and A. Sakdinawat, 'Ultra-high aspect ratio high-resolution nanofabrication for hard X-ray diffractive optics', Nature Communications **5**, 4243 (2014).

[157]J. Kim et al., 'Au/Ag Bilayered Metal Mesh as a Si Etching Catalyst for Controlled Fabrication of Si Nanowires', ACS Nano **5**, 3222–3229 (2011).

[158]Y. Qi et al., 'Electron transport characteristics of silicon nanowires by metal-assisted chemical etching', AIP Advances **4**, 031307 (2014).

[159]K. Rajkumar et al., 'Engineering Silicon to Porous Silicon and Silicon Nanowires by Metal-Assisted Chemical Etching: Role of Ag Size and Electron-Scavenging Rate on Morphology Control and Mechanism', ACS Omega **2**, 4540–4547 (2017).

[160]Z. Huang et al., 'Ordered Arrays of Vertically Aligned [110] Silicon Nanowires by Suppressing the Crystallographically Preferred Etching Directions', Nano Letters **9**, 2519–2525 (2009).

[161]M. Kismann et al., 'Ordered arrays of Si nanopillars with alternating diameters fabricated by nanosphere lithography and metal-assisted chemical etching', Materials Science in Semiconductor Processing **128**, 105746 (2021).

[162]O. J. Hildreth et al., 'Effect of Catalyst Shape and Etchant Composition on Etching Direction in Metal-Assisted Chemical Etching of Silicon to Fabricate 3D Nanostructures', ACS Nano **3**, 4033–4042 (2009).

[163]K. Rykaczewski et al., 'Guided Three-Dimensional Catalyst Folding during Metal-Assisted Chemical Etching of Silicon', Nano Letters **11**, 2369–2374 (2011).

[164]J. Weber and M. Singh, 'New method to determine the carbon concentration in silicon', Applied Physics Letters **49**, 1617–1619 (1986).

[165]A. Henry et al., 'Photoluminescence characterization of plasma exposed silicon surfaces', Journal of Applied Physics **70**, 5597–5603 (1991).

[166]I. A. Buyanova et al., 'Photoluminescence of defects induced in silicon by SF6/O2 reactive-ion etching', Journal of Applied Physics **78**, 3348–3352 (1995).

[167]V. Siklitsky, *SiC - Silicon Carbide*, `http://www.ioffe.ru/SVA/NSM/Semicond/SiC/index.html`, (accessed: 30.11.2023).

[168]J. S. Shor et al., 'Dopant-selective etch stops in 6H and 3C SiC', Journal of Applied Physics **81**, 1546–1551 (1997).

[169]D. van Dorp and J. Kelly, 'Photoelectrochemistry of 4H–SiC in KOH solutions', Journal of Electroanalytical Chemistry **599**, 260–266 (2007).

[170]D. H. v. Dorp et al., 'Anodic etching of SiC in alkaline solutions', Journal of Micromechanics and Microengineering **17**, S50–S55 (2007).

[171]J. Suda et al., 'Electrostatic-Actuated Suspended Ribbon Structure Fabricated in Single-Crystalline SiC by Selective Photoelectrochemical Etching', Japanese Journal of Applied Physics **48**, 111101 (2009).

[172]M. A. Fraga et al., 'Silicon Carbide in Microsystem Technology — Thin Film Versus Bulk Material', in *Advanced Silicon Carbide Devices and Processing*, edited by S. E. Saddow and F. La Via (InTech, Sept. 2015).

[173]P. A. Kohl and F. W. Ostermayer, 'Photoelectrochemical Methods for III-V Compound Semiconductor Device Processing', 23.

[174]J. S. Shor et al., 'Photoelectrochemical conductivity selective etch stops for SiC', Applied Physics Letters **60**, 1001–1003 (1992).

[175] J. S. Shor et al., 'Photoelectrochemical Etching and Dopant Selective Etch-Stops in SiC', in *Amorphous and Crystalline Silicon Carbide IV*, Vol. 71, edited by H. K. V. Lotsch et al., Series Title: Springer Proceedings in Physics (Springer Berlin Heidelberg, Berlin, Heidelberg, 1992), pp. 356–361.

[176] J. S. Shor and A. D. Kurtz, 'Method for etching of silicon carbide semiconductor using selective etching of different conductivity types', 15 (2000).

[177] Y. Shishkin et al., 'Photoelectrochemical etching of n-type 4H silicon carbide', Journal of Applied Physics **96**, 2311–2322 (2004).

[178] J.-H. Tan et al., 'Fabrication of uniform 4H-SiC mesopores by pulsed electrochemical etching', Nanoscale Research Letters **9**, 570 (2014).

[179] D. Zhuang and J. Edgar, 'Wet etching of GaN, AlN, and SiC: a review', Materials Science and Engineering: R: Reports **48**, 1–46 (2005).

[180] J. L. Weyher et al., 'Defect-selective etching of SiC', physica status solidi (a) **202**, 578–583 (2005).

[181] P. M. Sarro, 'Silicon carbide as a new MEMS technology', Sensors and Actuators A: Physical **82**, 210–218 (2000).

[182] A. P. Magyar et al., 'High quality SiC microdisk resonators fabricated from monolithic epilayer wafers', Applied Physics Letters **104**, 051109 (2014).

[183] S. Whiteley et al., 'Dopant Selective Photoelectrochemical Etching of SiC', Journal of The Electrochemical Society **170**, 036508 (2023).

[184] G. Hlawacek and A. Gölzhäuser, eds., *Helium Ion Microscopy*, NanoScience and Technology (Springer International Publishing, Cham, 2016).

[185] F. I. Allen, 'A review of defect engineering, ion implantation, and nanofabrication using the helium ion microscope', Beilstein Journal of Nanotechnology **12**, 633–664 (2021).

[186] Y. Zhang et al., 'Ultralow-loss silicon waveguide crossing using Bloch modes in index-engineered cascaded multimode-interference couplers', Optics Letters **38**, 3608 (2013).

[187] J. S. Shor and A. D. Kurtz, 'Photoelectrochemical Etching of 6H-SiC', Journal of The Electrochemical Society **141**, 778–781 (1994).

[188] P. Bredol et al., *Effect of Helium Ion Implantation on 3C-SiC Nanomechanical String Resonators*, arXiv:2405.02035 [cond-mat], May 2024.

[189] M. G. Grimaldi et al., 'Amorphization and defect recombination in ion implanted silicon carbide', Journal of Applied Physics **81**, 7181–7185 (1997).

[190] D. Sun et al., 'Interaction between helium and intrinsic point defects in 3C-SiC single crystal', Journal of Applied Physics **121**, 225111 (2017).

[191]A. Debelle et al., 'Characterization and modelling of the ion-irradiation induced disorder in 6H-SiC and 3C-SiC single crystals', Journal of Physics D: Applied Physics **43**, 455408 (2010).

[192]M. Hollenbach et al., 'Ultralong-term high-density data storage with atomic defects in SiC', Adv. Funct. Mater. 2024, 2313413 (2024).

# Acknowledgements

First, I want to express my gratitude to Prof. Dr. Artur Erbe and PD Dr. Georgy Astakhov for allowing me to work with them. Thanks, Georgy and Artur, for your pragmatism and scientific freedom you gave me. Without you, my PhD journey would have been totally different. Thank you very much.

I thank my mentors and supervisors, Dr. Ciarán Fowley, Prof. Dr. Artur Erbe, PD Dr. Georgy Astakhov, and Prof. Manfred Helm, for their invaluable scientific counselling. I also thank Prof. Dr. Eva Weig for reviewing my thesis.

I want to thank our expert technicians, Bernd Scheumann, Gabriele Schnabel, Tommy Schönherr, Claudia Neisser, Jens Zscharschuch, and Holger Lange, for always being supportive in cases of technical intricacies with the setups and processes. Thank you very much, Gabi, for training me on cleanroom processing. I express my gratitude to PD. Dr. Peter Zahn for always helping with the complex administration and things related to PhD life.

I am thankful to our collaborators, Prof. Dr. Eva Weig, Dr. Yannick Klaß, Dr. Philipp Bredol, and Felix David, for exciting discussions, project coordination, and for allowing me to work in their labs. Thanks, Yannick and Philipp, for helping with the measurements at TUM labs and data analysis.

I thank Mitisha and Silvan for their help with SRIM and for understanding the simulation results. Thanks, Prosun, for your support with the Python code.

I would like to thank my friends who have always been helpful and kept my motivation strong: Maria, Andrey, Alex, Filip, Ciarán, Simon, Serhii, Željko, Astrid, Michael, Andrey, Yonder, Saif, Oliver, Anna, João, Kalliopi, Pavel, Xiaoxiao, Justin, and Patrick. Alex and Filip, I will never forget the great times with you at HZDR and outside.

I am grateful to my students Juan, Alžbeta, Deniz, Gabriel, and Susan. I had interesting discussions with you all, and I learned so much from you.

No matter where you are, your best friends are always there for you! Thanks to XP, Pankaj, Aniket, who always believed in me and made me believe in myself!

At last, I thank my lovely parents, Kanchan and Shamrao, and sisters, Neha and Neelam, who have always supported and motivated me along my journey through life! Special appreciation goes to my wife, Sukriti, for her support during thesis writing and towards the end of my PhD. I could not have possibly come so far without them!

# Appendix A

# Fabrication Protocols

## A.1 3C-SiC Mechanical Nanoresonators

**Table A.1: Fabrication protocol for 3C-SiC nanoresonators**

| Process step | Equipment | Details |
|---|---|---|
| Cleaning | Ultrasonic bath, acetone | power=5 for 5 min |
| | IPA | dip in IPA |
| | $N_2$ stream | blow drying |
| Spin coating | Spin coater, 950K PMMA A6 | 800 rpm, 5 s, ramp up 800 rpm $s^{-1}$ |
| | | 5000 rpm, 30 s, ramp up 2500 rpm $s^{-1}$ |
| | | 100 rpm, 2 s, ramp down 2500 rpm $s^{-1}$ |
| | Hotplate | at 180 °C for 90 s |
| EBL | Raith 150TWO | acceleration voltage=10 kV |
| | | aperture=30 µm |
| | | base dose=100 µC $cm^{-2}$ |
| Development | MIBK:IPA 1:3 | dip for 50 s |
| | IPA | 90 s |
| | $N_2$ stream | blow drying |
| Evaporation | Leybold LAB500 | 30 nm Cr at 1.5 Å $s^{-1}$ |
| | (thermal) | base pressure $\sim 10^{-6}$ mbar (check) |
| Lift-off | Ultrasonic bath, acetone | power=1 for 5 min |
| | IPA | dip in IPA |
| | $N_2$ stream | blow drying |
| Releasing resonators[90] | ICP-RIE | anisotropic etching of 3C-SiC and Si |
| | ICP-RIE | Isotropic etching of Si |
| | Cr etchant | dip for 40 s |

## A.2 Si Photonic Nanopillars

**Table A.2: Fabrication protocol for Si nanopillars**

| Process step | Equipment | Details |
|---|---|---|
| Piranha cleaning | 96% $H_2SO_4$:31% $H_2O_2$=3:1<br>DI water<br>$N_2$ stream | dip for 15 min<br>dip in 2 consecutive baths<br>blow drying |
| Oxide removal | 0.5% HF solution | dip for 2 min |
| Spin coating | UV Spin Coater LabSpin6<br>ma-N 2410<br><br>Hotplate | ramp up in 1 s to 3500 rpm<br>spin time=45 s<br>resist thickness=1 µm<br>at 90 °C for 150 s |
| EBL | Raith 150TWO | acceleration voltage=20 kV<br>aperture=20 µm<br>base dose=130 µC cm$^{-2}$ |
| Development | ma-D 525<br>DI water<br>$N_2$ stream | dip for 3 min<br>dip for 1 min<br>blow drying |
| Oxide removal | 0.5% HF solution | dip for 2 min |
| Evaporation | Creavac CREAMET 600 (thermal) | 10 nm Au at 3 Å s$^{-1}$<br>base pressure=$10^{-8}$ mbar |
| MACEtch | solution of 31% $H_2O_2$, 40% HF and DI water<br><br>MACEtch solution<br><br>DI water<br>$N_2$ stream | 100 mL DI water<br>add 4.5 mL $H_2O_2$, wait 5 min<br>add 25 mL HF, wait 5 min<br>5 min dip<br>etch rate=240 nm min$^{-1}$<br>dip in 2 consecutive baths<br>blow drying |
| Lift-off | Ultrasonic bath, acetone<br>IPA<br>$N_2$ stream | lowest intensity, 5 min<br>dip in IPA<br>blow drying |

## A.3 4H-SiC Mechanical Nanoresonators

**Table A.3: Fabrication protocol for 4H-SiC nanoresonators**

| Process step | Equipment | Details |
|---|---|---|
| Cleaning | Ultrasonic bath, acetone<br>IPA<br>$N_2$ stream | power=3 for 5 min<br>dip in IPA<br>blow drying |
| Spin coating | Hotplate<br>Spin coater, EL11<br>Hotplate<br>Spin coater, 950K PMMA A4<br>Hotplate | at 150 °C for 5 min<br>4000 rpm, thickness=270 nm<br>at 150 °C for 5 min<br>4000 rpm, thickness=125 nm<br>at 150 °C for 5 min |
| EBL | Raith 150TWO | acceleration voltage=10 kV<br>aperture=30 µm<br>base dose=100 $\mu C\,cm^{-2}$ |
| Development | MIBK:IPA 1:3<br>IPA<br>$N_2$ stream | dip for 30 s<br>90 s<br>blow drying |
| Evaporation | Creavac CREAMET 600<br>(e-beam) | 50 nm Ni at 3 $Å\,s^{-1}$<br>base pressure = $10^{-8}$ mbar |
| Lift-off | Ultrasonic bath, acetone<br>IPA<br>$N_2$ stream | power=1 for 5 min<br>dip in IPA<br>blow drying |
| Anisotropic etching | ICP-RIE | $SF_6$=40 SCCM, $O_2$=10 SCCM<br>P=2.0 Pa, ICP Power=400 W<br>RF Power=75 W, time=2 min<br>etch rate $\sim$ 350 $nm\,min^{-1}$ |
| Removing Ni by Aqua regia | $HNO_3$:HCl=1:3 at 80 °C<br>DI water<br>$N_2$ stream | dip for 10 min<br>dip for 30 s<br>blow drying |
| Evaporation (back contact) | Creavac CREAMET 600<br>(e-beam) | 100 nm Ni at 3 $Å\,s^{-1}$<br>base pressure $\sim$ $10^{-8}$ mbar |
| PEC etching | PEC setup | Calibration in process |

# Appendix B

# Author Contributions

In this chapter, my contributions in the publications I am coauthor of are summarised.

## B.1 Ensembles of G-centres in Silicon Nanopillars

In this work, I fabricated silicon nanopillars, and Dr. Michael Hollenbach performed the spectroscopic measurements.

- Publication Title: Metal-assisted chemically etched silicon nanopillars hosting telecom photon emitters
- Journal: Journal of Applied Physics 132
- Year: 2022
- Abbreviations used in the table and text:
  - M.Ho. - Michael Hollenbach
  - **N.S.J. - Nagesh S. Jagtap**
  - C.F. - Ciarán Fowley
  - J.B. - Juan Baratech
  - V.A. - Verónica Guardia-Arce
  - U.K. - Ulrich Kentsch
  - A.V. - Anna Eichler-Volf
  - N.A. - Nikolay V. Abrosimov
  - A.E. - Artur Erbe
  - C.S. - ChaeHo Shin
  - H.K. - Hakseong Kim
  - M.H. - Manfred Helm

– W.L. - Woo Lee
– G.V.A. - Georgy V. Astakhov
– Y.B. - Yonder Berencén
– Sup. - Supporting

**Table B.1: Author contributions I(a)**

| Authors | M.Ho. | **N.S.J.** | C.F. | J.B. | V.A. | U.K. | A.V. | N.A. |
|---|---|---|---|---|---|---|---|---|
| **Data curation** | Equal | **Equal** | | Sup. | Sup. | | Sup. | Sup. |
| **Formal analysis** | Equal | **Equal** | | | | | | |
| **Investigation** | Equal | **Equal** | | Sup. | Sup. | Sup. | Sup. | Sup. |
| **Visualisation** | Equal | **Equal** | | Sup. | | | | |
| **Methodology** | Equal | **Equal** | Sup. | | | | | |
| Supervision | | | Equal | | | | | |
| Writing-review, editing | | | Sup. | | | | | |
| Validation | | | | | Sup. | Sup. | Sup. | |
| Resources | | | | | | | | Sup. |

**Table B.2: Author contributions I(b)**

| Authors | A.E. | C.S. | H.K. | M.H. | W.L. | G.V.A. | Y.B. |
|---|---|---|---|---|---|---|---|
| Data curation | | Sup. | Sup. | | | | Equal |
| Formal analysis | | Sup. | Sup. | | Sup. | | Lead |
| Investigation | | Sup. | Sup. | | Sup. | Sup. | Equal |
| Visualisation | | | | | | | Equal |
| Methodology | | | | | Sup. | | Lead |
| Supervision | Sup. | | | | | Sup. | Lead |
| Writing-review, editing | | | | | | | Equal |
| Validation | | | | | | | Equal |
| Resources | Sup. | | | Sup. | | Sup. | |
| Project administration | Sup. | | | | | | Lead |
| Conceptualisation | | Sup. | Sup. | | Sup. | Sup. | Lead |
| Funding acquisition | | | | Sup. | | Sup. | |
| Software | | | | | | Lead | |
| Writing-original draft | | | | | | | Lead |

**Author Contributions:** Michael Hollenbach: Data curation (equal); Formal analysis (equal); Investigation (equal); Visualisation (equal); Methodology (equal). Nagesh S. Jagtap: Data curation (equal); Formal analysis (equal); Investigation (equal); Methodology (equal); Visualisation (equal). Ciarán Fowley:

Methodology (supporting); Supervision (equal); Writing – review  editing (supporting). Juan Baratech: Data curation (supporting); Investigation (supporting); Visualisation (supporting). Verónica Guardia-Arce: Data curation (supporting); Investigation (supporting); Validation (supporting). Ulrich Kentsch: Investigation (supporting); Methodology (supporting); Validation (supporting). Anna Eichler-Volf: Data curation (supporting); Investigation (supporting); Validation (supporting). Nikolay V. Abrosimov: Data curation (supporting); Investigation (supporting); Resources (supporting). Artur Erbe: Project administration (supporting); Resources (supporting); Supervision (supporting). ChaeHo Shin: Conceptualisation (supporting); Data curation (supporting); Formal analysis (supporting); Investigation (supporting). Hakseong Kim: Conceptualisation (supporting); Data curation (supporting); Formal analysis (supporting); Investigation (supporting). Manfred Helm: Funding acquisition (supporting); Resources (supporting). Woo Lee: Conceptualisation (supporting); Formal analysis (supporting); Investigation (supporting); Methodology (supporting). Georgy V. Astakhov: Conceptualisation (supporting); Funding acquisition (supporting); Investigation (supporting); Resources (supporting); Software (lead); Supervision (equal). Yonder Berencén: Conceptualisation (lead); Data curation (equal); Formal analysis (lead); Investigation (equal); Methodology (lead); Project administration (lead); Supervision (lead); Validation (equal); Visualisation (equal); Writing – original draft (lead); Writing – review  editing (equal) [reproduced from the manuscript[40]].

## B.2 Wafer-Scale Nanofabrication of G-centres & W-centres

In this work, I fabricated the photoresist mask with lithographically defined arrays of nanoholes.

- Publication Title: Wafer-scale nanofabrication of telecom single-photon emitters in silicon
- Journal: Nature Communications 13
- Year: 2022
- Abbreviations used in the text:
  - M.Ho. - Michael Hollenbach
  - Y.B. - Yonder Berencén
  - G.V.A. - Georgy V. Astakhov
  - N.K. - Nico Klingner
  - L.B. - Lothar Bischoff
  - **N.S.J. - Nagesh S. Jagtap**
  - C.F. - Ciarán Fowley
  - U.K. - Ulrich Kentsch
  - N.V.A. - Nikolay V. Abrosimov
  - G.H. - Gregor Hlawacek
  - A.E. - Artur Erbe
  - M.H. - Manfred Helm

**Author Contributions:** M.Ho., Y.B., and G.V.A. conceived and designed the experiments. M.Ho. performed the single-photon spectroscopy experiments under the supervision of G.V.A. M.Ho., N.K., and L.B. designed the FIB layout. N.K. and L.B. performed FIB implantation and in situ annealing. M.Ho., **N.S.J.**, Y.B., C.F., and G.V.A. **designed the PMMA mask. N.S.J. fabricated the PMMA mask.** M.Ho., U.K., Y.B., and G.V.A. conceived and performed the broad-beam silicon implantation. C.F. and Y.B. carried out the RTA processing. N.V.A. grew the ultrapure silicon substrates. M.Ho. and G.V.A. wrote the manuscript. All authors, together with G.H., A.E., and M.H., discussed the results and contributed to the manuscript preparation [reproduced from the manuscript[41]].

# Publication List

- Philipp Bredol, Felix David, Nagesh S. Jagtap, Yannick S. Klaß, Georgy V. Astakhov, Artur Erbe, and Eva M. Weig. **Effect of helium ion implantation on 3C-SiC nanomechanical string resonators.** *arXiv:2405.02035*, 2024

- Michael Hollenbach, Nico Klingner, Nagesh S.Jagtap, Lothar Bischoff, Ciarán Fowley, Ulrich Kentsch, Gregor Hlawacek, Artur Erbe, Nikolay V. Abrosimov, Manfred Helm, Yonder Berencén & Georgy V. Astakhov. **Wafer-scale nanofabrication of telecom single-photon emitters in silicon.** *Nature Communications*, 13, 7683, 2022

- Michael Hollenbach, Nagesh S. Jagtap, Ciarán Fowley, Juan Baratech, Verónica Guardia-Arce, Ulrich Kentsch, Anna Eichler-Volf, Nikolay V. Abrosimov, Artur Erbe, ChaeHo Shin, Hakseong Kim, Manfred Helm, Woo Lee, Georgy V. Astakhov, and Yonder Berencén. **Metal-assisted chemically etched Si nanopillars hosting telecom photon emitters.** *Journal of Applied Physics*, 132, 033101, 2022

The following publication is related to my previous work on bottom-up nanofabrication using DNA origami during my master's degree.

- Türkan Bayrak, Nagesh S. Jagtap and Artur Erbe., **Review of the Electrical Characterization of Metallic Nanowires on DNA Templates** *International Journal of Molecular Sciences*, 19(10), 3019, 2018

# Conference Contributions

- Nagesh S. Jagtap, Felix David, Philipp Bredol, Yannick Klaß, Manfred Helm, Georgy Astakhov, Eva Weig, Artur Erbe. **Effect of Helium Ion Implantation on 3c-sic Nanomechanical Resonators.**, FIT4NANO Workshop 2024, 16-20 September 2024, Durrës, Albania - Poster Presentation (Planned).
- Nagesh S. Jagtap, Felix David, Philipp Bredol, Yannick Klaß, Manfred Helm, Georgy Astakhov, Eva Weig, Artur Erbe. **Effect of Helium Ion Implantation on 3c-sic Nanomechanical Resonators.**, IEEE NAP-2024, 8-13 September 2024, Riga, Latvia - Poster Presentation (Planned).
- Nagesh S. Jagtap, Felix David, Philipp Bredol, Yannick Klaß, Manfred Helm, Georgy Astakhov, Eva Weig, Artur Erbe. **Change in Mechanical Properties of SiC Resonators Using Helium Ion Implantation.** NANONET+ Annual Workshop 2023, 11-13 September 2023, Sayda, Germany - Oral Presentation.
- Nagesh S. Jagtap, Felix David, Philipp Bredol, Yannick Klaß, Manfred Helm, Georgy Astakhov, Eva Weig, Artur Erbe. **Towards Hybrid Spin-Mechanical Systems in Silicon Carbide Using Helium Ion Implantation.** FIT4NANO Workshop 2023, 17-19 July 2023, Lisbon, Portugal - Poster Presentation.
- Nagesh S. Jagtap, Felix David, Philipp Bredol, Yannick Klaß, Manfred Helm, Georgy Astakhov, Eva Weig, Artur Erbe. **Effect of Helium Ion Implantation on Nanomechanical Resonators in 3C-SiC.** Frontiers of Nanomechanical Systems (FNS), 6-9 June 2023, Delft, Netherlands - Poster Presentation.
- Nagesh S. Jagtap, Yannick Klaß, Felix David, Philipp Bredol, Manfred Helm, Georgy Astakhov, Eva Weig, Artur Erbe. **Effect of Helium Ion Implantation on Nanomechanical Resonators in 3C-SiC.** DPG-Physik SKM 2023, 26-31 March 2023, Dresden, Germany - Oral Presentation.

- Nagesh S. Jagtap, Yannick Klaß, Felix David, Philipp Bredol, Manfred Helm, Ciarán Fowley, Georgy Astakhov, Eva Weig, Artur Erbe. **Effect of $He^+$ Implantation on Nanomechanical Resonators in 3C-SiC.** NANONET+ Annual Workshop 2022, 4-6 October 2022, Görlitz, Germany - Oral Presentation.

- Nagesh S. Jagtap, Michael Hollenbach, Ciarán Fowley, Juan Baratech, Verónica Guardia-Arce, Ulrich Kentsch, Anna Eichler-Volf, Nikolay V. Abrosimov, Artur Erbe, ChaeHo Shin, Hakseong Kim, Manfred Helm, Woo Lee, Georgy V. Astakhov, and Yonder Berencén. **Top-down Nanofabrication of Silicon Nanopillars Hosting Telecom Photon Emitters.** DPG Meeting 2022, 4-9 September 2022, Regensburg, Germany - Oral Presentation.

- Nagesh S. Jagtap, Michael Hollenbach, Ciarán Fowley, Juan Baratech, Verónica Guardia-Arce, Ulrich Kentsch, Anna Eichler-Volf, Nikolay V. Abrosimov, Artur Erbe, ChaeHo Shin, Hakseong Kim, Manfred Helm, Woo Lee, Georgy V. Astakhov, and Yonder Berencén. **A Photonic Platform Hosting Telecom Photon Emitters in Silicon.** LEAPS meets Quantum Technology, 15-20 May 2022, Elba Island, Italy - Poster Presentation.

- Nagesh S. Jagtap, Michael Hollenbach, Ciarán Fowley, Yonder Berencén, Woo Lee, Georgy V. Astakhov, Artur Erbe, Manfred Helm. **Top-down Fabrication of Silicon Photonic Structures for Hosting Single-Photon Emitters.** Virtual DPG Spring Meeting SKM 2021, 27 September-1 October 2021, Germany - Poster Presentation.

- Nagesh S. Jagtap, Michael Hollenbach, Ciarán Fowley, Juan Baratech, Ulrich Kentsch, Nikolay V. Abrosimov, Artur Erbe, Manfred Helm, Woo Lee, Georgy V. Astakhov, and Yonder Berencén. **Top-down Fabrication of Silicon Photonic Structures by Metal Assisted Chemical Etching (MACEtch).** NANONET+ Annual Workshop 2021, 21-23 September 2021, Klingenberg, Germany - Oral Presentation.

# List of Figures

# List of Tables

# Declaration

I declare that I have personally written the present doctoral thesis with the title **Colour Centres in 3D Nanostructures for Quantum Applications** without any improper support of a third party and without using any other means than indicated. Help of third parties was only used in scientifically appropriate way and within the permitted scope of doctorate regulations of the Faculty of Mathematics and Natural Sciences of the Dresden University of Technology (TUD). There were no improper transfers of direct or indirect financial benefits in relation to the submitted doctoral thesis. In particular, I did not seek the help of any commercial doctoral consultant.

I also state that Intellectual property which has been used directly or indirectly from other sources is clearly indicated. The thesis has never been published and has never been submitted up to this date in identical or similar form to any other graduation authority in Germany or abroad. I am aware that the doctorate proceedings can be discontinued or the doctoral title can be withdrawn in case of faulty information or if I do not follow this declaration.

This PhD thesis is based on research in Helmholtz-Zentrum Dresden - Rossendorf (HZDR) at the Institute of Ion Beam Physics and Materials Research. This scientific work was supervised by Prof. Dr. Artur Erbe, PD Dr. Georgy Astakhov and Prof. Dr. Manfred Helm.

Dresden, 29$^{th}$ July 2024

Nagesh S. Jagtap